University of Strathclyde

Department of Electronic and Electrical Engineering

Performance Improvement and Interference Cancellation in Tracking Radar

By

Sherif Abdelhalim Radwan Elgamel

A thesis presented in fulfilment of the requirements for the degree of

Doctor of Philosophy

2011

Declaration

This thesis is the result of the author's original research. It has been composed by the author and has not been previously submitted for examination which has led to the award of a degree. I have referenced the work of others where appropriate throughout the thesis.

Acknowledgements

It is a pleasure to thank the many people who made this thesis possible. I would like to begin with thanking my supervisor Prof. John Soraghan for giving me an excellent opportunity to carry out a very innovating and challenging research on interference against tracking radar. Prof. Soraghan provided me endless source of ideas and encouragement. His enthusiasm in research, systematic organisation in work and optimistic attitude towards life positively influenced my study and life. His assistance and instructions during my time at University of Strathclyde has been invaluable.

I would like to extend my sincere gratitude to my sponsor, the Egyptian government, through MoD for giving me the opportunity to pursue my PhD in University of Strathclyde.

My deepest and sincere thanks are always to my parents, parent-in-laws, brothers, sisters, brother-in-laws and sister-in-laws for their constant support and prayers. I am so lucky and so proud to have such a wonderful family.

Lastly, and most importantly, I owe my loving thanks to my wife Mona and daughters Sama and Hamsa without their understanding, endless patience and encouragement it would have been impossible for me to finish this work.

Dedication

Dedicated to

My wife

Mona

My children

Sama

Hamsa

Abstract

This Thesis presents monopulse radar concepts and signal processing techniques including fractional Fourier transform (FrFT), empirical mode decomposition (EMD), and combined EMD-FrFT to mitigate different types of interference associated with this radar. A matched filter is implemented for a chirp radar signal in the optimum fractional Fourier domain (FrFD). Mathematical formula for a received chirp signal in the Fourier domain and a generalized formula in the FrFD are derived using the principle of stationary phase (PSP). The performance enhancements in using the matched filter in the FrFD are presented and an example of using the FrFT radar matched filter for multiple target detection is presented. Two new monopulse system configurations based on new FrFT filtering algorithms are used to overcome the interference problems of unwanted targets appearing in the monopulse look direction and the presence of high power noise interference (through the radar main lobe or side lobe), respectively. A very high improvement in the radar's tracking ability for different SNRs is gained by using the suggested canceling techniques in both interference scenarios. Another solution to the distortion problem, due to high power manmade interference, is proposed using a new monopulse processor based on EMD system. This algorithm successfully decreases the high power noise interference and improves the received radar SNR. Finally, a proposed EMD-FrFT filtering algorithm merges the benefits of both EMD and FrFT filtering algorithms to reduce the distortion problem due to high power interference in chirp monopulse radar systems. This algorithm successfully decreases the high power noise interference and improves the received radar SNR.

Contents

List of Figures

List of Tables

List of Abbreviations

AM	Amplitude modulation
CPI	Coherent processing interval
DBM	Displaced beam method
DM	Derivative method
DT	Direct thresholding
EMD	Empirical mode decomposition
EMD-CIIT	Clear iterative EMD interval thresholding
EMD-DT	EMD Detrending and Thresholding
EMD-IT	Interval thresholding EMD
EMD-IIT	Iterative EMD interval thresholding
EOF	Empirical orthogonal function expansion
FFT	Fast Fourier transform
FT	Fourier transform
FrFD	Fractional Fourier domain
FrFT	Fractional Fourier transform
FrFT-ATF	FrFT for additive targets filtering
FrFT-NIF	FrFT noise interference filtering
HHT	Hilbert Huang transformation
HPRM	Half phase reversed method
IFFT	Inverse fast Fourier transform

IFT	Inverse Fourier transform
IMF	Intrinsic Mode Functions
INR	Interference to noise ratio
LCT	Linear canonical transform
LFM	Linear frequency modulation
LO	Local oscillator
ML	Maximum likelihood
MRC	Monopulse response curve
MV	Min variance technique
OINR	Output interference to noise ratio
PRI	Pulse repetition interval
PSP	Principle of stationary phase
RCS	Radar cross section
RMS	Root mean square
SFT	Space fast time
SNR	Signal to noise ratio
SST	Space slow time
STDAE	Standard deviation of the angle error
ULA	Uniform linear array

List of Symbols

a	Fractional Fourier transform order
$\mathfrak{a}$	Parameter for LCT matrix
a	Constant
$\boldsymbol{a}(\nu)$	Centre phase normalized steering vector in the look direction
a_{opt}	Optimum Fractional Fourier order.
a_y	Integral boundary
$\mathfrak{b}$	Parameter for LCT matrix
b	Constant
b_y	Integral boundary
c	Speed of light
$\boldsymbol{c}$	Constraint vector.
$\mathfrak{c}$	Parameter for LCT matrix
$\boldsymbol{c}(t)$	Pulsed chirp signal
$\mathfrak{d}$	Parameter for LCT matrix
$\boldsymbol{d}[n]$	EMD residual.
$\boldsymbol{e}_{\varphi_k}[n]$	Envelope curve in direction φ_k
$\boldsymbol{e}'_{\varphi_k}[n]$	Tangent curve in direction φ_k
f	Function belong to $\mathcal{L}$
f_a	FrFT of function f

f_c	Radar carrier frequency
f_d	Target Doppler frequency.
f_τ	Denotes frequency counterpart of τ
$\boldsymbol{f}_d$	Doppler vector
$\boldsymbol{f}_\phi$	Antenna phase factor
g	Function belong to $\mathcal{L}$
g_a	FrFT of function g
$\boldsymbol{g}_{opt,i}$	Optimum filter in the FrFT domain
$\boldsymbol{h}^{(i)}[n]$	Intrinsic mode functions.
$\boldsymbol{h}_m^{(i)}[n]$	Temporarily IMF
i	Index
j	Imaginary number
k	Index
m	Index
$\boldsymbol{m}_m[n]$	Mean curve
$\boldsymbol{m}(\phi)$	Monopulse response curve
$\boldsymbol{n}_{jam}(t)$	White Gaussian noise
q	Index
$\boldsymbol{s}'$	Sum of the additional unwanted targets' signals
$\boldsymbol{s}_e$	Estimate chirp signal of the tracked target at range R_t
$\boldsymbol{s}'_e$	Estimate chirp signal of the additive targets

$\hat{\boldsymbol{s}}$	Filtered signal in time domain
$s(y)$	Slowly varying function
$s_m(t)$	Matched filter output
t	Time
t^*	Stationary point
t_a	Time variable t in the a^{th}
t_s	Sampled time axis
t_{st}	Chirp start time sampling number
t_i^k	Locations of the maxima
u	Normalized coordinates for t
u^*	Stationary point
u_a	Normalized coordinates for t_a
u'	Discrete normalized representation for u
u_a'	Discrete normalized representation for u_a
$\boldsymbol{w}$	Spatial weight vector
$\boldsymbol{w}_\Sigma$	Spatial weight vector for the sum processor
$\boldsymbol{w}_\Delta$	Spatial weight vector for the difference processor
$\boldsymbol{W}_\Sigma(\phi)$	Monopulse beam pattern for the sum processor
$\boldsymbol{W}_\Delta(\phi)$	Monopulse beam pattern for the difference processor
$\boldsymbol{x}^{(m)}(t)$	Spatial snapshot
$\boldsymbol{x}[u]$	Sampled signal

$\boldsymbol{z}_q^{(i)}$	IMF interval
$\boldsymbol{z}_i$	Processor output when only interference is present
$z_\Sigma(t)$	Sum monopulse processor output
$z_\Delta(t)$	Difference monopulse processor output
A	Received signal amplitude
D	Distance between antenna elements
$\boldsymbol{C}$	Constraint matrix.
F_s	Sampling frequency
F_{start}	Chirp start frequency.
F_{stop}	Chirp stop frequency.
F^a	Fractional Fourier transform operator
F^{-a}	Inverse fractional Fourier transform operator
$\overline{\boldsymbol{F}}$	Discrete FT matrix
$\overline{\boldsymbol{F}}^a$	Discrete FrFT matrix
$F^M[x(t)]$	Linear canonical transform
^{H}	Hermitian
$\boldsymbol{H}$	Matrix characterizing system degradation process
$\boldsymbol{I}$	$1\times N$ unitary vector
L	Number of samples in received window
L_{IMF}	Number of IMFs
K	Time frequency ratio
K	Number of projection direction for bivariate EMD algorithms

K_d	Discrete definition of K
$K_\theta(t_a,t)$	Transformation Kernel
$K^M(t^M,t)$	LCT kernel
M	Number of coherent pulses
M	2×2 LCT rotation matrix
M_T	Number of samples in pulse width
$M_F(f)$	Matched filter
N	Number of antenna elements
N_t	Number of targets
$\boldsymbol{N}_{array}$	Vector represented as $\{0,1,\ldots..,N-1\}$
$\boldsymbol{N}_{jam}$	Barrage noise jamming
P_p	Peak position
$\boldsymbol{R}_{xx}$	Covariance matrix for the signal $\boldsymbol{x}$
$\boldsymbol{R}_{yy}$	Covariance matrix for the signal $\boldsymbol{y}$
$\boldsymbol{R}_{ss}$	Covariance matrix for the tracked target signal
$\boldsymbol{R}_{s's'}$	Covariance matrix for the additive targets signal
$\boldsymbol{R}_{x_az_a}$	Crosscorrelation matrix between signals $\boldsymbol{x}$ and $\boldsymbol{z}$
$\boldsymbol{R}_{z_az_a}$	Auto correlation matrix for signal $\boldsymbol{z}$
$\boldsymbol{R}_{s_az_a}$	Cross correlation matrix
$\boldsymbol{R}_{z_az_a}$	Auto correlation matrix for signal $\boldsymbol{z}$
$\Re$	Real

R_t	Target range
R_o	Range at bin 0
$\boldsymbol{R}_x$	covariance matrix
S	Normalization factor
S^{B_i}	Low Frequency comment in bivariate EMD
$\boldsymbol{S}(t)$	Received radar signal
$S(f)$	Fourier transform of $s(t)$
T	Pulse duration
T_p	Sampling period
T_{w_1}	Start of time of receiving window
T_{start}	Start time of the returned pulse
$T[i]$	Threshold level energies
$\hat{W}[i]$	Estimated IMFs energy
$W_f(t,t_1)$	Wigner distribution
$W_{f_a}(t,t_1)$	Wigner distribution of fractional function
$X_\theta(t_a)$	Fractional Fourier formula of $x(t)$ at order a.
$\boldsymbol{X}_{\boldsymbol{SFT}}(t)$	SFT snapshot
$\boldsymbol{X}_{\boldsymbol{SST}}(t)$	SST snapshot
$\boldsymbol{Y}$	Sum of all distortion signals
$\boldsymbol{Z}$	Observation model
Δf	Band width.

ΔR	Distance within the time window
Δt	Time lag between wave fronts
ϕ	Propagation angle (Target angle)
$\hat{\phi}$	Estimate of target angle.
ϕ_s	Random phase shift
ϕ_o	Random phase shift
ϕ_{jam}	Jammer angle.
φ_k	Projection direction for bivariate EMD algorithms
$\varphi(y)$	Phase change
θ	Fractional Fourier transform angle
θ_{opt}	Optimal fractional Fourier transform angle
ϑ_{opt}	Complement angle of Optimal fractional Fourier transform angle
ε	Constant
ε_ϕ	Error angle
$\varepsilon_v(t)$	Error voltage
$\sigma_{\varepsilon_\phi}$	Standard deviation of the angle error
σ_n^2	Noise power
σ_{jam}^2	Jamming power
ν	Spatial steering frequency
ν_t	spatial steering frequency snapshot at time instant t
$\boldsymbol{\nu}_\Sigma$	Spatial steering frequency vectors for the sum channel

$\boldsymbol{v}_{\Delta}$	Spatial steering frequency vectors for the difference channel
ζ	Mean square output of the processor
τ	denotes time variable
$\upsilon_k[u']$	k^{th} discrete Hermite-Gaussian function
λ_k	Eigenvalue
γ	Chirp rate parameter
ρ	Constant
$\boldsymbol{\rho}_{\varphi_k}[n]$	Project the complex-valued signal on direction
δf	Frequency resolution.
δt	Time resolution
δ_t	Time shift
$\boldsymbol{\Lambda}_g$	Diagonal matrix

1. Introduction

1.1 Preface

Typical tracking radars use a pencil beam to receive echoes from a single target and track the target in angle, range, and/or Doppler. Electronic beam-scanning phased array radars may track multiple targets by sequentially dwelling upon and measuring each target while excluding other echo or signal sources. Because of its narrow beam width tracking radars usually depend upon information from surveillance radar or other source of target location to acquire the target. Hence tracking radar places its beam on or in the vicinity of the target before initiating a track. There are a large variety of tracking radar systems including some that achieve simultaneously both surveillance and tracking functions [1].

Monopulse radars are commonly used in target tracking because of their angular accuracy [2]. They provide superior angular accuracy and less sensitivity to fluctuation in the radar cross section (RCS) of the target compared to other types of tracking radars [3]. However, these radars are affected by different types of interference which affects the target tracking process that may lead to inaccurate tracking [1, 3].

Monopulse radars are used for civilian and military applications. In military, it is used to track the highly manoeuvrable airplanes and missiles, fire control systems, and in fire-and-forget radar guided missile (monopulse seeker). In civilian application they are used in airports for air traffic control. Monopulse radars can accommodate a significant increase in the number of airplane arrival to airports [3-5].

Monopulse radar first appeared at the Naval Research Laboratory (USA) and OKB 30 (USSR) in 1940s. It was used for surface-to-air missiles projects in 1945, naval tracking radar in 1960s, and from 1970s spread into many military projects.

Historically, monopulse radars employ two separate feed horns on a single antenna

element in order to generate two receive beams that are slightly offset in azimuth (or elevation) angle. Sum and difference outputs are formed by summing and subtracting the two beam outputs, respectively [6]. The ratio of difference to sum output voltages, called the error voltage, is then used to determine the degree of correction necessary to realign the beam axis with the target [7]. With the introduction of phased array technology, it became unnecessary to employ special hardware for monopulse processing, since the array itself can electronically form the multiple beams needed [8, 9]. A conventional monopulse processor for phased array radar is obtained by appropriately phasing the individual array channels to obtain sum and difference outputs. The ratio of difference to sum outputs provides the measure by which the angle offset from the beam axis (i.e., look direction) is determined. The updated angle measurement is used to compute phases for the channels so as to realign the beam axis with the target. Consequently the radar is affected by different types of interference [10] that may cause inaccurate tracking.

1.2 Motivation of Research

The aim of this thesis is to explore new signal processing techniques which can be used to improve the interference mitigation, noise rejection, and enhance the performance of the monopulse tracking radar. The objectives of the research presented in this thesis are two fold. The first objective is to develop a new monopulse radar processor based filtering algorithm to solve the interference problem due to more than one target appears in the monopulse radar half power beam width. The second objective is to investigate developed algorithms to mitigate the problem of high power interference (jamming) introduced to the radar processor and enhance the monopulse radar tracking performance. The thesis will address the enhancements, modifications, and inventions required to achieve high tracking radar performance using new signal processing techniques while avoiding as much as possible any additional complexity or increase in the computational cost.

1.3 Summary of Original Contributions

The research detailed in this thesis includes original contributions to the field of tracking radars, noise/interference rejection or suppression, and target detection. These contributions are as follows:

1. A new matched filter is implemented for a chirp radar signal in the optimum fractional Fourier domain (FrFD). Mathematical formulae for a received chirp signal in the Fourier domain and a generalized formula in the FrFD are derived using the principle of stationary phase (PSP). These expressions are used to show the limitations of the matched filter in the FrFD. The parameters that affect the chirp signal in the optimum FrFD and the implementation of radar matched filter in FrFD are described. The required processing steps to perform the radar matched filter in FrFD are demonstrated. The complexity of the FrFD matched filter over the normal FT matched filter is also investigated. The performance enhancements in using the matched filter in the FrFD are presented and the enhancement in the output SNR's at different target SNR's are also described. Example of using the FrFT radar matched filter for multiple targets detection is presented [11].

2. A new signal processing algorithm, referred to as FrFT-ATF, is developed that offers a solution to the interference problem resulting from additive targets that appears in the monopulse look direction. The technique is based on the use of optimal fractional Fourier transform (FrFT) filtering. The relative performance of the new filtering method over traditional based methods is assessed using standard deviation angle estimation error (STDAE) for a range of simulated environments. The proposed system configuration succeeds in significantly cancelling additional target signals appearing in the look direction beam width even if these targets have the same Doppler frequency [12-14].

3. A new monopulse radar structure is proposed that aims to mitigate high power interference jamming signal. The structure is based on the use of optimal FrFT

filtering, referred to as FrFT-NIF. The improved performance of the new monopulse radar structure over the traditional monopulse processor is assessed using STDAE for a range of simulated and real environments. The proposed system configurations with optimum FrFT filters is shown to reduce the interfered signal (simulated and real) and to minimize the STDAE for monopulse processors even with jamming present in the main lobe. Output interference-to-noise ratio ($OINR$) is used to quantify the monopulse processor improvement by comparing the mitigation performance for the FrFT based monopulse radar compared to the conventional monopulse radar [15, 16].

4. New monopulse radar structures that utilizes an empirical mode decomposition (EMD) based denoising processor to overcome the jamming signals are presented. EMD filtering is carried out for the complex radar chirp signal with subsequent detrending, thresholding, and denoising processes. These processes are used to decrease the noise level in the radar processed data to improve the signal to noise ratio. The performance enhancement using the monopulse radar tracking system with EMD based filtering is included using the STDAE for different jamming scenarios and different target SNRs. The proposed system configuration is shown to reduce the interfered signal and to minimize the STDAE for high power interference signal presence in the main lobe and side lobe. STDAE shows that the new EMD based system works well in the case of main beam interference and side lobe interference for the conventional processor and, in the case of the spatial adaptive processor, is effective in the case of main lobe interference [17, 18].

5. A new signal processing subsystem for conventional monopulse tracking radars that offers an improved solution to the problem of dealing with manmade high power interference (jamming) is presented. It is based on the hybrid use of EMD and FrFT. EMD-FrFT filtering is carried out for complex noisy radar chirp signals to decrease the signal's noisy components. An improvement in the signal-to-noise

ratio (SNR) for different target SNRs is achieved using the proposed EMD-FrFT algorithm [19, 20].

1.4 Thesis Organization

The remainder of this thesis is divided into six chapters, the organization of which is explained as follows:

Chapter 2 provides an overview of monopulse radars. It starts with the tracking radar, which uses angle tracking techniques, in order to introduce the sum and difference monopulse radar which will be used throughout the thesis. The basic monopulse radar structure and the basic monopulse radar processor are investigated next. Later on in this chapter, the mathematical models for both the conventional and spatial monopulse processors are reviewed. The last part of this chapter presents the real and simulated parameters for the target, jammer, and radar scenarios.

Chapter 3 reviews the FrFT and EMD algorithms. Both algorithms are used in the remainder of this thesis in the design and implementation of advanced monopulse radar systems that aim to overcome different types of interference in tracking radars. A historical background and the applications of the two algorithms are given followed by details description.

Chapter 4 uses the principle of stationary phase (PSP) to derive the chirp signal in the Fourier and fractional Fourier domains, respectively, and presents a matched filter in the Fourier domain and FrFD. A set of simulation results is presented in for different scenarios. It includes a discussion on the chirp matched filtering in the FrFD, the signal parameter limitations, and the improvement in SNR using matched filter in FrFT. Section 4.3.5 of this chapter presents work that was carried out in collaboration with Carmine Clemente on FrFT Matched filter for multiple targets. Chapter 4 concludes with a discussion underlining the results and the complexity comparison for matched filter in both the Fourier and fractional Fourier domains.

Chapter 5 consists of two main sections (5.2 and 5.3) introducing new algorithms that aim to overcome the monopulse distortion problems mentioned previously. This chapter is organized as follows: Section 5.2 proposes a new structure of the FrFT based monopulse radar processor. FrFT addtitive target filtering (FrFT-ATF) is a new algorithm for optimum FrFT to reduce the interference due to more than one target appearing in the radar look direction. Later in Section 5.2, a set of simulation results is presented for single and multiple targets using the new monopulse processor. Section 5.3 proposes a new structure of the FrFT based monopulse radar processor. The proposed FrFT noise interference filtering (FrFT-NIF) mitigates the effects of high power jamming signal introduced to the radar processor through the radar antenna. A set of simulation results using simulated and real data is presented for the new monopulse structure that shows the improved reduction in the interfered signal and improves the tracking performance for the FrFT based monopulse radar compared to the conventional monopulse radar are included. Section 5.4 concludes the chapter.

Chapter 6 consists of two main sections (6.2 and 6.3) that introduce new algorithms to overcome the monopulse distortion problems mentioned previously. This chapter is organized as follows: Section 6.2 proposes a new monopulse radar that employs an EMD based monopulse processor to reduce the interference due to high power jamming. Later in Section 6.2, a set of simulation results is presented for different jamming scenarios at different target SNR that demonstrates the superior performance of the new structure. Section 6.3 proposes a new EMD-FrFT interference filtering algorithm. A set of simulation results is presented for the received signal improvement at different SNRs is also introduced. Section 6.4 concludes the chapter.

Chapter 7 includes a summary and conclusions of this thesis are presented, along with a discussion of its limitations and suggestion of potential areas for further future work.

The appendices contain some detailed calculations and some theoretical material which would impede the flow of the thesis. A list of the author's publications resulting from the research undertaken in this thesis is also provided.

2. Monopulse Tracking Radar

2.1 Introduction

Monopulse radars are used to track a target that appears in the look direction. Similar to other tracking radar systems, monopulse radars suffer from distortion such as man made high power interference and additive unwanted targets, which appear in the look direction that may lead to errors in the target tracking angles resulting in target mistracking.

This chapter provides an overview of monopulse radars. Section 2.2 introduces radar background. The tracking radar which uses angle tracking techniques, in order to introduce the sum and difference monopulse radar which will be used throughout the thesis is described in Section 2.3 . The basic monopulse radar structure is investigated in Section 2.4. In Section 2.6, the mathematical modelling for both the conventional and spatial monopulse processor are reviewed. The basic monopulse radar processor is investigated in Section 2.7. Section 2.9 of this chapter presents some real and simulated parameters for the target, jammer, and radar scenarios that will be used throughout the thesis.

2.2 Radar Background

A radar device transmits a waveform into the atmosphere and then listens for echoes as the transmitted waveform reflects back from surrounding objects [1, 3]. Depending on the radar, various types of information can be obtained from the incoming echoes about the desired scattering object, known as the target. Range information can be calculated from the amount of time takes by the transmitted signal to travel to an object and then arrive back at the receiver [9, 21]. Directional information can be obtained by scanning the surrounding space with a directive beam. Target velocity can be determined through

measuring the Doppler shift induced in the reflected waveform. The accuracy or resolution to which any of the above parameters can be measured depends to a large extent on the physical parameters of the radar and its electronics and to some extent on the environment in which it operates.

Figure 2.1 shows a general block diagram of a tracking radar system [1, 3]. A waveform generator is used to generate the desired wave which is up-converted to the radar carrier frequency using mixer and local oscillator (LO) before amplification and transmission through the duplexer to the radar antenna. The duplexer is used to separate between the transmitting and receiving signal. The received signal is down converted (using mixer and LO), amplified by IF amplifier, and passes through a matched filter to extract the useful signal before detection and display [1].

2.3 Tracking Radar with Angle Tracking Techniques

Tracking radar systems are used to measure the target's relative position in range, azimuth angle, elevation angle, and velocity [22]. The radar can predict future values by using and keeping track of these measured parameters. Target tracking is important to military radars as well as most civilian radars. In military radars tracking is responsible for fire control and missile guidance; in fact, missile guidance is almost impossible without proper target tracking. Commercial radar systems such as civilian airport traffic control radars may utilize tracking as a means of controlling incoming and departing airplanes[23].

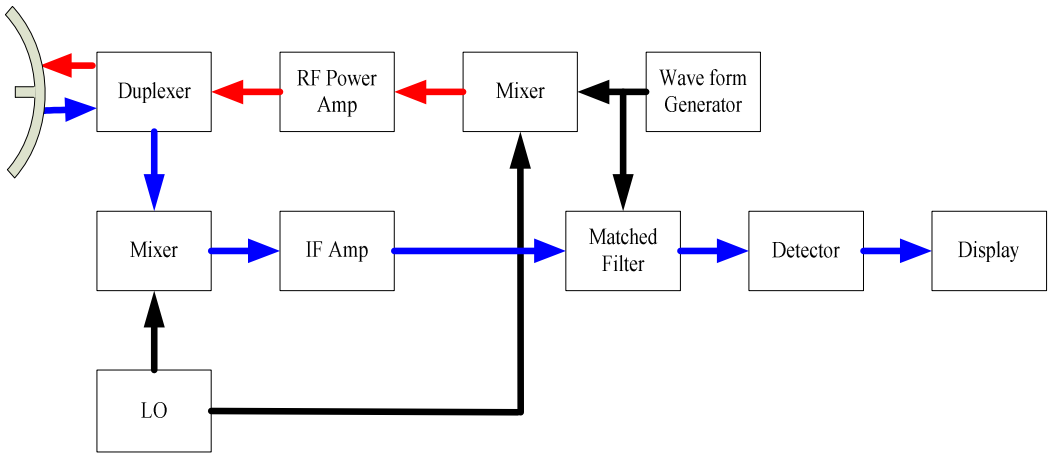

Figure 2.1 General Block diagram of radar system

Angle tracking is concerned with generating continuous measurements of the target's angular position in the azimuth and elevation coordinates. The accuracy of early generation angle tracking radars depend heavily on the size of the pencil beam employed. Most modern radar systems achieve very fine angular measurements by utilizing monopulse tracking techniques [9]. Tracking radars use the angular deviation from the antenna main axis of the target within the beam to generate an error signal [24]. This deviation is normally measured from the antenna's main axis. The resultant error signal describes how much the target has deviated from the beam main axis. Then, the beam position is continuously changed in an attempt to produce a zero error signal.

In order to be able to quickly change the beam position, the error signal needs to be a linear function of the deviation angle. It can be shown that this condition requires the beam's axis be squinted by some angle (squint angle) off the antenna's main axis. A tracking radar measures coordinates of the target and provides data that may be used to determine the target path and to predict its future position. All or only part of the available radar data-range, elevation angle, azimuth angle, and Doppler frequency shift may be used in predicting the future position.

Classifications of the tracking radar types are shown in Figure 2.2. These types are described in detail in the following subsections.

2.3.1 Sequential Comparison Tracking Techniques

The main aspect of sequential lobing tracking radar is the antenna. It usually faces the

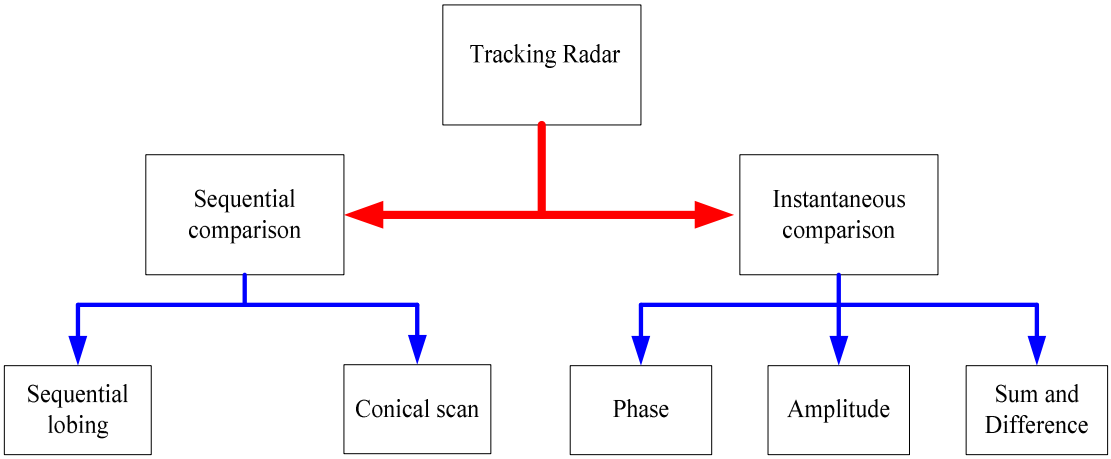

Figure 2.2 Classifications of angle tracking radar

target all the time in order to keep it in the centre of the antenna beam. If the target moves away from the centre of the beam, this produce an error voltage which is amplified and fed to servo motors to drive the antenna back on the target [21, 25]. There are two main techniques depending on this idea, the sequential lobing and the conical scan [26].

2.3.1.1 Sequential Lobing

Sequential lobing [27] was one of the first tracking techniques utilized by early generation of radar systems. Sequential lobing is often referred to as lobe switching or sequential switching. It has a tracking accuracy that is limited by the pencil beam width and the noise caused by either mechanical or electronic switching mechanisms.

Figure 2.3 shows the sequential lobing for target tracking. In Figure 2.3 as the beam is switched between the two positions (position A and position B), the radar measures the returned signal levels. The difference between the two measured signal levels is used to compute the angular error signal [23]. For example, when the target is tracked on the tracking axis, as the case in Figure 2.3-A, the voltage difference is zero. However, when the target is off the tracking axis, as in Figure 2.3-B, a non-zero error signal is produced. The sign of the voltage difference determines the direction in which the antenna must be moved with the goal to make the voltage difference be equal to zero [23].

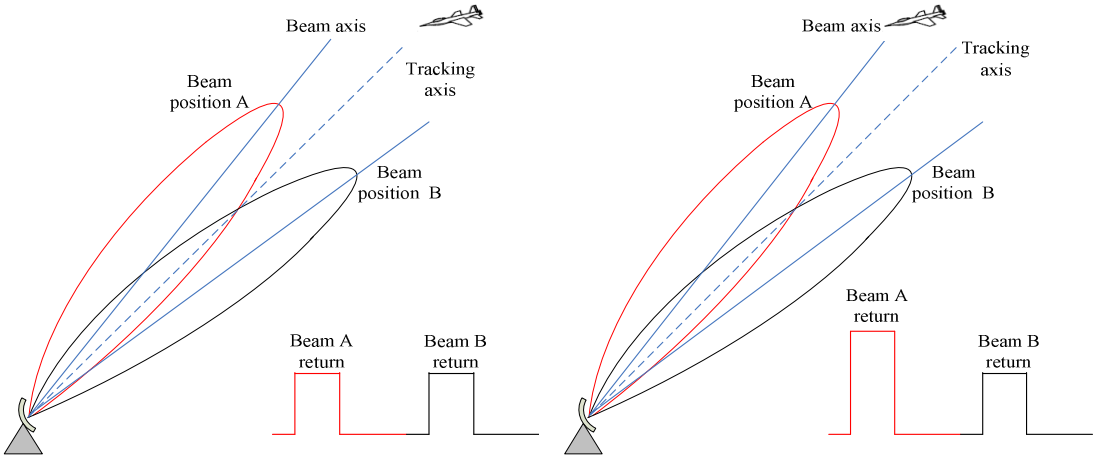

(A) (B)

Figure 2.3 Sequential lobing target tracking

2.3.1.2 Conical Scan

Conical scan [28] is a logical extension of sequential lobing. The radar antenna is continuously rotated at an offset angle off the main axis. The antenna's beam position is continuously changed so that the target will always be on the tracking axis [9].

In order to illustrate how conical scan tracking is achieved, Figure 2.4 shows two different cases. The first case shown in Figure 2.4-A, the antenna rotates around the tracking axis all target returns have the same amplitude (zero error signals). Figure 2.4-B shows the second case when the beam is at position B. The envelope of target returned signals is similar to the amplitude modulation (AM) envelope [25]. This AM envelope corresponds to the relative position of the target within the beam. Thus the extracted AM envelope can be used to derive a servo-control system in order to position the target on the tracking axis.

2.3.2 Instantaneous Comparisons Monopulse Techniques

Instantaneous comparison monopulse tracking is similar to lobing in the sense that four squinted beams are required to measure the target's angular position [29]. The difference is that the four beams are generated simultaneously rather than sequentially. For this purpose, a special antenna feed is utilized such that the four beams as shown in Figure 2.5, are produced using a single pulse, hence the name monopulse [6]. With the introduction of phased array technology, it became unnecessary to employ special

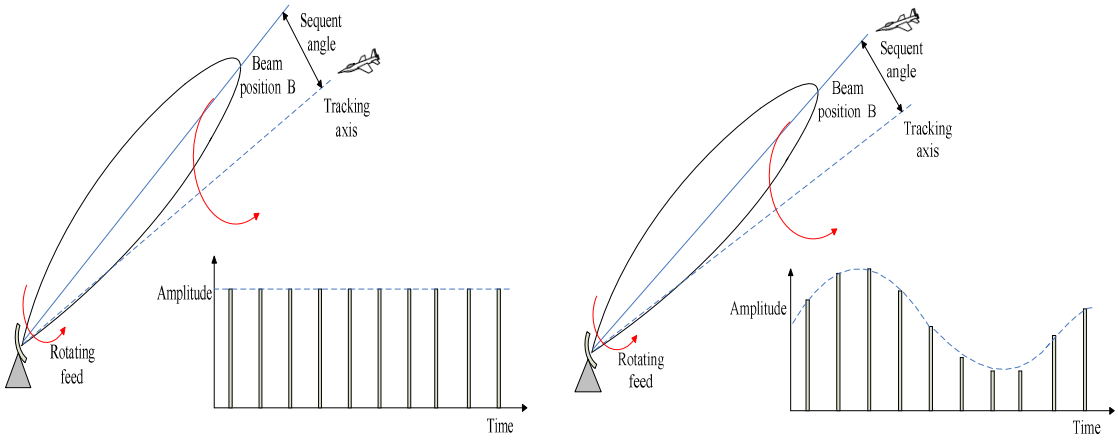

(A) (B)

Figure 2.4 Conical scan target tracking

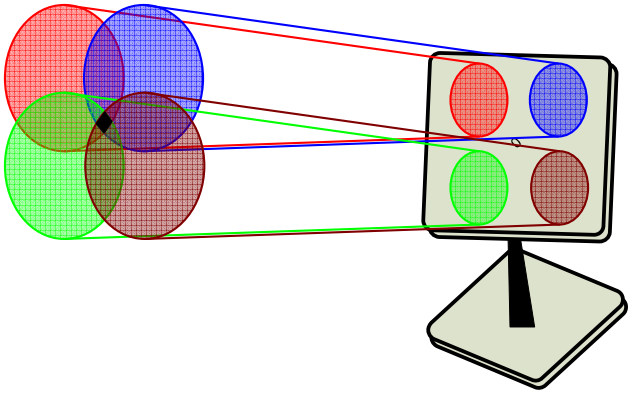

Figure 2.5 Monopulse antenna pattern

hardware for monopulse processing, since the array itself can electronically form the multiple beams needed. Three different methods can be found in the literature for the instantaneous generation of the monopulse, namely amplitude, phase, and sum and difference monopulse techniques.

2.3.2.1 Amplitude Comparison Monopulse Technique

In amplitude comparison monopulse only amplitude information is considered. The beams must be offset in angle as shown Figure 2.6 [4, 30, 31]. Note that phase is discarded in the angle sensor. For the configuration shown, angle estimation can only take place within a narrow region about boresight but with higher accuracy. The useful monopulse region can be increased by separating the beams farther but the angle measuring accuracy degrades as a result.

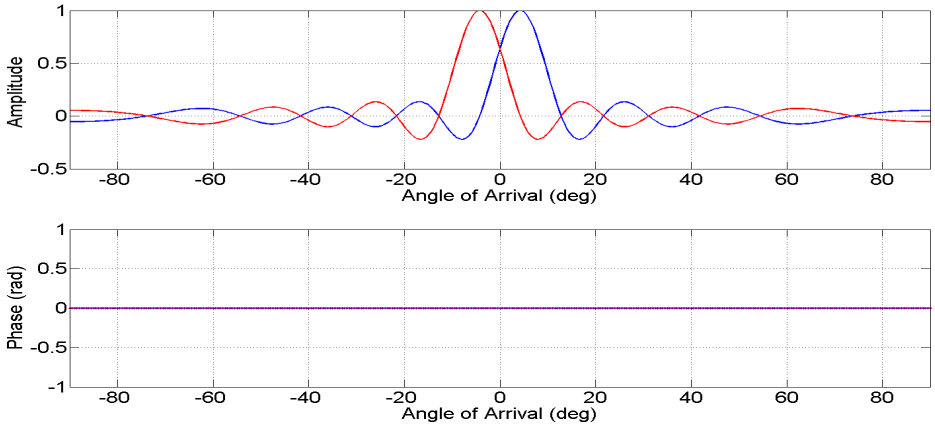

Figure 2.6 Amplitude comparison monopulse

2.3.2.2 Phase Comparison Monopulse Technique

In contrast, phase comparison monopulse utilizes only phase information. The beam patterns have identical shapes and pointing directions but with mirroring phase functions as shown in Figure 2.7 [4, 30, 31]. Although the phase functions are continuous in the entire 180^{o} range, typically the phase functions wrap around a number of times throughout this range. Thus, the angle estimation takes place in only a narrow region about boresight.

2.3.2.3 Sum and Difference Monopulse Technique

The sum beam is formed by summing the displaced beams of the amplitude comparison monopulse, whereas the difference beam is formed by taking their differences [4, 31, 32]. Note that the sum beam peaks at boresight whereas the difference beam has a null at boresight as shown in Figure 2.8.

Monopulse radars (for the rest of this thesis, the words monopulse radar is used for sum and difference monopulse radar) are commonly used in target tracking because of their angular accuracy [2, 33]. They provide superior angular accuracy and less sensitivity to fluctuation in the RCS of the target compared to other types of tracking radars [3]. However, these radars as other types or radars are affected by different types of interference which affects the target tracking process that may lead to inaccurate tracking [8].

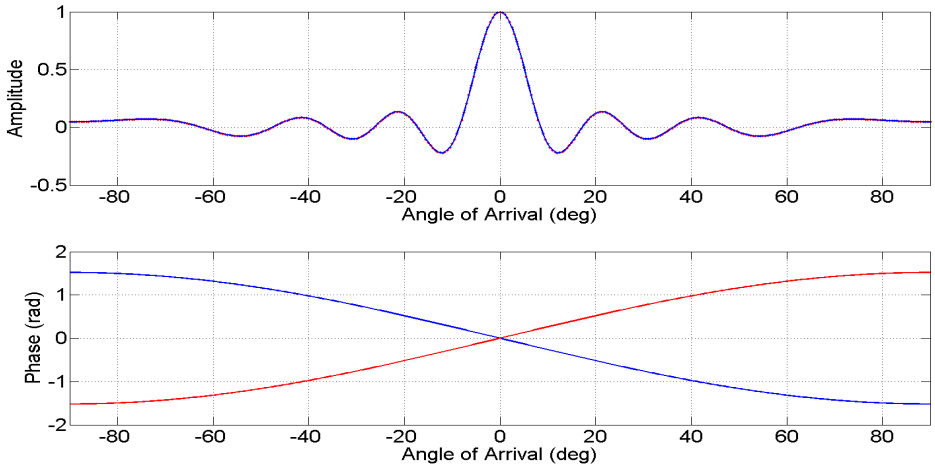

Figure 2.7 Phase comparison monopulse

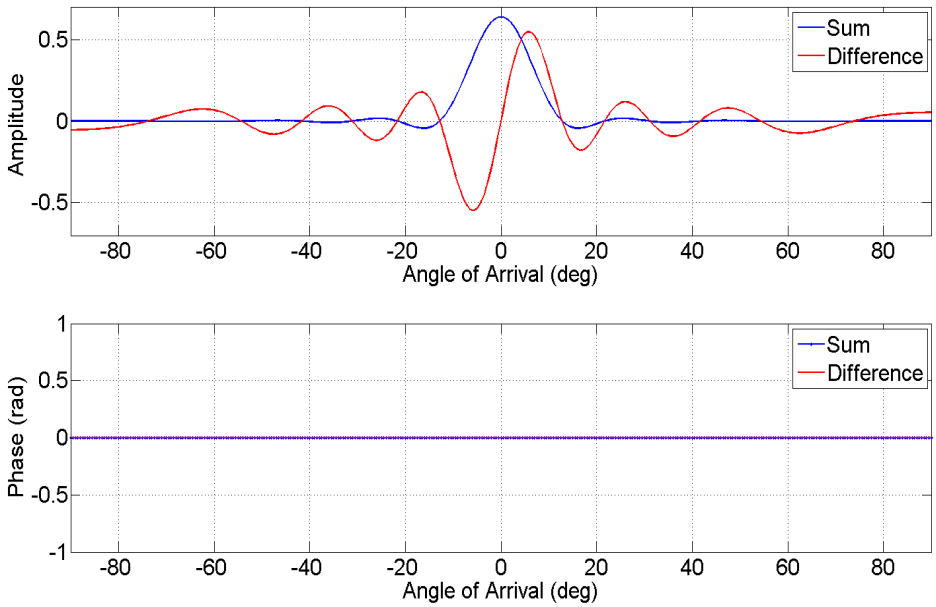

Figure 2.8 Sum and Difference monopulse

As mentioned previously, monopulse radars employ two separate feed horns on a single antenna element in order to generate two receive beams that are slightly offset in azimuth (or elevation) angle. Sum and difference outputs are formed by summing and subtracting the two beam outputs, respectively [6]. The ratio of difference to sum output voltages, called the error voltage, is then used to determine the degree of correction necessary to realign the beam axis with the target [7]. With the introduction of phased array technology, it became unnecessary to employ special hardware for monopulse processing, since the array itself can electronically form the multiple beams needed [8, 9].

With an array of antenna elements it is possible for the overall array to emulate a variety of directional characteristics without altering the geometry, position, or orientation of the individual antenna elements that make up the array. Proper phase and amplitude adjustments of an outgoing signal waveform at the individual elements focuses the radiated energy in a particular direction. Likewise, phase and amplitude weighting of incoming signals sensitizes the array to a particular direction. Utilizing phase and amplitude weighting as a means to achieve a desired steer direction is typically referred to as phase steering or beam forming [34].

Planar arrays (elements configured in a plane) permit beam forming in azimuth and elevation whereas linear arrays (elements configured on an axis) permit beam forming in one but not the other. The number of elements in an array and their spacing determine the extent of the angular and temporal resolution afforded by the array.

The particular configuration that will be considered through the rest of the thesis is a uniform linear array (ULA) having N equally spaced elements, D meters apart ($D \le \lambda/2$) as shown in Figure 2.9. Hence, for a given angle of propagation with respect to array boresight, ϕ, the time lag between wave fronts Δt impinging on neighbouring sensors is

$$\Delta t = D \sin\phi / c, \tag{2.1}$$

where c is the speed of light with approximate value 3×10^8 m/s.

Consider a monopulse radar system that transmits a sequence of M coherent pulses and samples the returns on an N element ULA. The transmitted waveform is often a linear frequency modulated (LFM) pulse having time duration T and band width Δf [10, 35, 36]. The radar collects L temporal samples from each element receiver at each pulse repetition interval (PRI), where each time sample corresponds to a range cell. The three-dimensional data cube structure shown in Figure 2.10 represents the sampled returns in a single coherent processing interval (CPI) of M pulses. A spatial snapshot $\boldsymbol{x}^{(m)}(t)$ consists of N elements of spatial data from the t^{th} range cell at a particular m pulse, where $1 < m < M$ as

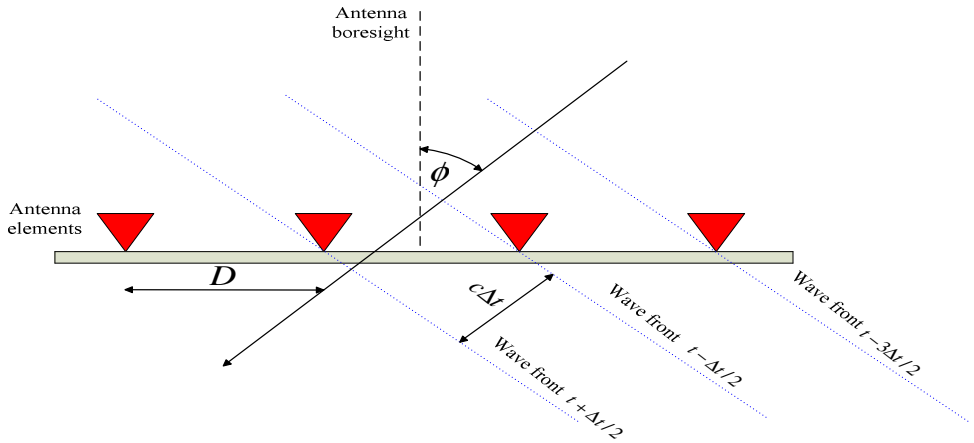

Figure 2.9 Monopulse linear antenna

$$\boldsymbol{x}^{(m)}(t) = \left[x^{(m)}(0,t)\ x^{(m)}(1,t)\ \ \ldots\ \ x^{(m)}(N-1,t)\right]^T, \tag{2.2}$$

where $x^{(m)}(n,t)$ is a sample aquired from the n^{th} receive element, representing the t^{th} range cell during the m^{th} repettion interval.

A space fast time (SFT) snapshot $\boldsymbol{X}_{SFT}(t)$ consists of k consecutive spatial snapshots in descending order, k consecutive descending columns of $\boldsymbol{x}^{(m)}(t)$:

$$\boldsymbol{X}_{SFT}(t) = \left[\boldsymbol{x}^{(m)}(t)\ \boldsymbol{x}^{(m)}(t-1)\ \ \ldots\ \boldsymbol{x}^{(m)}(t-k+1)\right]. \tag{2.3}$$

Similarly, A space slow time (SST) snapshot, $\boldsymbol{X}_{SST}(t)$, consists of stacked element data from consecutive pulses at a given range cell,

$$\boldsymbol{X}_{SST}(t) = \left[\boldsymbol{x}^{(0)}(t)\ \boldsymbol{x}^{(1)}(t)\ \ \ldots\ \ \boldsymbol{x}^{(M-1)}(t)\right]. \tag{2.4}$$

2.4 Basic Monopulse Radar Structure

In a typical monopulse radar shown in Figure 2.11, a pulsed chirp signal $c(t)$ given in (2.5) is produced from the waveform generator and up-converted to the radar carrier frequency f_c before amplification and transmission through the duplexer to the radar antenna

$$\boldsymbol{c}(t) = \exp\left(j\pi\left(\frac{F_{stop}-F_{start}}{T}\right)\left(t-\frac{T}{2}\right)^2\right), \tag{2.5}$$

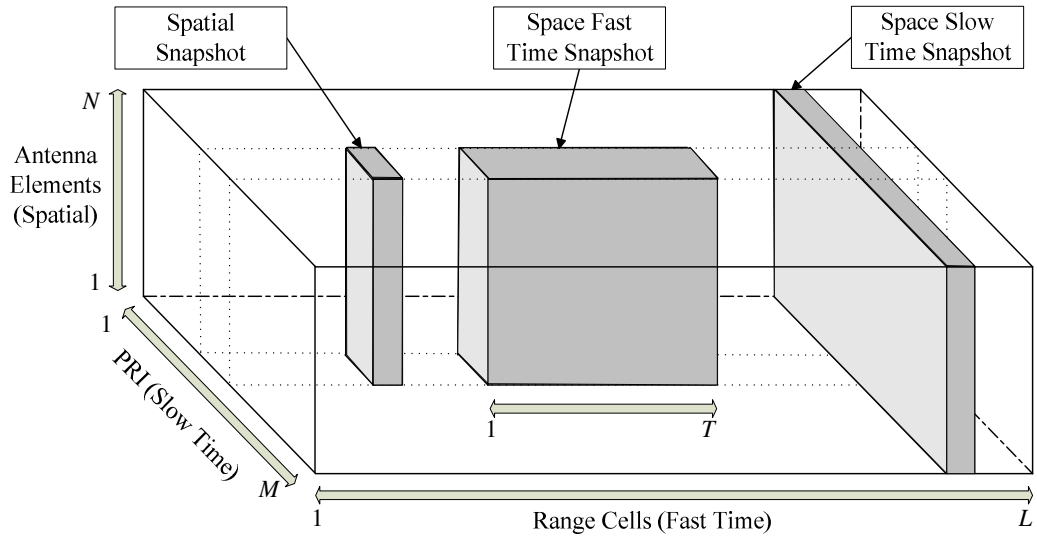

Figure 2.10 Three dimensional data cube

where t is restricted to a window $0 < t < T$, T is the chirp time duration (pulse duration), F_{start} is the chirp start frequency, and F_{stop} is the chirp stop frequency.

The received signal is down-converted through the sampler with sampling frequency F_s and passed through a Gaussian filter. The filtered data is input to a chirp matched filtering process to maximize the target return signal. The target information parameters (azimuth angle, elevation angle, and target range) are then calculated by the monopulse processor from the filtered signal. The structure of monopulse radar is repeated N times. The receiver system is considered as a parallel channel radar receiver, each channel having its own complete receiving system. All output data will be processed in only one monopulse processor.

2.5 Important Parameters of the Monopulse Processor

Before going into detail on the monopulse processor, it is important at this stage to define some of the necessary parameters as illustrated in the following subsections.

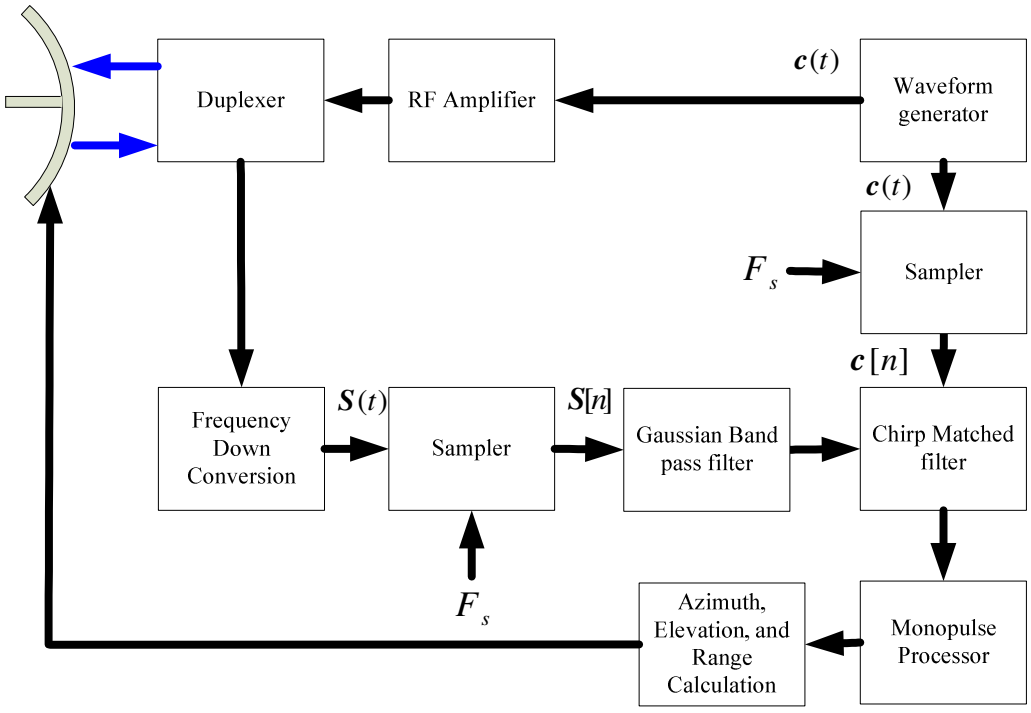

Figure 2.11 Basic structure of a monopulse radar

2.5.1 Spatial steering frequency vectors

As mentioned in subsection 2.3.2.3, a phased array monopulse processor requires the formation of sum and difference beams through the appropriate phasing of the array elements. In one method [36, 37] a standard steering vector is selected for the sum channel and its derivative with respect to spatial frequency for the difference channel

$$\boldsymbol{v}_{\Sigma} = \boldsymbol{a}(\nu_t),\ \boldsymbol{v}_{\Delta} = \left.\frac{\partial \boldsymbol{a}(\nu)}{\partial \nu}\right|_{\nu_t}, \tag{2.6}$$

where $\boldsymbol{v}_{\Sigma}$ and $\boldsymbol{v}_{\Delta}$ are the spatial steering frequency vectors for the sum and difference channel, respectively. The centre phase normalized steering vector in the look direction is defined as:

$$\boldsymbol{a}(\nu) = \frac{e^{-j\pi\nu(N-1)}}{\sqrt{N}}\left[1 \quad e^{j2\pi\nu} \ldots\ldots\ e^{j2\pi\nu(N-1)}\right]^T, \tag{2.7}$$

where ν is the spatial steering frequency, and ν_t is the spatial steering frequency snapshot at time instant t. The normalized spatial steering frequency ν is estimated from

$$\nu = f_c \Delta t = f_c D \sin\phi / c, \tag{2.8}$$

where f_c is the monopulse radar carrier frequency.

2.5.2 Monopulse Sum and Difference Outputs

The sum $z_{\Sigma}(t)$ and difference $z_{\Delta}(t)$ monopulse processor outputs are given by

$$z_{\Sigma}(t) = \boldsymbol{w}_{\Sigma}{}^{H}\boldsymbol{x}(t)\ , \quad z_{\Delta}(t) = \boldsymbol{w}_{\Delta}{}^{H}\boldsymbol{x}(t), \tag{2.9}$$

where $\boldsymbol{x}(t)$ is the $N \times 1$ spatial snapshot at time instant t at one of the M received pulses as shown in (2.2), $\boldsymbol{w}_{\Sigma}$ is the sum weight vector for the sum channel, $\boldsymbol{w}_{\Delta}$ is the difference weight vector for the difference channel, and $_H$ indicates the Hermitian. The real part of the ratio of difference to sum outputs is defined as the error voltage $\varepsilon_{\nu}(t)$ [36, 37].

2.5.3 Error voltage curve

The amplitude and phase components caused by factors that are external to the radar, such as target range, target cross-section, and medium losses, appear identically in both

sum and difference voltages. By considering a ratio of the voltages, the components that appear identically in the two voltages cancel out. Hence the real part of the ratio of difference to sum outputs is known as the error voltage $\varepsilon_v(t)$ and is defined as [36, 37]

$$\varepsilon_v(t) = \Re\left\{\frac{z_\Delta(t)}{z_\Sigma(t)}\right\}. \tag{2.10}$$

Equations (2.9) and (2.10) show that the array sensor outputs $z_\Delta(t)$ and $z_\Sigma(t)$ can be complex valued as the ratio of beam outputs is in general complex. However, the real valued ratios $\frac{z_\Delta(t)}{z_\Sigma(t)}$ correspond to a physical target and the imaginary part of the ratio should be discarded since it is primarily due to interference. Once an error voltage is estimated, it can be used in conjunction with monopulse response curve (MRC) to estimate the target angle $\hat{\phi}$ of the real angle ϕ.

2.5.4 Monopulse response curve

The mapping function, MRC, is the ratio of difference to sum beam patterns and represented the ideal error voltage response to targets arriving from a particular angular region about boresight, so MRC, $\boldsymbol{m}(\phi)$ is defined as

$$\boldsymbol{m}(\phi) = \Re\left\{\frac{\boldsymbol{W}_\Delta(\phi)}{\boldsymbol{W}_\Sigma(\phi)}\right\}, \tag{2.11}$$

where $\boldsymbol{W}_\Sigma(\phi)$ and $\boldsymbol{W}_\Delta(\phi)$ are the monopulse beam pattern for the sum processor and the difference processor, respectively. The beam pattern $\boldsymbol{W}_\Sigma(\phi)$ and $\boldsymbol{W}_\Delta(\phi)$ are defined as the response of a fixed beam former, specified by its weight the spatial weight vectors $\boldsymbol{w}_\Sigma$ and $\boldsymbol{w}_\Delta$ to an ideal signal arriving from look direction angle ϕ, respectively, and are calculated as [38, 39]:

$$\boldsymbol{W}_\Sigma(\phi) = \boldsymbol{w}_\Sigma{}^H \boldsymbol{a}(\nu), \quad \boldsymbol{W}_\Delta(\phi) = \boldsymbol{w}_\Delta{}^H \boldsymbol{a}(\nu). \tag{2.12}$$

Different methods to generate sum and difference patterns for monopulse processor are shown in Appendix A

2.6 Mathematical Modelling for Monopulse Processors

Mathematical modelling for the sum and difference weights vectors for both conventional and spatial adaptive monopulse processors are introduced in this section. Error voltage curves and also MRCs are estimated for both processors in absence of interference.

2.6.1 Conventional Monopulse Processor

The conventional processor is a non-adaptive system comprising two sets of weights set to the sum and difference weights vectors defined as [36, 40]:

$$\boldsymbol{w}_{\Sigma} = \boldsymbol{v}_{\Sigma},\ \boldsymbol{w}_{\Delta} = \boldsymbol{v}_{\Delta}. \tag{2.13}$$

Figure 2.12-A and Figure 2.12-B show example sum and difference weights patterns $\boldsymbol{w}_{\Sigma}(\phi)$ and $\boldsymbol{w}_{\Delta}(\phi)$, respectively, for a conventional monopulse processor using (2.12) and (2.13). The sum pattern has a maximum at the radar look direction which is considered at $\phi = 32^{o}$ (vertical dashed line) with number of antennas $N = 14$, while the difference pattern has a deep null in the look direction. Thus, the resultant MRC shown in Figure 2.12-C, estimated from (2.11) shows a sloped curve which is the best requirements for monopulse pattern. The error voltage curve estimated from (2.10) is shown in Figure 2.12-D. The error voltage curve $\varepsilon_{v}(t)$ and MRC are identical due to no interference. Thus the target estimated angle $\hat{\phi}$ of the real angle ϕ are identical.

A major shortcoming of conventional monopulse is that it may not provide adequate suppression of jamming and other forms of interference. Spatial adaptive monopulse has been proposed as an effective means to counter the problem of side lobe jamming and, to a limited extent, main beam jamming.[36, 40]

Adaptive processing represents a more sophisticated class of processors and typically requires solving for a set of weights $\boldsymbol{w}$ that are optimal in the mean square sense. In other words, the mean square output of the processor can be written as

$$\zeta = E\{|z(t)|^{2}\} = E\{\boldsymbol{w}^{H}\boldsymbol{X}_{SFT}\boldsymbol{X}_{SFT}^{H}\boldsymbol{w}\} = \boldsymbol{w}^{H}\boldsymbol{R}_{x}\boldsymbol{w}, \tag{2.14}$$

where $\boldsymbol{R}_{x}$ is covariance matrix. The mean output is minimized with respect to $\boldsymbol{w}$ subject

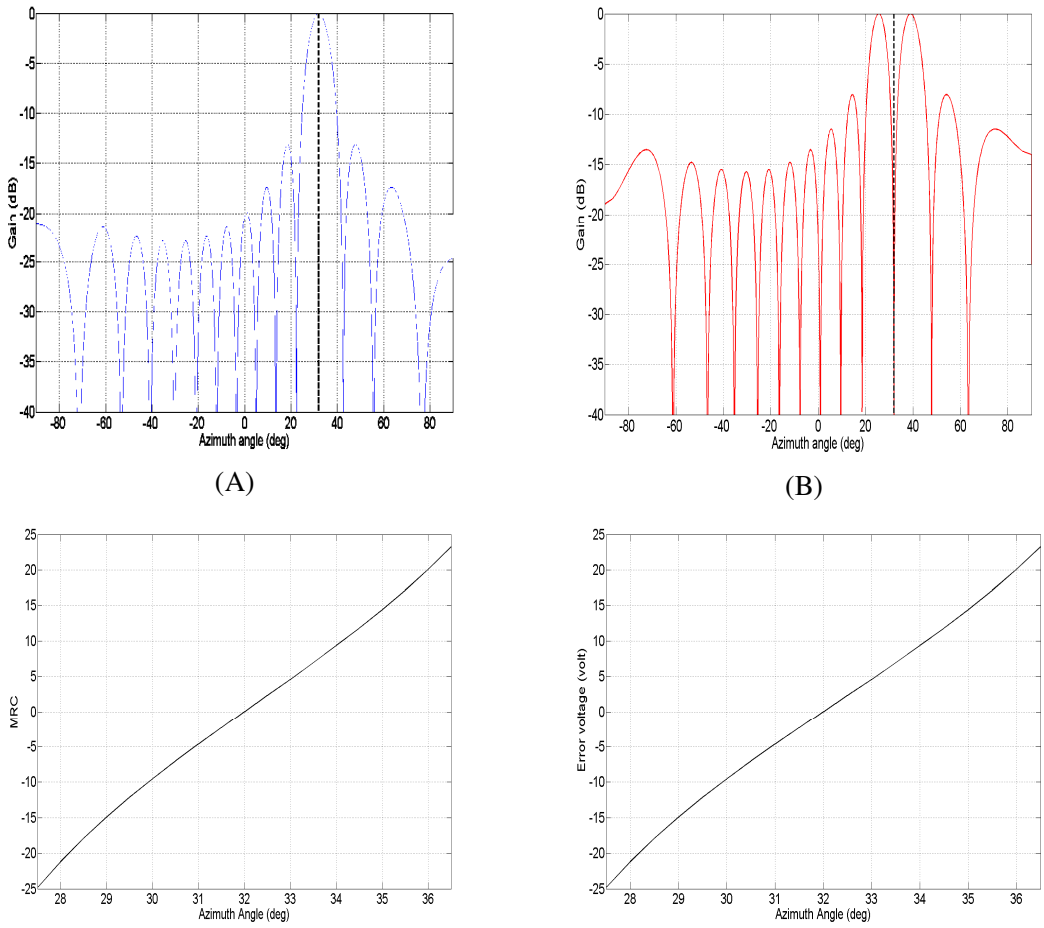

Figure 2.12 Conventional monopulse processor
(A) sum weight pattern
(B) difference weight pattern
(C) MRC
(D) error voltage

to the constraints $\boldsymbol{C}\,\boldsymbol{w} = \boldsymbol{c}$. The constraint matrix, $\boldsymbol{C}$, may consist of a set of space-time steering vectors, whose spatiotemporal locations indicate where the constraints are to be applied. The constraint vector, $\boldsymbol{c}$, contains the desired responses for signals arriving from the respective locations. The solution to the minimization problem can be expressed in closed form (assuming $\boldsymbol{R}_x^{-1}$ exists) as

$$\boldsymbol{w} = (\boldsymbol{C}\,\boldsymbol{R}_x^{-1}\boldsymbol{C}^{H})^{-1}\boldsymbol{R}_x^{-1}\boldsymbol{C}^{H}\;\boldsymbol{c}\,. \tag{2.15}$$

In a real system, the inverse of the covariance matrix $\boldsymbol{R}_x$ is estimated using the sample matrix inversion (SMI) technique [41]. Some detailed expressions on how $\boldsymbol{R}_x$ can be estimated are given in Appendix B.

The reason for using Min variance technique (MV) to estimate the set of weights $\boldsymbol{w}$ rather than other types of angle estimator such as Maximum likelihood (ML) is because MV allows the designer to exercise a great deal of control over both the spatial and temporal behaviour of the SFT sum and difference processors, thus assuring robustness by providing a means to avoid target spreading and other distorting effects. More detailed comparison between MV and ML as angle estimators in SFT is shown in Appendix C.

2.6.2 Spatial Adaptive Monopulse Processor

Several different approaches have been proposed for designing an adaptive pair of sum and difference beams, such as the maximum-likelihood approach in [42, 43], which yields a pair of beams, that optimizes a selected angle estimator. Rather than directly optimizing an angle estimator, it is possible to minimize the interference in the individual sum and difference output channels by employing linearly constrained optimization. The spatial processor comprises an adaptive sum and difference beams formed by applying sum unity gain constraints in the look direction,

$$\boldsymbol{w}_{\Sigma}^{H}\,\boldsymbol{v}_{\Sigma} = 1 \tag{2.16}$$

The sum and difference weights yields minimum variance (MV) may be written in the following form [37, 44, 45]:

$$\boldsymbol{w}_{\Sigma} = \frac{\boldsymbol{R}_x^{-1}\boldsymbol{v}_{\Sigma}}{\boldsymbol{v}_{\Sigma}^{H}\boldsymbol{R}_x^{-1}\boldsymbol{v}_{\Sigma}},\ \boldsymbol{w}_{\Delta} = \frac{\boldsymbol{R}_x^{-1}\boldsymbol{v}_{\Delta}}{\boldsymbol{v}_{\Delta}^{H}\boldsymbol{R}_x^{-1}\boldsymbol{v}_{\Delta}}, \tag{2.17}$$

where $\boldsymbol{R}_x$ is the covariance matrix [41] of the input data to the processor with diagonal loading [46, 47].

Figure 2.13-A and Figure 2.13-B show the sum and difference patterns, respectively, for spatial adaptive monopulse processor as in (2.17). These patterns look the same as the weight patterns for the conventional processor shown in Figure 2.12-A and Figure 2.12-

B since all spatial adaptive pattern work like the conventional when no interference. The spatial adaptive MRC and the error voltage shown in Figure 2.13-C and Figure 2.13-D , respectively, are similar to those shown Figure 2.12-A and Figure 2.12-B for the conventional processor but it can be noticed that it is more sensitive to error voltage change.

2.7 Basic Structure of a Monopulse Processor

The basic structure of a monopulse processor is shown in Figure 2.14. The received $s[n]$

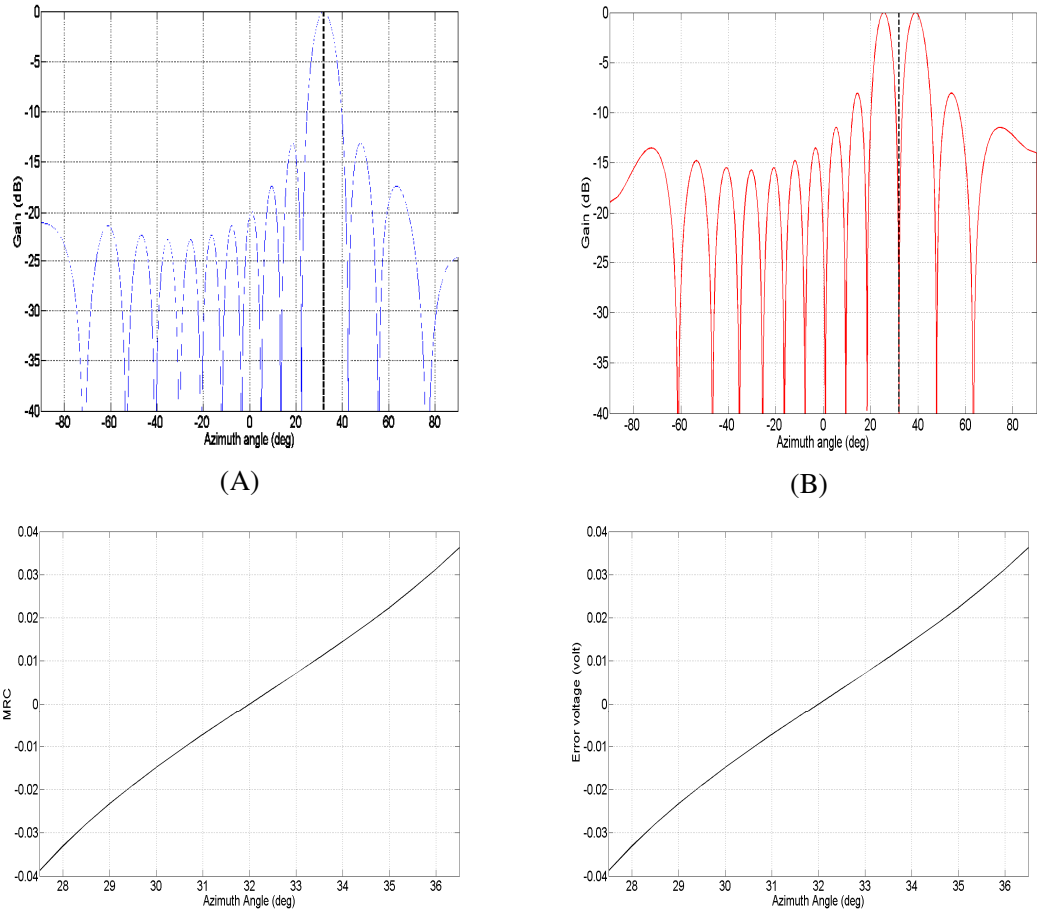

Figure 2.13 Spatial adaptive monopulse processor
(A) sum weight pattern
(B) difference weight pattern
(C) MRC
(D) error voltage

is used to form the covariance matrix $\boldsymbol{R}_x$. In the construction of $\boldsymbol{R}_x$ the processor attempts to exclude as much as possible of the target data from the input data to the processor (target range bin interval are deleted from the processed data). The weights (sum $\boldsymbol{w}_\Sigma$ and difference $\boldsymbol{w}_\Delta$) calculation depends on the type of monopulse processor (2.13), (2.17). These weights, in conjunction with the received data $s[n]$, are used to form the sum and difference outputs $z_\Sigma(l)$ and $z_\Delta(l)$, respectively, from (2.9). The sum output $z_\Sigma(l)$ is considered as the processor output which is used to show the existence of a target and to determine the target range. The weights $\boldsymbol{w}_\Sigma$ and $\boldsymbol{w}_\Delta$ are also used to calculate the monopulse beam pattern $\boldsymbol{W}_\Sigma(\phi)$ and $\boldsymbol{W}_\Delta(\phi)$ which are used to determine the MRC (2.11), (2.12). The MRC can be viewed as the ratio of difference to sum beam patterns that represents the ideal error voltage response to targets arriving from a particular angular region about its boresight. The sum and difference outputs $z_\Sigma(l)$ and $z_\Delta(l)$ are used to calculate the error voltage $\varepsilon_v(l)$ from (2.10). The error voltage $\varepsilon_v(l)$ is converted to an angular form via the mapping function MRC to compute the target look direction angle ϕ.

2.8 Monopulse Performance Measures

Angle estimation performance and interference mitigation performance are the most

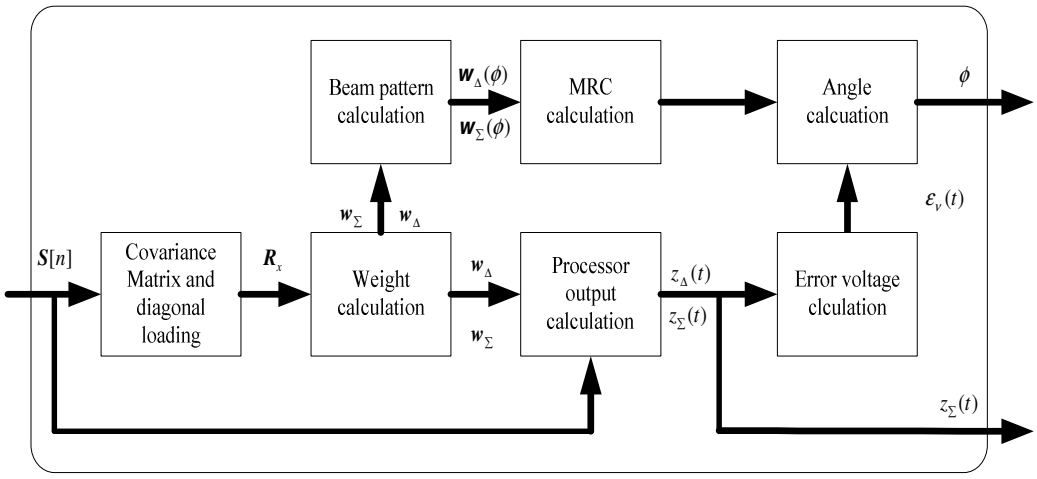

Figure 2.14 Basic structure of a monopulse processor

important performance measures for the monopulse processor. These two performances are explained in the following subsections.

2.8.1 Angle Estimation Performance

Angle estimation performance is a formal methodology for assessing monopulse performance. One particularly useful performance measure for angle estimation techniques is the root mean square (RMS) of the angle error. The RMS of the angle error is equal to the standard deviation of the angle error (STDAE) for unbiased estimator ($E\{\varepsilon_\phi\}=0$). The STDAE is determined using a target that is injected randomly across the range and angle within the main beam. The corresponding angle error is then averaged over the range and is defined as[37]:

$$\sigma_{\varepsilon_\phi}=\sqrt{E\{\left|\varepsilon_\phi\right|^2\}}\,, \tag{2.18}$$

where $\varepsilon_\phi=\hat{\phi}-\phi$, ϕ is the target angle, and $\hat{\phi}$ is the estimate angle. When there is only one target signal without any distortion signal (jamming signal, clutter, thermal noise, and terrain scattering interference), both ϕ and $\hat{\phi}$ are nearly equal, hence the STDAE will be close to zero.

2.8.2 Interference Mitigation Performance

Output to interference and noise ratio (*OINR*) is used to compare the mitigation performance for the different monopulse processors. *OINR* [10, 48] is defined as the ratio of the processor output power to the noise power

$$OINR=\frac{\mathrm{E}\left\{\left|z_i\right|^2\right\}}{\sigma_{\mathrm{n}}^2}, \tag{2.19}$$

where z_i is the output of the processor when only interference is present and σ_n^2 is the noise power. A lower *OINR* value implies improved mitigation performance and vice versa.

2.9 Simulated and Real Monopulse Data

The monopulse radar parameters, simulated target parameters, real and simulated

jamming signal parameters that are used throughout this thesis for simulation purposes are expressed in the following subsections:

2.9.1 Simulated monopulse radar

The computer based simulations that will be used in this thesis are extracted from DARPA/Navy Mountaintop Program to nearly emulate a real airborne monopulse tracking radar [49, 50]. These simulations comprise of a monopulse chirp radar with an ULA of 14 elements spaced 1/3 meters. The radar comprises a chirp pulse width T of 100 microseconds, a pulse repetition interval (PRI) of 1.6 milliseconds, and the chirp pulse width W is 500 MHz using a carrier frequency f_c 435 MHz. Some of these monopulse radar parameters for complete PRI are shown in Figure 2.15. A 200 kHz Gaussian band pass filter exists at the front end of each of the N receiving channels associated with each antenna elements to filter the incoming data. The incoming baseband signals are sampled with sampling frequency F_s 1 MHz. It is assumed that the radar operating range is 100:200 range bins with a starting window at 865 microseconds with window duration of 403 microseconds.

2.9.2 Simulated Target Signal

The target received signal $S(t)$ may be expressed in the radar baseband as:

$$S(t)=\begin{cases}\left[\left(Ae^{-j2\pi\phi_0}\, e^{j\pi\left(\frac{F_{stop}-F_{start}}{T}\right)\left(t-T_{start}-\frac{T}{2}\right)^2}\right).f_d\right]\times f_\phi & T_{start}<t<T_{start}+T \\ 0 & elsewhere\end{cases}, \qquad (2.20)$$

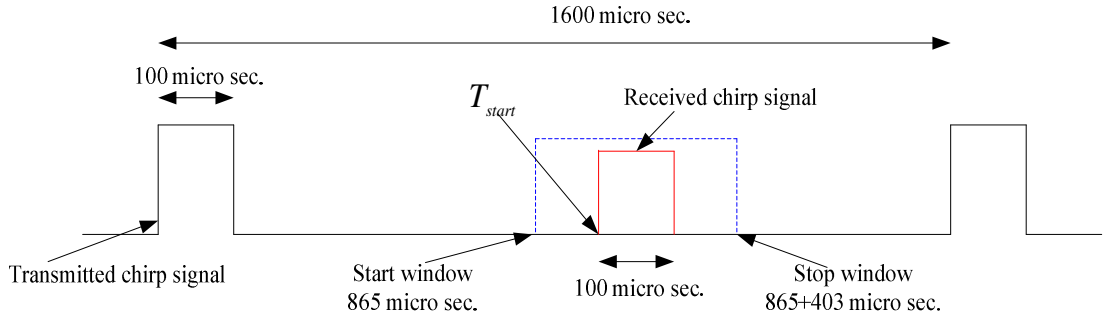

Figure 2.15 Complete pulse repetition interval

where A is the received signal amplitude, ϕ_o is a random phase shift, (.) is the dot product, $(\times)$ is the cross product, and T_{start} is the start time of the returned pulse that passes through a band pass Gaussian filter. The start time T_{start} depends on the target range R_t can be estimated as

$$T_{start} = \frac{2R_t}{c}. \tag{2.21}$$

As indicated in (2.20), the Doppler shift and delay effect on the target chirp signal is determined by the dot product of the chirp signal by the Doppler vector $\boldsymbol{f}_d$ defined as

$$\boldsymbol{f}_d = \exp\left(j2\pi f_d (t\boldsymbol{I}_L - T_{start})\right) \qquad T_{start} < t < T_{start} + T, \tag{2.22}$$

where f_d is the target Doppler frequency $\boldsymbol{I}_L$ is a $1\times L$ unitary vector.

For the phased array receiving antenna, an antenna phase factor $\boldsymbol{f}_\phi$ is introduced as

$$\boldsymbol{f}_\phi = \exp\left(-j2\pi f_c (T_{start}\boldsymbol{I}_N - \boldsymbol{n}_{array}\Delta t)\right), \tag{2.23}$$

where $\boldsymbol{n}_{array}$ is a vector represented as $\{0, 1, \ldots, N-1\}$ and $\boldsymbol{I}_N$ is a $1\times N$ unitary vector.

The down-converted received signal passes through a band limited Gaussian filter before passing through the chirp matched filter to maximize the target return signal. The target information parameters are then calculated by the monopulse processor (conventional monopulse and spatial adaptive processor) from $z_\Sigma(l)$.

In the thesis, the simulated desired target is considered to be at range bin=150 at different angles from the look direction with a Doppler frequency of 150 Hz at different signal to noise ratio (SNR).

2.9.3 Simulated and Real Jamming Signals

A distortion produced when man made high power interference (jamming) with interference to noise ratio (INR) is introduced to the radar processor through the radar antenna main lobe (main lobe interference) or antenna side lobe (side lobe interference) may lead to errors in the target tracking angles resulting in target mistracking. The mathematical modelling and jamming scenarios for the simulated and real interference are shown in the following subsections.

2.9.3.1 Simulated Jamming Data

Barrage noise jamming $\boldsymbol{N}_{jam}$ [1, 51] is the most common form of hostile interference. Such interference emanates from a spatially localized source and is temporally uncorrelated from sample to sample as well as between pulse repetition intervals. It is modelled as the product of a spatial steering vector $\boldsymbol{n}_{jam}(t)$ and the jamming spatial steering vector $\boldsymbol{a}_{jam}(\nu)$:

$$\boldsymbol{N}_{jam} = \boldsymbol{n}_{jam}(t)\,\boldsymbol{a}_{jam}(\nu), \tag{2.24}$$

where $\boldsymbol{n}_{jam}(t)$ is complex white Gaussian noise vector with zero mean, and the jamming spatial steering vector $\boldsymbol{a}_{jam}(\nu)$ is defined as

$$\boldsymbol{a}_{jam}(\nu_{jam}) = \exp\left(j\,2\pi\nu_{jam}\,\boldsymbol{N}_{array}\right), \tag{2.25}$$

where ν_{jam} is the normalized jamming spatial steering frequency estimated from

$$\nu_{jam} = f_c\,D\,\sin\phi_{jam}/c, \tag{2.26}$$

where ϕ_{jam} is the jamming angle w.r.t the radar antenna boresight.

The power of each component of $\boldsymbol{n}_{jam}(t)$ is assumed to be σ^2_{jam}. The white Gaussian vector $\boldsymbol{n}_{jam}(t)$ is a complex signal with real and imaginary parts drawn from a Gaussian distribution with zero mean and unit variance. For a white Gaussian $\boldsymbol{n}_{jam}(t)$ of length L (where L is the radar range gates), the barrage noise jamming $\boldsymbol{N}_{jam}$ is of size $N \times L$.

A jamming signal with different interference noise ratio (INR) with two angles scenario, first at angle 32^o from the look direction (main beam jamming) and second at angle 62^o from the look direction (side lobe beam jamming) will be introduced later in the thesis.

2.9.3.2 Real Jamming Data

The real jamming data is an experimental dataset stap3001 containing a direct-path barrage noise jammer at 42^o that was collected as part of the DARPA/Navy Mountaintop Program [45, 49, 50]. The real jamming radar data "File stap3001" is pseudo-random signal noise with a bandwidth of 600 kHz (broadband relative to the

radar's bandwidth, so it appears as broadband barrage jamming). The jammer was sited on a mountain at a range of 65 km from the radar, and at an azimuth of 302^o relative to true North. Therefore the jammer is at angle 42^o from the radar look direction so the interference enters the radar through the side lobe.

2.10 Conclusion

This chapter has introduced the monopulse radars using sum and difference processing. These radars are commonly used in target tracking because of their angular accuracy. They provide superior angular accuracy and less sensitivity to fluctuation in RCS of the target compared to other types of tracking radars. However, these radars are affected by different types of interference which affects the target tracking process and may lead to inaccurate tracking.

For phased array monopulse radar, the error voltage (the ratio of difference to sum output voltages) is used to determine the degree of correction necessary to realign the beam axis with the target. A conventional monopulse processor for phased array radar is obtained by appropriately phasing the individual array channels to obtain sum and difference outputs. The ratio of difference to sum outputs provides the measure by which the angle offset from the beam axis (i.e., look direction) is determined. The updated angle measurement is used to compute phases for the channels so as to realign the beam axis with the target. Consequently the radar is affected by different types of interference that may cause inaccurate tracking.

The next chapter will present the signal processing algorithms that will be used to mitigate the interference problem in monopulse radar. These algorithms will be used later in the thesis to reduce the interferences and to enhance the tracking performance.

3. FrFT and EMD Algorithms

3.1 Introduction

This chapter reviews the fractional Fourier transform (FrFT) and empirical mode decomposition (EMD) algorithms. Both algorithms are used in the remainder of this thesis in the design and implementation of advanced monopulse radar systems that aim to overcome different types of interference in tracking radars. A historical background and applications of the two algorithms are provided.

The word "fraction" is widely used in different fields of science such as fractional derivatives in mathematics, fractal dimension in geometry, fractal noise, fractional space equalisers and fractional transformations in signal processing [52-55]. In general, "fractional" means that some parameter has no longer an integer value. The idea of fractional powers of the Fourier transform operator appeared as early as 1929 [56]. In the mathematics literature, a generalization of the Fourier transform known as FrFT was re-introduced by Namias for applications in quantum mechanics in 1980 [57] but it was not widely recognized until it was independently reinvented by several groups of researchers [58-61]. State-of-the art collections for the FrFT theory including computational cost and applications can be found in [56, 62-65].

The FrFT is used in many applications such as:

Optics: quantum optics, optical diffraction theory, optical beam propagation (including lasers) [59, 62, 66]. *Image processing*: image recovery, restoration, enhancement [67, 68], application on SAR/ISAR and Sonar imaging [69-72]. *Signal processing*: signal recovery, signal detectors, correlation, convolution, synthesis, study signal time-frequency distributions, pattern recognition, beam forming, wave front propagation and reconstruction, speech processing , digital watermarking, encryption and compression, multiplexing, tomography, blind source separation and energy localization problems,

high resolution trigonometric interpolation, analyzing sequences with non-integer periodic components (computing solar positions) , pre-processing for neural networks, three dimensional transparent object recognition, numerical holography computing ,multiple FrFT holography, securing information in digital holography [73-77].

EMD is *Empirical* because it lacks theoretical foundations. *Mode* relates to the intrinsic mode functions which represent the oscillation modes embedded in the data. *Decomposition* refers to decomposing the original signal to IMFs and residual.

The idea of EMD, which is also known as the Hilbert Huang transformation (HHT), appeared in 1998 [78] and was the winner of the 2002 NASA Government Invention of the Year [79]. It is recognized by NASA Headquarters inventions and contributions board as "One of the most important discoveries in the field of applied mathematics in NASA history". Norden E. Huang who works for NASA Goddard Space Flight Center reviewed the non-stationary data processing methods as the spectrogram, wavelet analysis, Wigner-Ville distribution, evolutionary spectrum, empirical orthogonal function expansion (EOF), and other miscellaneous methods, and then showed the superior performance of EMD over these methods [80].

EMD is used in many applications such as: nonlinear wave evolution, climate cycles, earthquake engineering, submarine design, structural damage detection, satellite data analysis, turbulence flow, blood pressure variations and heart arrhythmia, non-destructive testing, structural health monitoring, signal enhancement, or economic data analysis [81-84].

The remainder of the chapter comprises two main parts. In Section 3.2 the FrFT is reviewed. In this section definitions, mathematical formula and some applications of the FrFT are given along with its relation to other transforms. The classical and bivariate definitions of EMD, EMD Detrending and Thresholding algorithm, invariant EMD thresholding and denoising algorithms, and EMD application are reviewed in Section 3.3. Section 3.4 conclude this chapter.

3.2 Fractional Fourier Transform (FrFT)

The FrFT is the generalized formula for the Fourier transform that transforms a function into an intermediate domain between time and frequency [85, 86].

3.2.1 Definition and Mathematical Formula

The FrFT of order a of an arbitrary function $x(t)$, with an angle θ, is defined as [87]:

$$X_\theta(t_a) = \int_{-\infty}^{\infty} x(t) K_\theta(t_a, t) dt, \tag{3.1}$$

where $K_\theta(t_a,t)$ is the transformation Kernel, t_a is the variable in the a^{th} FrFD, and $\theta = a\pi/2$ with $a \in \Re$. $K_\theta(t_a,t)$ is defined as[88]:

$$K_\theta(t_a,t) = \begin{cases} \sqrt{\dfrac{1-j\cot\theta}{2\pi}} \exp\left(j\dfrac{t^2+t_a^2}{2}\cot\theta - jt_a t \csc\theta \right) & \text{if } \theta \text{ is not a multiple of } \pi \\ \delta(t-t_a) & \text{if } \theta \text{ is a multiple of } 2\pi \\ \delta(t+t_a) & \text{if } \theta+\pi \text{ is a multiple of } 2\pi \end{cases} \tag{3.2}$$

The fractional transform operator $F^a[x(t)]$ is used to transform the time domain signal $x(t)$ to the fractional Fourier domain (FrFD) $X_\theta(t_a)$ that represents an intermediate domain between time and frequency as illustrated in Figure 3.1 . Thus the signal $X_\theta(t_a)$ in the FrFD has combined components of the time and frequency.

Figure 3.1 illustrates the relationships between the time, and frequency outputs from the FrFT, F^a when the fractional order a in an integer as:

$$F^a[x(t)] = \begin{cases} F^0[x(t)] = x(t) & for \quad a = 0 \longrightarrow \text{Time domain} \\ F^1[x(t)] = X(f) & for \quad a = 1 \longrightarrow \text{Frequency domain} \\ F^2[x(t)] = x(-t) & for \quad a = 2 \longrightarrow \text{Reverse Time domain} \\ F^3[x(t)] = X(-f) & for \quad a = 3 \longrightarrow \text{Reverse Frequency domain} \end{cases} \tag{3.3}$$

It can also seen in Figure 3.1 that $F^4[x(t)] = F^0[x(t)] = x(t)$.

The inverse FrFT is achieved using the same transformation equations (3.1) and (3.2) using negative transformation order $-a$ thus the inverse fractional transform function

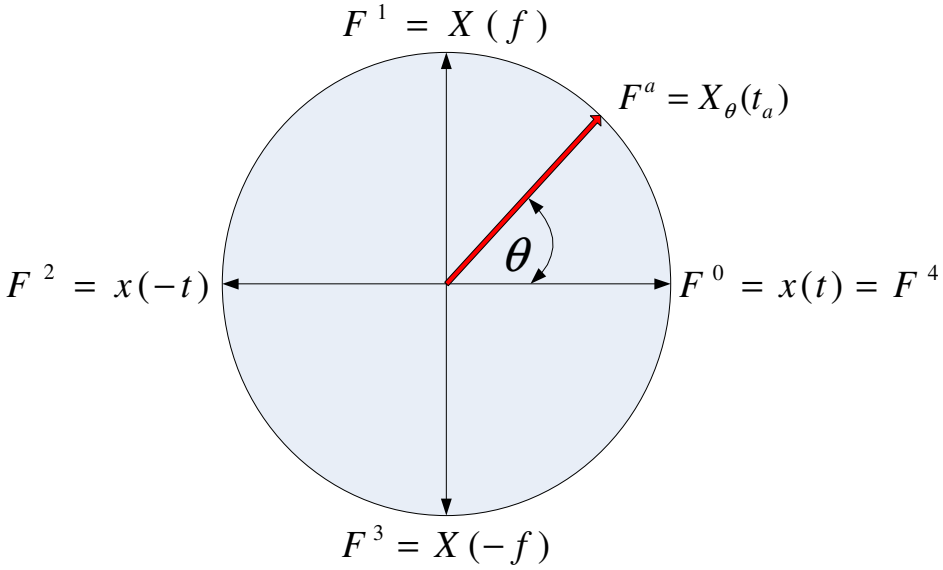

Figure 3.1 Signal $x(t)$ at different transformation order a

$F^{-a}[X_{\theta}(t_a)]$ is used to transform the FrFD $X_{\theta}(t_a)$ back to the time domain signal $x(t)$. To understand the effect of different transformation orders a on a signal $x(t)$, a linear chirp signal with the following parameters :- starting frequency of 5 Hz, stopping frequency of 100 Hz, chirp period of 0.8 sec, and sampling frequency of 1 kHz; time window 5 sec, and the chirp start at 1.5 sec is transformed using different transformation orders $-1 < a < 1$ (transformation angles $-\frac{\pi}{2} < \theta < \frac{\pi}{2}$). The resulting transformations are illustrated in Figure 3.2-A for orders in the range $-1 < a < 1$. As expected the transformation becomes the FT of the chirp signal when $a = 1$ as seen in Figure 3.2-B with bandwidth 95 Hz while the transformation is the original time representation at $a = 0$ as seen in Figure 3.2-C with chirp duration 0.8 sec and starts at 1.5 sec. As indicated in Figure 3.2-D at $a = -0.6588$, the chirp signal transformation reaches the narrowest band width with a spike at the fractional sample 2194 which is the peak position fractional sample. This order ($a = -0.6588$) is called optimum FrFT order a_{opt} (or the angle of rotation $\theta_{opt} = a_{opt}\pi/2$). At this order the FrFT is tuned to provide an optimal response to the given linear chirp signal.

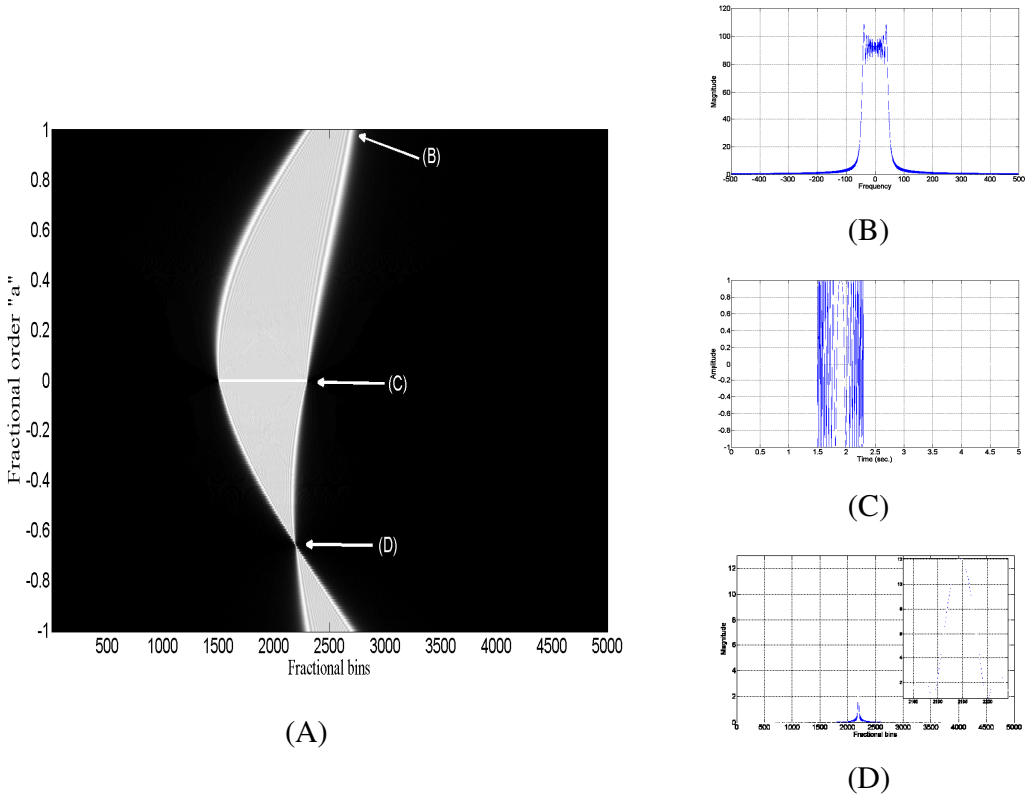

Figure 3.2 FrFT of a chirp signal with different transformation order a

3.2.2 Normalized FrFT

In the FrFT kernel transformation formula (3.2), the exponential term contains an addition process between t and t_a. This process is dimensionally incorrect because t dimension is in sec. (time domain) and t_a dimension is something between sec. and Hz (FrFD). A normalization factor $S = \sqrt{\mathrm{K}}$ is added to the kernel formula to resolve this incorrect dimensions problem. The normalized coordinates for t and t_a are u and u_a, respectively, where u and u_a are defined from

$$t = \frac{u}{S} = \frac{u}{\sqrt{\mathrm{K}}}, \text{ and} \qquad (3.4)$$

$$t_a = u_a S = u_a \sqrt{\mathrm{K}}.$$

K is defined as

$$\mathrm{K} = \frac{\tau}{f_\tau}, \tag{3.5}$$

where τ denotes time variable and f_τ denotes frequency counterpart of τ.

Hence the normalized FrFT kernel (3.2) can be re-written in the form

$$K_\theta(u_a,u)=\begin{cases}\sqrt{\dfrac{1-j\cot\theta}{2\pi}}\exp\left(j\dfrac{(u^2/\mathrm{K})+(u_a^{\,2}\mathrm{K})}{2}\cot\theta - j\,u_a u\csc\theta\right) & \text{if } \theta \text{ is not a multiple of } \pi \\ \delta(u-u_a) & \text{if } \theta \text{ is a multiple of } 2\pi \\ \delta(u+u_a) & \text{if } \theta+\pi \text{ is a multiple of } 2\pi \end{cases} \tag{3.6}$$

Thus the normalized FrFT formula is now defined as

$$X_\theta(u_a) = \frac{1}{\sqrt{\mathrm{K}}}\int_{-\infty}^{\infty} x(u)K_\theta(u_a,u)du\,. \tag{3.7}$$

For a sampled signal $\boldsymbol{x}[u]$ with a sampling period T_p and sampling frequency $F_s = 1/T_p$, the frequency axis is defined as $[-F_s/2, F_s/2]$ and the timeline axis is defined in the period $[-t_s/2, t_s/2]$ as

$$t_s = LT_p\,, \tag{3.8}$$

where L is the number of samples.

A discrete definition of K called K_d is written in the form

$$\mathrm{K}_d = t_s/F_s\,. \tag{3.9}$$

Hence the normalized discrete FrFT formula of $\boldsymbol{x}[n]$ is defined as

$$K_\theta[u'_a,u']=\begin{cases}\sqrt{\dfrac{1-j\cot\theta}{2\pi}}\exp\left(j\dfrac{(u'^2/\mathrm{K}_d)+(u'^2_a\mathrm{K}_d)}{2}\cot\theta - j\,u'_a u'\csc\theta\right) & \text{if } \theta \text{ is not a multiple of } \pi \\ \delta(u'-u'_a) & \text{if } \theta \text{ is a multiple of } 2\pi \\ \delta(u'+u'_a) & \text{if } \theta+\pi \text{ is a multiple of } 2\pi \end{cases} \tag{3.10}$$

where u' and u'_a are the discrete representation for u and u_a, respectively.

$$X_\theta[u_a] = \frac{1}{\sqrt{\mathrm{K}_d}}\sum_{-L/2}^{L/2} x[u]K_\theta[u'_a,u']. \tag{3.11}$$

3.2.3 Discrete FrFT Matrix

The discrete FT matrix $\overline{\boldsymbol{F}}$ is a complex matrix of values around the unit circle. The product of the matrix $\overline{\boldsymbol{F}}$ with a vector computes the discrete FT of this vector. The discrete FrFT matrix $\overline{\boldsymbol{F}}^{a}$ is used to transform a vector into the a^{th} FrFD. Note that at $a = 1$ the discrete FrFT matrix $\overline{\boldsymbol{F}}^{a}$ is identical to a discrete FT (DFT) matrix $\overline{\boldsymbol{F}}$.

Several publications [87, 89-91] proposing a definition for the discrete FrFT have appeared, but not all of these publications satisfy the following properties: unitarity, index additivty, reduction to the discrete FT when the order is equal to unity, and approximation of the continuous FrFT. The definition of the discrete FrFT matrix that satisfies all the previous properties is the spectral expansion given as [87]

$$\overline{\boldsymbol{F}}^{a}[u'_a, u'] = \sum_{k=0,\, k\neq(L-1+L \bmod 2)}^{L} \upsilon_k[u'_a] e^{-j\frac{\pi}{2}k\,a}\, \upsilon_k[u'], \tag{3.12}$$

where $\upsilon_k[u']$ is the k^{th} discrete Hermite-Gaussian function. The Hermite-Gaussian functions are known to be the eigenfunctions of the FT operator. The $\exp(-j\frac{\pi}{2}k\,a)$ is the a^{th} power of eigenvalue $\lambda_k = \exp(-j\frac{\pi}{2}k)$ of the ordinary FT. The particular range of summation is due to the fact that an eigenvector doesn't exist with $L-1$ or L zero crossing when L is even or odd, respectively. The discrete Hermite-Gaussian function can be written as

$$\upsilon_k[u'_a] = \frac{2^{1/4}}{\sqrt{2^k\, k!}} H_k(\sqrt{2\pi}u'_a) \exp(-\pi u'^{2}_a), \tag{3.13}$$

where υ_k is the k^{th} discrete Hermite polynomial having k real zeros.

3.2.4 Optimum FrFD of a Chirp Signal

The FrFT is able to process linear chirp signals better than the ordinary FT. This is because a linear chirp signal forms a diagonal line in the time-frequency plane, and therefore, there exists an order of transformation in which such signals become compact

as shown in Figure 3.3. Figure 3.3 shows the time-frequency representation of the previous linear chirp signal. It is clear that the chirp starts at time 1.5 sec and ends at 2.3 sec. and the chirp frequency from -45 Hz to 45 Hz. The optimal fractional domain (black line) is the domain at which this chirp appears as a spike.

Thus the idea of the transformation optimization process is that the optimum FrFT order a_{opt} (or the angle of rotation $\theta_{opt} = a_{opt}\pi/2$) is used to tune the transform to provide an optimal response to a given linear chirp signal. For a general linear chirp, $\exp[j2\pi(\gamma t^2 + \varepsilon t + \rho)]$, it is the chirp rate parameter γ to which the transform order is matched. When the axis rotation is matched to the chirp rate γ of the signal, the magnitude response reaches its maximum [62, 92].

For a sampled version of the general linear chirp signal an expression for the optimum order value, a_{opt}, may be written as [92]:

$$a_{opt} = -\frac{2}{\pi}\tan^{-1}\left(\frac{\delta f / \delta t}{2\gamma}\right) = -\frac{2}{\pi}\tan^{-1}\left(\frac{F_s^2 / N}{2\gamma}\right), \tag{3.14}$$

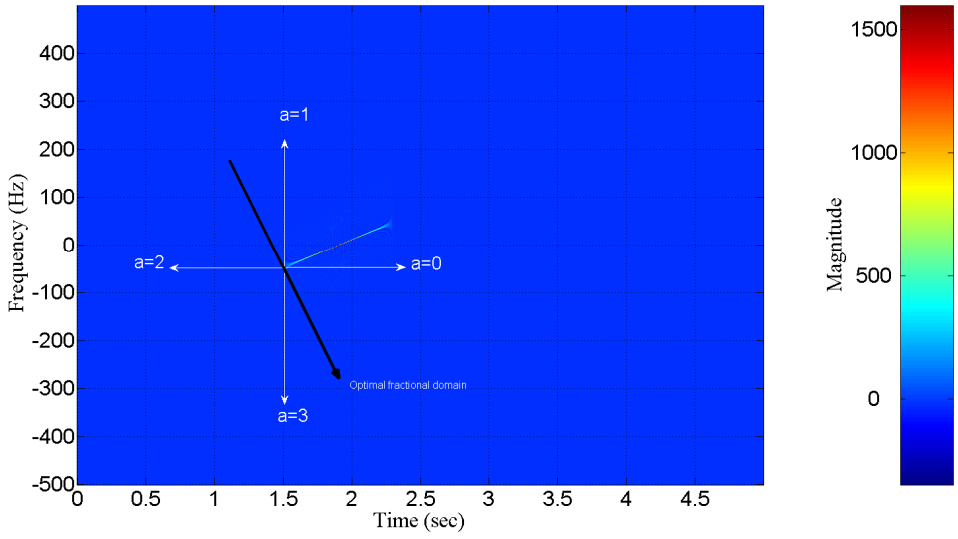

Figure 3.3 Time-frequency plane for chirp signal

where δf is the frequency resolution $\left(\delta f = F_s / L\right)$, δt is the time resolution $\left(\delta t = 1 / F_s\right)$, and F_s is the sampling frequency. Detail descriptions about the relation between the chirp rate γ and the optimum FrFT index a_{opt} shown in (3.14) is described in Appendix D.

3.2.5 Peak Position of a Chirp Signal in the FrFD

The shape of the magnitude of the chirp radar received signal in the FrFD using the transmitted chirp radar information depends on the transformation order a that the chirp radar signal is transformed to a compact form using the FrFT with optimal order a_{opt} [85]. The optimum FrFT produces a narrow peak for a certain chirp signal, however for processing purposes the knowledge of the position of the peak in the FrFD is required. This position, in terms of sample number, depends on various discrete signal parameters. The peak position P_p of a chirp signal in the FrFD (compact form) is computed as [93]:

$$P_p = \sin(\vartheta_{opt}) \left[\frac{F_{start}}{\delta f} + \frac{\Delta f \ (L / M_T)}{2 \ \delta f} \right] - \cos(\vartheta_{opt}) \, t_{st} \,, \tag{3.15}$$

where M_T is the number of samples in the chirp signal with pulse width T, ϑ_{opt} is $360^o - \theta_{opt}$, and t_{st} is the chirp start time sampling number. Detail descriptions how to estimate the peak position P_p of a chirp signal in the optimum FrFD in (3.15) is described in Appendix E.

Applying the chirp signal parameters used in subsection 3.2.1 and using the optimum transformation angle θ_{opt} in (3.15), a spike is expected at fractional sample 2194. This is confirmed by Figure 3.2-D.

3.2.6 Some Important Properties of FrFT

Similar to the FT, the FrFT has basic properties such as linearity, translation, modulation, scaling, conjugation, duality, and convolution. Many references [62, 63]

introduce these properties in the fractional domain and compute the FrFT for some special functions including rectangular, Dirac, unit step, sinc, exponential. The FrFT of some of these elementary functions are presented in Appendix F. The following background concentrates on the properties and operations that are relevant to this thesis:

3.2.6.1 Shift operation and Convolution/Correlation in the FrFT

The FrFT is a shift variant transform [62, 63]. In the FrFT, if a function is shifted in time or multiplied by an exponential, it results in a mixture of time and frequency components given a is not an integer.

Define two functions f and g with f_a the FrFT of f and g_a the FrFT of g. For $f, g \in \mathcal{L}$ and $\theta \in \Re$ we have[63]:

Shift rule: if $g(t) = f(t + \delta_t)$ then

$$g_a(t_a) = e^{i\delta_t \sin\theta (t_a + \frac{1}{2}\delta_t \cos\theta)} f_a(t_a + \delta_t \cos\theta). \tag{3.16}$$

Exponential rule: if $g(t) = e^{i\delta_t t} f(t)$ then,

$$g_a(t_a) = e^{i\delta_t \cos\theta (f_t + \frac{1}{2}\delta_t \sin\theta)} f_a(t_a + \delta_t \sin\theta). \tag{3.17}$$

Convolution rule: $f(t) *_a g(t)$ definition is

$$f(t) *_a g(t) = F^{-1}\left(g_{a+1}(t_a) f_{a+1}(-t_a)\right). \tag{3.18}$$

Cross correlation rule: $f(t) \otimes_a g(t)$ definition is,

$$f(t) \otimes_a g(t) = F^{-1}\left(g_{a+1}(t_a)\left(f_{a+1}(t_a)\right)^H\right). \tag{3.19}$$

where F^{-1} is the fractional transform function with $a = -1$ (inverse Fourier transform), and H is the Hermitian transpose. $g_{a+1}(t_a)$ and $f_{a+1}(t_a)$ are the Fourier transform of FrFT of $g(t)$ and $f(t)$, respectively.

3.2.6.2 Optimum Filtering in FrFD

In many practical applications, the useful signals are overlapped by undesired (distortion) signals. This overlapping may be partially or completely in both the time and frequency domain. Transforming these signals into the FrFD with available prior

knowledge about the useful signal and the distortion signals may result in minimized or complete cancellation of the effect of undesired signals. Thus signals with significant overlap in both the time and frequency domain may have little or no overlap in the fractional Fourier domain (FrFD). As an illustration in Figure 3.4, depicts signals S_1 and S_2 that can be separated in the FrFT domain.

This is done by filtering the unwanted signal in the optimal FrFD before transforming the filtered signal back to the time domain.

The most commonly used observation model $\boldsymbol{Z}$ may be described by:

$$\boldsymbol{Z} = \boldsymbol{H}\,\boldsymbol{X} + \boldsymbol{Y}\,, \tag{3.20}$$

where $\boldsymbol{X}$ is the system useful signal, $\boldsymbol{Y}$ is the sum of all distortion signals, and $\boldsymbol{H}$ is the matrix characterizing the degradation process. The crosscorrelation matrix $\boldsymbol{R}_{x_a z_a}$ is the cross correlation between $\boldsymbol{x}$ and $\boldsymbol{z}$ (column vector in $\boldsymbol{X}$ and $\boldsymbol{Z}$, respectively) in the FrFT domain of order a. The auto correlation matrix $\boldsymbol{R}_{z_a z_a}$ is the autocorrelation for signal $\boldsymbol{z}$ in the FrFT domain of order a. These matrices may be calculated from the following equations [87]

$$\boldsymbol{R}_{x_a z_a} = \overline{\boldsymbol{F}}^{a}\boldsymbol{R}_{xx}\boldsymbol{H}^{H}\overline{\boldsymbol{F}}^{-a}\ , \text{ and} \tag{3.21}$$

$$\boldsymbol{R}_{z_a z_a} = \overline{\boldsymbol{F}}^{a}(\boldsymbol{H}\boldsymbol{R}_{xx}\boldsymbol{H}^{H} + \boldsymbol{R}_{yy})\overline{\boldsymbol{F}}^{-a}, \tag{3.22}$$

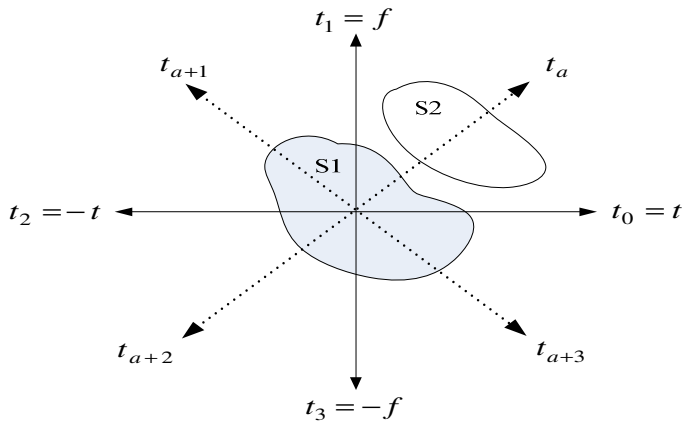

Figure 3.4 Signal separation in the a^{th} domain

where $\overline{\boldsymbol{F}}^{a}$ and $\overline{\boldsymbol{F}}^{-a}$ are discrete FrFT matrices of order a and $-a$, respectively, $\boldsymbol{R}_{xx}$ and $\boldsymbol{R}_{yy}$ are the covariance matrix for the signals $\boldsymbol{x}$ and $\boldsymbol{y}$, respectively.

The optimum filter $\boldsymbol{g}_{opt,i}$ (optimum order filter) to filter the $\boldsymbol{y}$ signal in the FrFT domain is given by:

$$\boldsymbol{g}_{opt,i} = \frac{\boldsymbol{R}_{x_a z_a}(i,i)}{\boldsymbol{R}_{z_a z_a}(i,i)} \quad i = 1,2,\ldots..,m \tag{3.23}$$

where m is the signal length.

The filtered signal $\hat{\boldsymbol{x}}$ in the time domain is calculated from [85, 94]

$$\hat{\boldsymbol{x}} = \overline{\boldsymbol{F}}^{-a} \boldsymbol{\Lambda}_g \overline{\boldsymbol{F}}^{a} \boldsymbol{z}, \tag{3.24}$$

where $\boldsymbol{\Lambda}_g$ is a diagonal matrix whose diagonal consists of the elements of the vector $g_{opt,i}$.

In this section, the discrete filtering in the optimal FrFD is formulated, and its solution based on the discrete fractional Fourier transform using the discrete FrFT matrices is introduced. Application of this filtering in the optimum FrFD will be shown in chapter 5.

3.2.7 Relation to Other Transforms

3.2.7.1 Linear Canonical Transform

Linear canonical transform (LCT) is a family of integral transforms that generalizes many classical transforms. The LCT has four parameters ($a, b, c,$ and d) characterized by a general rotation 2×2 matrix M and one constraint that the determine of M equal one [62, 63]. The LCT generalizes the Fourier, fractional Fourier, Laplace, Gauss–Weierstrass, Bargmann, and the Fresnel transforms as particular cases. The relationship between the LCT and the general formula for FT and FrFT will now be investigated.

The linear canonical transform $F^{M}[x(t)]$ of a function $x(t)$ is an integral transform with kernel $K^{M}(t^{M}, t)$ defined by [62, 63]

$$K^M(t^M,t)=\sqrt{\frac{\upsilon}{2\pi j}}\exp\frac{j}{2}\left(\mu(t^M)^2-2\mu t^M t+\omega t^2\right)=\sqrt{\frac{1}{2\pi jb}}\exp\frac{j}{2b}\left(a(t^M)^2-2t^M t+at^2\right), \tag{3.25}$$

where $\mathrm{M}=\begin{bmatrix} a & b \\ c & d \end{bmatrix}=\begin{bmatrix} \omega/\mu & 1/\mu \\ -\upsilon+\mu\omega/\upsilon & \mu/\upsilon \end{bmatrix}$, the parameters μ, υ, and ω are independent of t^M and t. For a rotation with angle θ, the four parameters in matrix M are chosen such as $a=d=\cos\theta$ and $b=-c=\sin\theta$ as

$$\mathrm{M}=\begin{bmatrix} \cos\theta & \sin\theta \\ -\sin\theta & \cos\theta \end{bmatrix}. \tag{3.26}$$

The FT is achieved by considering the transformation matrix M ($\theta=\pi/2$) and the transformation kernel $K^M(t^M,t)$ as

$$\mathrm{M}=\begin{bmatrix} 0 & 1 \\ -1 & 0 \end{bmatrix}, \tag{3.27}$$

hence $$K^M(t^M,t)=\sqrt{\frac{1}{2\pi}}\exp\frac{-jt^M t}{2}.$$

Similarly the inverse FT ($\theta=-\pi/2$) is calculated by

$$\mathrm{M}=\begin{bmatrix} 0 & -1 \\ 1 & 0 \end{bmatrix}, \tag{3.28}$$

thus $$K^M(t^M,t)=\sqrt{\frac{1}{2\pi}}\exp\frac{jt^M t}{2}.$$

The FrFT can be defined using LCT depending on two different decomposition of FrFT namely:

The 1st decomposition reflects the FrFT decomposition as chirp multiplication, chirp convolution, and another chirp multiplication. This can be seen from

$$\mathrm{M}=\begin{bmatrix} 1 & 0 \\ (d-1)/b & 1 \end{bmatrix}\begin{bmatrix} 1 & b \\ 0 & 1 \end{bmatrix}\begin{bmatrix} 1 & 0 \\ (a-1)/b & 1 \end{bmatrix}. \tag{3.29}$$

The 2nd decomposition of FrFT is expressed as chirp multiplication, FT, dilation, and another chirp multiplication. This decomposition is shown as

$$\mathrm{M}=\begin{bmatrix} 1 & 0 \\ d/b & 1 \end{bmatrix}\begin{bmatrix} b & 0 \\ 0 & 1/b \end{bmatrix}\begin{bmatrix} 0 & 1 \\ -1 & 0 \end{bmatrix}\begin{bmatrix} 1 & 0 \\ a/b & 1 \end{bmatrix}. \tag{3.30}$$

It is reported that more severe numerical rounding errors are experienced with the (3.30) for computing the FrFT compared to using (3.29) [63].

3.2.7.2 Wigner Distribution

The Wigner distribution $W_f(t,t_1)$ of a signal f can be defined in terms of the time-domain representation $f(t)$ of that signal as

$$W_f(t,t_1) = \int_{-\infty}^{\infty} f(t+t'/2)\, f^H(t-t'/2) \exp(-j2\pi t_1 t')\ dt'. \tag{3.31}$$

It is shown that the Wigner distribution of $f^a(t)$ is merely a rotation version of the Wigner distribution of $f(t)$ as

$$W_{f_a}(t,t_1) = W_f(t\cos\theta - t_1\sin\theta, t\sin\theta + t_1\cos\theta). \tag{3.32}$$

Thus the Wigner distribution of a signal and its FrFT are related by a rotation over an angle θ. In other words, rotation of Wigner distribution of a signal with angle θ as shown in Figure 3.5-A results in a Wigner distribution of this signal in the FrFD as illustrated Figure 3.5-B [88].

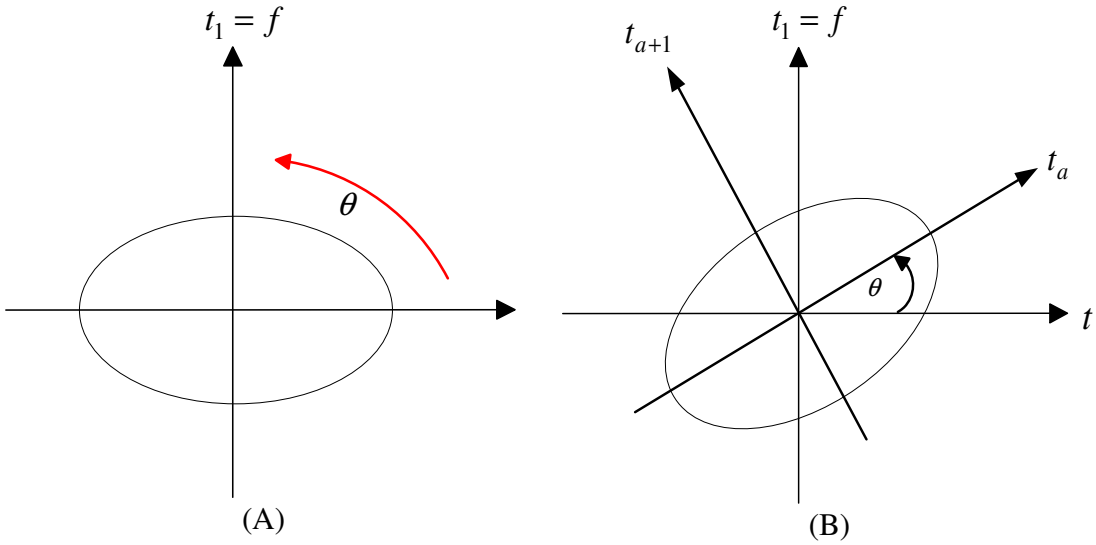

Figure 3.5 Wigner distribution of a signal in different domains

3.3 Empirical Mode Decomposition

EMD was developed for analyzing non-linear and non-stationary data [78]. EMD decomposition is based on the local characteristic time scale of data [95, 96]. EMD decomposes any data set into a finite and often small number of intrinsic mode functions (IMF) [97]. An IMF is defined as any function having the same numbers of zero crossings and extrema, and also having symmetric envelopes defined by the local maximal and minima, respectively [98]. The IMF also admits well behaved Hilbert transform verified to be highly orthogonal [99, 100]. With the Hilbert transform, the IMFs yield instantaneous frequencies as functions of time that give sharp identifications of imbedded structures [78]. The final presentation of the results is an energy-frequency-time distribution, designated as the Hilbert Spectrum.

Wavelet analysis and EMD are two decomposing algorithms [98]. EMD is used to decompose fast oscillations superimposed on slow oscillations while Wavelet analysis is used to decompose high frequency detail superimposed on low frequency components. Wavelet analysis splits the signal based on pre-determined spectral basis by the use of linear time-invariant filters and so prevents the possibility of adapting to local variations in the oscillations[98]. Thus, wavelets decomposition is conventionally achieved by repeated application of two filtering operations: firstly, pass the signal to high-pass filter extracts the detail. Secondly, the same filters applied to the approximation considered as a new full band after decimation by two.

In contrast to wavelets decomposing, which perform the analysis by projecting the signal under consideration onto a number of predefined basis vectors, EMD expresses the signal as an expansion of basis functions that are signal dependent and are estimated via an iterative procedure called sifting.

3.3.1 Classical and Bivariate EMD

The EMD iteratively decomposes a multi-component signal into a number of mono-component signals called IMFs. The iterative decomposition process is used for both the

classical and bivariate EMD. The classical EMD is used to decompose real signal and the bivariate EMD is used to decompose complex signal.

3.3.1.1 Classical EMD

EMD is a non-linear technique for analyzing and representing non-stationary signals. EMD is data-driven and decomposes a time domain signal $x[n]$ into a complete and finite set of adaptive basis functions which are defined as IMFs, $\boldsymbol{h}^{(i)}[n], 1 \le i \le L_{IMF}$. These IMFs are not predefined as in the case with the Fourier and the Wavelet transforms. The IMFs are oscillatory and have no DC component [98, 101, 102], so the signal $\boldsymbol{x}[n]$ can be represented as

$$\boldsymbol{x}[n] = \sum_{i=1}^{L_{IMF}} \boldsymbol{h}^{(i)}[n] + \boldsymbol{d}[n], \tag{3.33}$$

where $\boldsymbol{d}[n]$ is the residual.

When a signal $\boldsymbol{x}[n]$, that comprises a slowly oscillation relative to the sampling frequency superimposed on a highly oscillation signal relative to the sampling frequency (in our case additive interference noise signal), is applied to the EMD algorithm, the first IMFs tend to contain the highly oscillation signal (noise) and the remaining IMFs contain the useful signal (in our case radar chirp signal). In applications such as low frequency noise interference, the first IMFs in the EMD decomposition are the useful signal and the remainder contains the main noise components. Thus apriori knowledge of the noise characteristics in the EMD decomposed signal structure can be used to obtain the best performance.

Each IMF is estimated with the aid of an iterative process called sifting that is applied to the residual multi-component signal as shown in Figure 3.6

$$\boldsymbol{x}^{(i)}[n] = \begin{cases} \boldsymbol{x}[n] & i = 1 \\ \boldsymbol{x}[n] - \sum_{q=1}^{i-1} \boldsymbol{h}^{(q)}[n] & i \ge 2 \end{cases} \tag{3.34}$$

During the $(m+1)$th sifting iteration, the temporary IMF estimate $\boldsymbol{h}_m^{(i)}[n]$ is improved according to the following steps:

Table 3.1 Temporary IMF estimate $\boldsymbol{h}_m^{(i)}[n]$ improving

1	**While**	$\boldsymbol{h}_m^{(i)}[n]-\boldsymbol{m}_m[n]$ is not sufficiently close to zero
2		Identify all extrema (maxima and minima) of $\boldsymbol{h}_m^{(i)}[n]$.
3		Interpolate the extrema points of $\boldsymbol{h}_m^{(i)}[n]$ to make upper and lower envelope.
4		Compute the mean $\boldsymbol{m}_m[n]$ of the two envelopes (upper and lower).
5		Obtain the refined estimate $\boldsymbol{h}_{m+1}^{(i)}[n]$ of the IMF by subtracting the mean found in the previous step from the current IMF estimate $\boldsymbol{h}_m^{(i)}[n]-\boldsymbol{m}_m[n]$.
6	**End**	

To understand exactly how the classical EMD algorithm works, the signal $\boldsymbol{x}[n]$ consists of the linear chirp signal from Section 3.2.1 shown in Figure 3.7-A added to a sinusoidal signal $\sin(200\pi t)$ with sampling frequency 1000 Hz (shown in Figure 3.7-B) to form the combined signal shown in Figure 3.7-C .

Figure 3.8-A shows the interpolation for all maxima points and all the minima points of the temporarily IMF $\boldsymbol{h}_m^{(i)}[n]$ on two different curves. Figure 3.8-B shows a zoomed version of Figure 3.7-A.

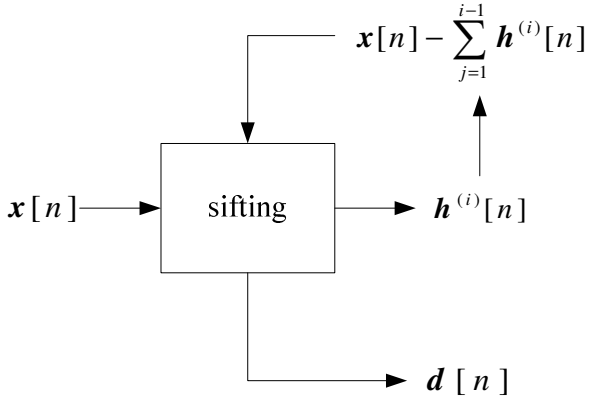

Figure 3.6 The EMD sifting process

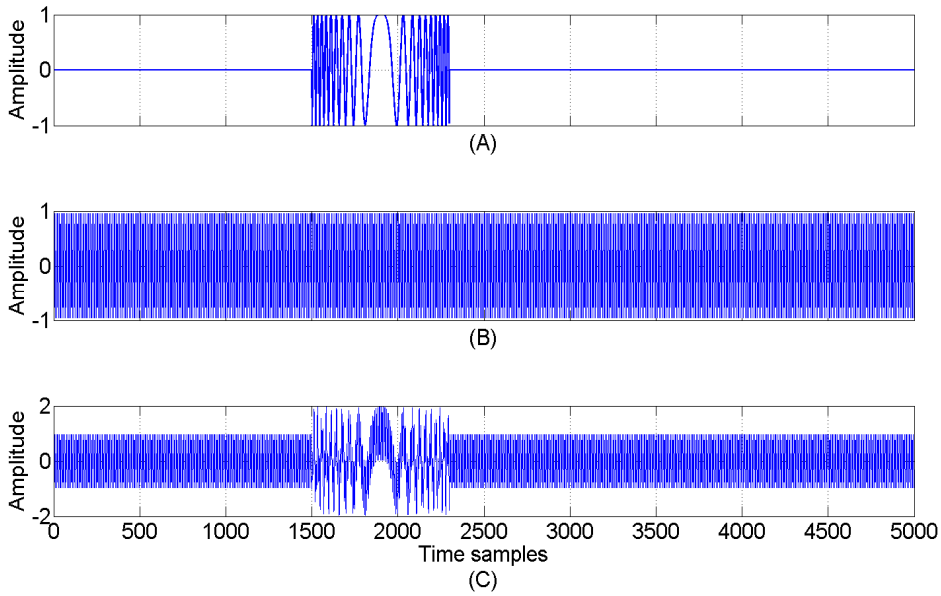

Figure 3.7 Combined chirp with sinusoidal signals

The mean curve $\boldsymbol{m}_m[n]$ is calculated as the mean of the interpolated curves and it is shown in Figure 3.8-C. The extracted mean $\boldsymbol{m}_m[n]$ is subtracted from the original $\boldsymbol{x}[n]$ and whole sifting iteration process continues for m times until the mean $\boldsymbol{m}_m[n]$ is reaching the stopping threshold criteria with nearly zero-mean. $\boldsymbol{m}_m[n]$ reaches the stoping criteria at the $m+1$ iteration process and the temporarily IMF $\boldsymbol{h}_m^{(i)}[n]$ is considered now as the 1st IMF $\boldsymbol{h}^1[n]$. $\boldsymbol{h}^1[n]$ is shown in Figure 3.9 and contains nearly all the sinusoidal signal $\sin(200\pi t)$ due to the fact that the first IMFs always contain the signal's high frequency components. The sifting process starts again with input signal $\boldsymbol{x}[n]-\boldsymbol{h}^1[n]$. All the previous processing work is repeated until the number of maxima points or minima points equal one (interpolation must be done at least between two points) and the last IMF (IMF 9) is achieved as seen in Figure 3.9. Note that the sum of the extracted IMFs from the 1st IMF 1 $\boldsymbol{h}^1[n]$ to the last IMF 9 $\boldsymbol{h}^9[n]$ results in the combined signal $\boldsymbol{x}[n]$.

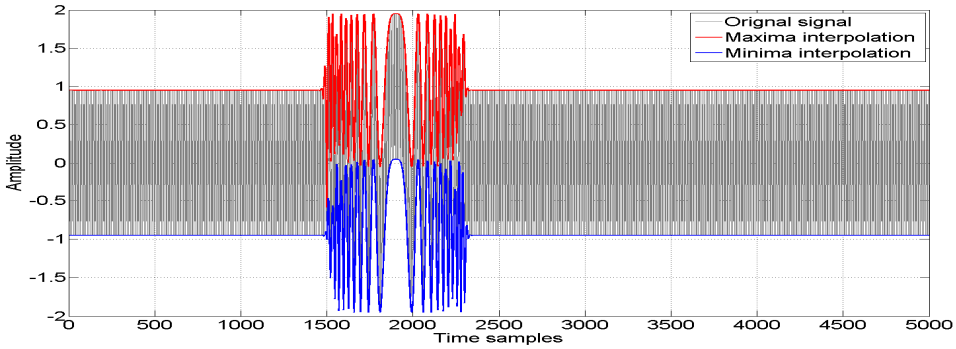

(A)

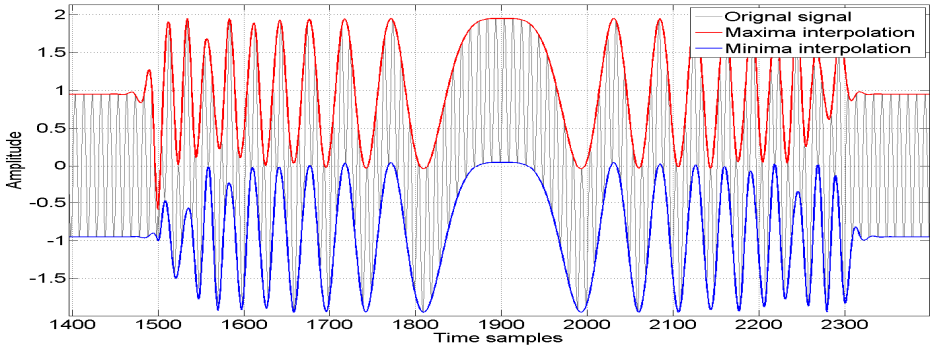

(B)

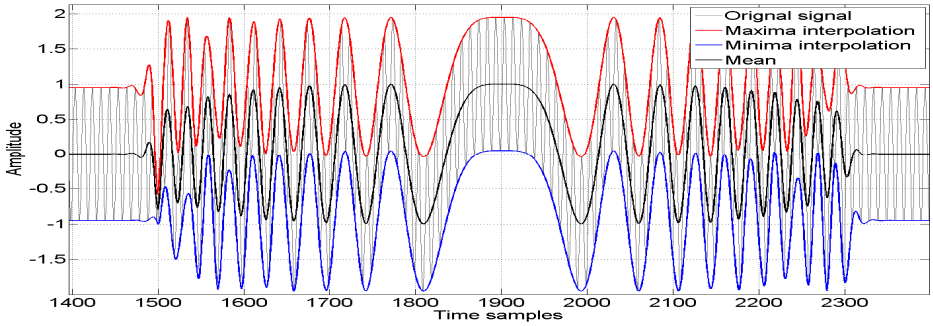

(C)

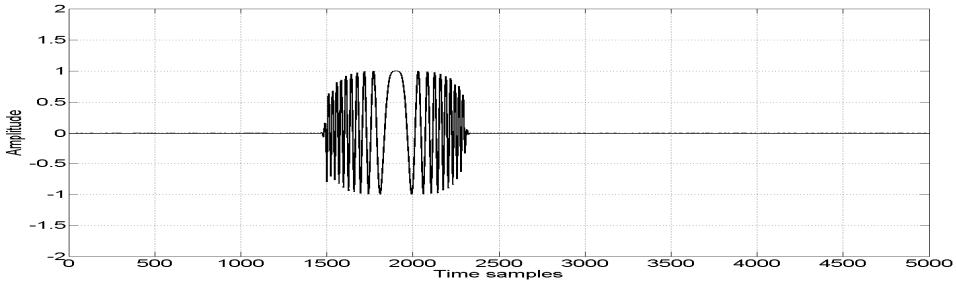

(D)

Figure 3.8 Classical EMD algorithm steps

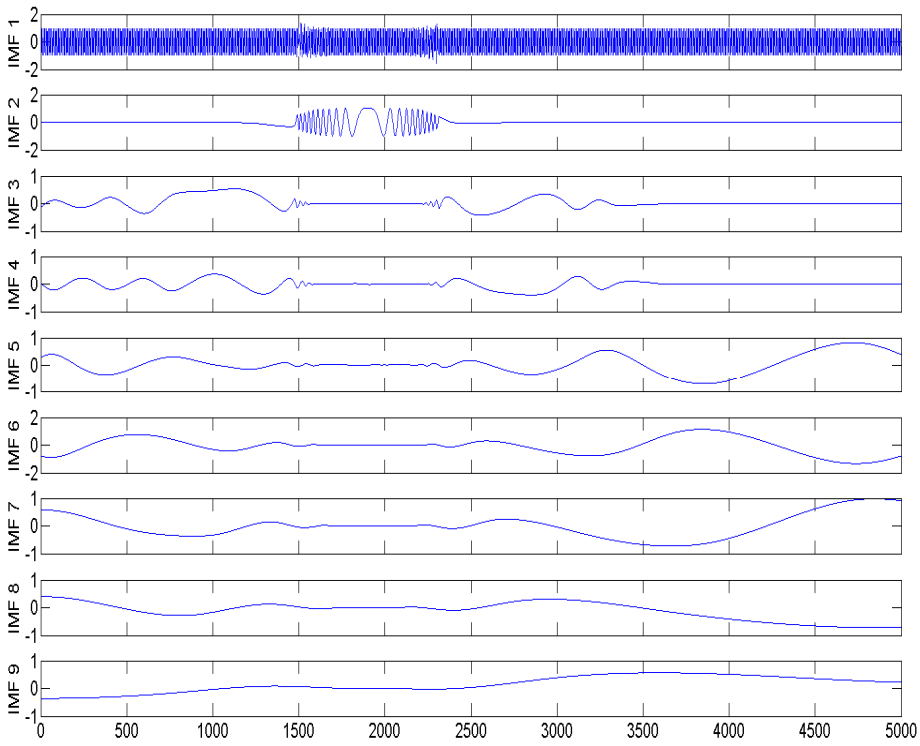

Figure 3.9 The IMFs of the combined signal

The classical EMD is not sufficient to deal with monopulse radar received complex chirp signal with additive interference noise. The bivariate EMD (complex EMD) is used to deal with complex data.

3.3.1.2 Bivariate EMD

The classical EMD described above can only be applied to real-valued time series. The bivariate EMD is used for complex valued time series [101, 102]. As with the classical EMD, the bivariate EMD is used to separate the more rapidly rotating components from slower ones. The procedure is to define the slowly rotating component as the mean of some envelope which is a three-dimensional tube that encloses the signal. The slowly rotating components of the signal at any point in time can then be defined as the centre of the enclosing tube.

Figure 3.10 presents how envelope curves are used to derive the mean which is the slowly rotating components of the signal. In Figure 3.10-A, four curves are considered to determine the tube periphery in four directions (top, bottom, right, and left) that encloses the complex signal then these four curves interpolate the maxima points of the signal in these directions. Vertical cross section in these curves results in four points is shown in shown in Figure 3.10-B and Figure 3.10-C. The barycentre or the intersection of two straight lines, one being halfway between the two horizontal tangents of these four points is one of the points pass through the centre of the enclosing tube as shown in Figure 3.10-B and Figure 3.10-C, respectively. Interpolate the entire points pass through this centre results in curve represents the slowly rotating components of the decomposed signal.

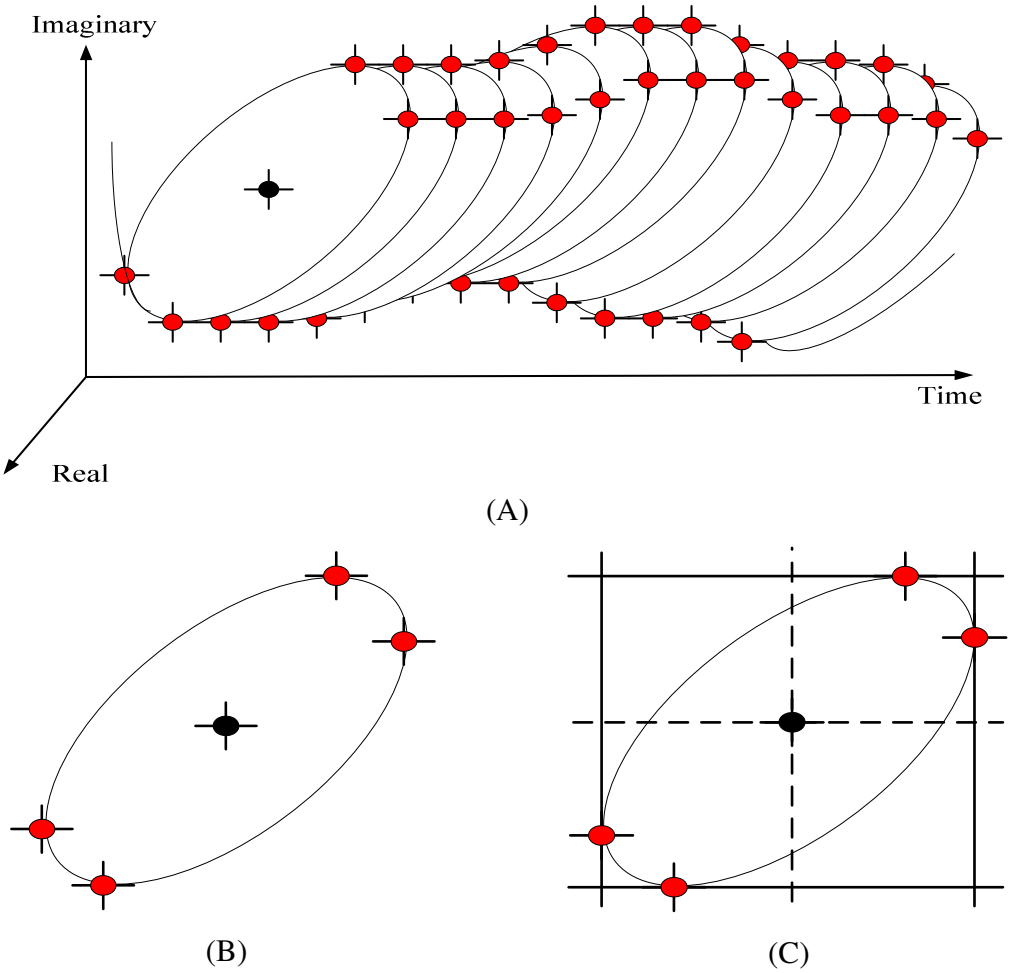

Figure 3.10 Different methods to determine the signal centre

The previous four directions can be generalized for different directions angles $\varphi_k = 2\pi k / K,\ 1 \le k \le K$ and are used in the following EMD complex algorithms [102].

Table 3.2 introduces bivariate EMD Algorithms which is used to decomposed complex signals.

Table 3.2 Bivariate EMD Algorithms [102]

First algorithm (Bi-EMD-1)	**Second algorithm (Bi-EMD-2)**
1 For $1 \le k \le K$ **do**	**1 For** $1 \le k \le K$ **do**
2 Project the complex-valued signal $\boldsymbol{x}[n]$ on direction $\varphi_k : \boldsymbol{\rho}_{\varphi_k}[n] = \Re(e^{-j\varphi_k}\boldsymbol{x}[n])$	**2** Project the complex-valued signal $\boldsymbol{x}[n]$ on direction $\varphi_k : \boldsymbol{\rho}_{\varphi_k}[n] = \Re(e^{-j\varphi_k}\boldsymbol{x}[n])$
3 Extract the locations $\{t_i^k\}$ of the maxima of $\boldsymbol{\rho}_{\varphi_k}[n]$, i refers to index	**3** Extract the maxima locations and its value $\boldsymbol{\rho}_{\varphi_k}[n] : \{t_i^k, \rho_i^k\}$, i refers to index
4 Interpolate the set $\{t_i^k, \boldsymbol{x}[t_i^k]\}$ to obtain the envelope curve in direction $\varphi_k : \boldsymbol{e}_{\varphi_k}[n]$	**4** Interpolate the set $\{t_i^k, e^{j\varphi_k}\rho_i^k\}$ to obtain the tangent curve $\varphi_k : \boldsymbol{e}'_{\varphi_k}[n]$
end	**end**
5 Compute the mean of all envelope curves: $\boldsymbol{m}[n] = \frac{1}{K}\sum_k \boldsymbol{e}_{\varphi_k}[n]$	**5** Compute the mean of all tangents: $\boldsymbol{m}[n] = \frac{2}{K}\sum_k \boldsymbol{e}'_{\varphi_k}[n]$
6 Subtract the mean to obtain $\boldsymbol{s}^{B_1}[x[n]] = \boldsymbol{x}[n] - \boldsymbol{m}[n]$	**6** Subtract the mean to obtain $\boldsymbol{s}^{B_2}[x[n]] = \boldsymbol{x}[n] - \boldsymbol{m}[n]$

In the special case for the 2nd algorithm (Bi-EMD-2) when K is an even number, the length of the "**For"** loop is reduced to $K/2$ and the mean is normalized by multiplying by 2 to be $\boldsymbol{m}[n] = \frac{4}{K}\sum_k e'_{\varphi_k}[n]$.

To understand exactly the two bivariate EMD algorithms, a complex signal is considered and is defined as:

$$\boldsymbol{x}[n] = \mathrm{a} + j\mathrm{b} + \exp(j\pi n f / F_s), \tag{3.35}$$

where $j = \sqrt{-1}$, a and b are constants, n represents the time samples, f is the signal frequency.

For the simplification purposes by $K = 4$, four angles directions φ_k ($\frac{\pi}{2}, \pi, \frac{3\pi}{2}$, and 2π) are considered. The complex signal $\boldsymbol{x}[n]$ in three dimensional plots (real, imaginary, and time samples) is shown in Figure 3.11-A as helix its centre at $\mathrm{a} + j\,\mathrm{b}$.

In the first algorithm Bi-EMD-1, for all k, the curves interpolate extrema $e_{\varphi_k}[n]$ in directions φ_k are all equal to: $x[t_i^1] = \mathrm{a} + j\,\mathrm{b} + j$, $x[t_i^2] = \mathrm{a} + j\,\mathrm{b} - 1$, $x[t_i^3] = \mathrm{a} + j\,\mathrm{b} - j$, and $x[t_i^4] = \mathrm{a} + j\,\mathrm{b} + 1$. Hence the center of these envelopes is $\mathrm{a} + j\,\mathrm{b}$ as shown in Figure 3.11-A and Figure 3.11-D.

For Bi-EMD-2, using the fact that the extrema of the projections $\boldsymbol{\rho}_{\varphi_k}[n]$ are the projections of these extrema $x[t_i^k]$, the tangent curves are calculated from the following table:

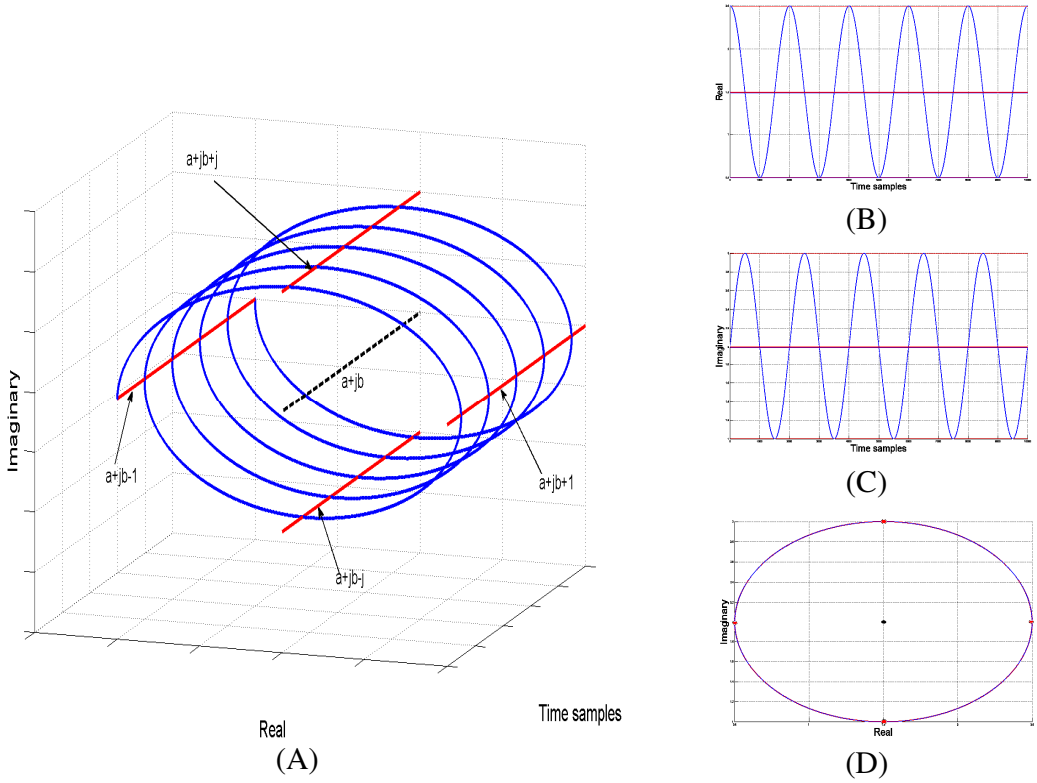

Figure 3.11 Bivariate EMD

Table 3.3 Bi-EMD-2 detailed calculation

$x[t_i^k]$	$e^{-j\phi}x[t_i^k]$	$\rho_i^k = \Re(e^{-j\phi}x[t_i^k])$	$e^{j\phi_k}\rho_i^k$
$x[t_i^1] = \mathrm{a} + j\,\mathrm{b} + j$	$\mathrm{a}\,j - \mathrm{b} - 1$	$-\mathrm{b} - 1$	$j\mathrm{b} + j$
$x[t_i^2] = \mathrm{a} + j\,\mathrm{b} - 1$	$-\mathrm{a} - j\,\mathrm{b} + 1$	$-\mathrm{a} + 1$	$\mathrm{a} - 1$
$x[t_i^3] = \mathrm{a} + j\,\mathrm{b} - j$	$-j\,\mathrm{a} + \mathrm{b} - 1$	$\mathrm{b} - 1$	$j\mathrm{b} - j$
$x[t_i^4] = \mathrm{a} + j\,\mathrm{b} + 1$	$\mathrm{a} + j\,\mathrm{b} + 1$	$\mathrm{a} + 1$	$\mathrm{a} + 1$

The mean of all tangent curves $m[n]$ is calculated as $0.5(2\mathrm{a} + 2\,jb) = \mathrm{a} + j\mathrm{b}$.

Applying both algorithms (Bi-EMD-1 and Bi-EMD-2) required angles directions φ_k more than four in the mentioned example to reduce the dependence of the final decomposition with respect to rotation of the spatial coordinates.

3.3.2 EMD Detrending and Thresholding (EMD-DT) Algorithm

The concept of detrending is to calculate an estimate of the IMF number at which all previous IMFs may be regarded as noise and the subsequent IMFs may be considered to contain the useful signal. The IMF detrending technique depends on assuming that the 1st IMF, $\boldsymbol{h}^{(1)}[n]$, captures mostly noise, the noise level $\hat{W}[1]$ is estimated in $x[n]$ by computing [96, 103]

$$\hat{W}[1] = \sum_{n=1}^{L} \left(\boldsymbol{h}^{(1)}[n]\right)^2 . \tag{3.36}$$

The model for noise only IMF energies can be approximated for white Gaussian noise dependence on the energy of the first IMF $\boldsymbol{h}^{(1)}[n]$ from [96, 103]

$$\hat{W}[i] = \frac{\hat{W}[1]}{0.719} \times 2.01^{(i)} . \tag{3.37}$$

The threshold level energies $T[i]$ are calculated using the approximated IMF energies in (3.37) from [96, 103]

$$\log_2\left(\log_2\left(\frac{T[i]}{\hat{W}[i]}\right)\right) = 0.46\,i - 1.92 . \tag{3.38}$$

Computing the IMFs energies by applying EMD algorithm on $\boldsymbol{x}[n]$ (noisy signal) from [96, 103]

$$W[i]=\sum_{n=1}^{L}\left(\boldsymbol{h}^{(i)}[n]\right)^2 . \tag{3.39}$$

Comparing IMFs energies $W[i]$ with threshold level energies $T[i]$ allows us to determine exactly when the signal energy level crosses the threshold level. Let this occur at $i=m$, the signal $\boldsymbol{x}[n]$ is denoised by reconstruction using only IMFs whose energy exceeds the threshold according to:

$$\tilde{\boldsymbol{x}}[n]=\sum_{i=m+1}^{L_{IMF}}\boldsymbol{h}^{(i)}[n]+\boldsymbol{d}[n]. \tag{3.40}$$

This concept of detrending and thresholding is used later in this thesis to filter the Gaussian noise signal in the proposed EMD filtering algorithm. For other types of noise for example short range correlation noise with Hurst exponent less than 0.5 or long range correlation noise with Hurst exponent greater than 0.5, the constants in the previous IMFs noise only model $\hat{W}[i]$ (3.37) and threshold level energies $T[i]$ (3.38) are changed according to the model defined in [96, 103] .

Figure 3.12 shows an example describing the detrending and the thresholding algorithm for a noisy chirp signal. Applying the EMD algorithm to this noisy signal results in 10

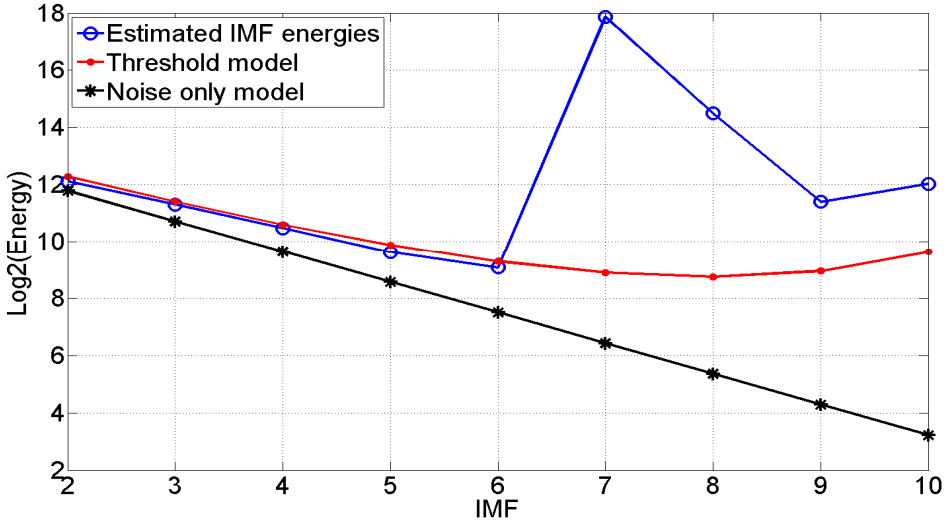

Figure 3.12 Detrending and the thresholding

IMFs (L_{IMF}). The 1st IMF is used to estimate energies for the remaining IMFs from (3.36) and (3.37) for the noise only model. The result is shown in black on Figure 3.12. The blue line represents the actual IMFs energies calculated from (3.38). The threshold model for each IMF from (3.37) is shown in red. It is clear that the actual IMFs energies are close to those estimated for noisy only model up to IMF 6 at which the threshold level is crossed. This means that these IMFs may be regarded as are essentially noise only. Thus the sum of IMFs from 7 to 10 represents the detrended and thresholded signal. For the noisy signal, the higher sampling frequency, the higher the number of samples, the greater the number of IMFs that are produced using EMD algorithm, the higher accuracy of detrending IMFs in the EMD-DT algorithm.

3.3.3 Invariant EMD Thresholding and Denoising Algorithms

Three EMD denoising algorithms that are inspired from iterative wavelet interval thresholding methods [97, 98] include:

- Interval thresholding EMD (EMD-IT)
- Iterative EMD Interval thresholding (EMD-IIT)
- Clear Iterative EMD Interval thresholding (EMD-CIIT)

3.3.3.1 Interval thresholding EMD (EMD-IT)

Direct thresholding (DT) is a wavelet-like thresholding method. DT depends on thresholding each IMF using the threshold $T[i]$ either for hard or soft thresholding. $T[i]$ described as [98]:

$$T[i] = C\sqrt{W[i]2\ln(L)}\,. \tag{3.41}$$

The thresholded IMF using this algorithm (both soft and hard) suffers from introducing discontinuities. DT makes segmentation for the thresholded IMF by putting zero for the values less than the threshold $T[i]$. EMD-IT overcomes this problem (discontinuities) of direct estimate $T[i]$ in each IMF by processing each IMF in intervals $\boldsymbol{z}_q^{(i)} = [z_q^{(i)}\ z_{q+1}^{(i)}]$ (isolated IMF samples). In each interval $\boldsymbol{z}_q^{(i)}$ it is impossible to decide for any one of them if they correspond to noise or to useful signal. However, it is possible to guess if

the interval is noise dominant or signal dominant based on the single extrema that correspond to this interval. If the signal is absent, the absolute value of this extrema will lie below the threshold. Alternatively in the presence of strong signals the extrema value can be expected to exceed the threshold.

3.3.3.2 Iterative EMD Interval thresholding (EMD-IIT)

EMD-IIT [97, 98] algorithm is inspired from iterative wavelet interval thresholding. EMD-IIT denoising depends on creating different noisy versions of the original signal and performing EMD-IT on each before averaging these denoised versions. The EMD-IIT method depends on the fact that most of the signal additive noise exists in the first IMF while the remaining IMFs (from 2nd IMF to the last IMF) contain the useful signal. EMD-IIT comprises: EMD expansion of the original noisy signal, randomly altering the sample positions of the first IMF to construct a different noisy version of the original first IMF. Adding the altered versions of the first IMF to the remaining IMFs creates different noisy versions of the original signal (altered first IMF + the remaining IMFs). The new version is expanded again using EMD before the new IMFs are denoised using EMD-IT. The previous steps are repeated for a number of iterations. The resultant denoised signal is the average of the resulting denoised signals from each iteration.

3.3.3.3 Clear Iterative EMD Interval thresholding (EMD-CIIT)

EMD-CIIT algorithm [97, 98] is similar to EMD-IIT algorithm except a thresholding operation of the first IMF is performed in an attempt to separate the noisy part of the first IMF from the non-noisy part. The noisy part is altered as described above. The altered noisy part of first IMF, the non-noisy part of first IMF and the remaining IMFs are combined to create a new version of the noisy signal. This is treated using EMD-IIT.

3.3.4 Best Selection of Sampling Frequency and Denoised Method

The higher the number of samples, the greater the number of IMFs that are produced. Using classical EMD algorithms the maximum number of these IMFs is $O(\log_2 L)$ [96, 103]. An increased number of decomposed IMFs, leads to higher accuracy of detrending in the EMD-DT algorithm. Furthermore the ability for the translation invariant EMD

algorithms to increase the output SNR after denoising depends on the number of samples and the shape of the desired signal [98]. As a result in our application it will be necessary to optimize both the EMD denoising method and the radar sampling frequency based on the monopulse received chirp signal (in the receiving window) with high interference jamming for different SNRs.

3.4 Conclusion

This chapter has introduced FrFT and EMD algorithms. Both algorithms are used in the remainder of this thesis to design and implement advanced monopulse radar systems that aim to overcome different types of interference in tracking radars and to enhance the tracking performance.

FrFT is the generalized formula for the Fourier transform that transforms a function into an intermediate domain between time and frequency. Signals with significant overlap in both the time and frequency domain may have little or no overlap in FrFD thus transforming signals into a particular FrFD may help to minimize or complete cancel the effect of undesired signals. The FrFT is able to process linear chirp signals better than the ordinary FT since there exists an order of transformation (optimum order) in which such signals become highly compact (spike) which can be used to apply many filtering ideas in the optimum FrFD.

EMD was developed for analyzing non-linear and non-stationary real and complex data thus it can be used with monopulse radar data. Many EMD filtering algorithms are used to filter the noisy data depends on the EMD decomposing such as EMD-DT, EMD-IT, EMD-IIT, and EMD-CIIT.

The next chapter will present the implementation of a radar matched filter using the FrFT to improve the matched filter output SNR and consequently improve the radar tracking performance.

4. FrFT Based Matched Filter

4.1 Introduction

Matched filters are commonly used in radar in which a known signal is transmitted, and the reflected signal is examined for common elements to the transmitted signal. Radar matched filters correlate a known signal (replica of the transmitted signal) with an unknown signal (received signal). This is conventionally achieved by convolving the incoming signal with a time-reversed version of the transmitted signal which can be efficiently carried using FT multiplication in the frequency domain before transforming back into the time domain. As mentioned previously in chapter 3, the FrFT is a mathematical generalization of the ordinary FT, the latter being a special case of the first when the fractional angle equals 90^{o} [62, 88]. The FrFT converts a chirp signal in the optimal FrFD to a narrow, highly compact, delta function. Computationally efficient matched filters, employed to enhance the signal to noise ratio, normally use FT multiplication. This chapter investigates the concept of the matched filter in the FrFD.

This chapter is organized as follows: Section 4.2 uses the principle of stationary phase (PSP) to derive the chirp signal in the Fourier and fractional Fourier domains, respectively. The matched filter in the Fourier domain and FrFD is presented in Section 4.3. A set of simulation results is presented in Section 4.4 for different scenarios. This section also includes a discussion on the chirp matched filtering in the FrFD, the signal parameter limitations, the improvement in SNR using matched filter in FrFT, and the usage of FrFT matched filter for multiple targets. Discussion underlining the results and the complexity comparison for matched filter in both the Fourier and fractional Fourier domains are presented in Section 4.5. Section 4.6 concludes the chapter.

4.2 PSP for Chirp signal in FT and FrFT

The principle of stationary phase (PSP) is an integration technique that can be applied to oscillatory integrals. PSP will be used in this section to estimate the mathematical modelling for a chirp signal in the frequency domain and FrFD using FT and FrFT, respectively.

4.2.1 Principle of Stationary Phase

PSP [104] can be applied to oscillatory integrals of the form:

$$S(k_y) = \int_{a_y}^{b_y} s(y)\, e^{j\varphi(y)}\, dy\,, \tag{4.1}$$

where $s(y)$ is a slowly varying function and $\varphi(y)$ changes by many cycles over the interval of integration. Under these conditions, contributions to the above integral over most of the y interval tend to cancel, and thus add little to the overall value of the integral [104]. An exception occurs for contributions at the stationary points of the phase $\varphi(y)$, defined as those values of y for which

$$\frac{d}{dy}\varphi(y) = 0\,, \tag{4.2}$$

The PSP states that the integral of (4.1) has its greatest contributions from those values of y which are stationary points of $\varphi(y)$ on the interval $[a_y, b_y]$. The following two steps are employed to evaluate the integral (4.1) involving:

1. Determine the location of the stationary point(s) of $\varphi(y)$.
2. Evaluate the integrand of (4.1) at the stationary point y^*.

If y^* is the only stationary point on $[a_y, b_y]$, then an approximation for the integral is

$$\int_{a_y}^{b_y} s(y)\, e^{j\varphi(y)}\, dy \approx \left(\frac{-\pi}{2\varphi''(y^*)} e^{-j\frac{\pi}{2}} \right)^{\frac{1}{2}} s(y^*)\, e^{j\varphi(y^*)}\,. \tag{4.3}$$

For the radar signal processing problem of interest here, the factor in brackets in (4.3), including a magnitude and phase term, is essentially constant ($\varphi''(y^*)$ is constant) and

without loss of generality will not be considered in the following analysis.

4.2.2 PSP for Chirp Fourier Transform

An illustrative application of the PSP involves the computation of the Fourier transform of a received chirp waveform using PSP. The received radar signal $s(t)$ formula (2.20) can be simplified to:

$$s(t)=\begin{cases} Ae^{-j2\pi(\phi_o)}\, e^{j\pi(\frac{\Delta f}{T})(t-T_{start}-\frac{T}{2})^2} & T_{start}<t<T_{start}+T, \\ 0 & elsewhere \end{cases} \tag{4.4}$$

The Fourier transform of $s(t)$ can be written as

$$S(f)=\int_{-\infty}^{\infty} s(t)e^{-j2\pi f t}\,dt\,. \tag{4.5}$$

Using the PSP, the phase of integrand is

$$\varphi(t,f)=-2\pi\phi_o+\pi\left(\frac{\Delta f}{T}\right)(t-\tau)^2-2\pi tf\,, \tag{4.6}$$

where $\tau=T_{start}+\dfrac{T}{2}$.

The stationary point is

$$t^*=f\frac{T}{\Delta f}+\tau\,. \tag{4.7}$$

Using (4.4) and (4.7) in (4.3) yields

$$S(f)=A\,e^{-j2\pi\phi_o}\;rect\left(\frac{t^*-\tau}{T}\right)e^{j\pi\left(\frac{\Delta f}{T}\right)(t^*)^2}\;e^{j\pi\left(\frac{-2\tau\Delta f}{T}-2f\right)t^*}\;e^{j\pi\left(\frac{\tau^2\Delta f}{T}\right)}. \tag{4.8}$$

Letting $B=A\,e^{-j2\pi\phi_o}$, then the formula of the received signal in frequency domain may be written as:

$$S(f)=Brect\left(\frac{f}{\Delta f}\right)e^{-j\pi\frac{T}{\Delta f}f^2}\;\;e^{-j2\pi\tau f}\,. \tag{4.9}$$

The $rect\,(.)$ function correctly indicates the nominal bandwidth of the chirp waveform and the exponential function correctly identifies the quadratic relationship across this bandwidth. The result in (4.9) is an approximation formula however it is a useful

engineering approximation especially in coherent radar problems emphasizing phase rather than magnitude.

4.2.3 PSP for Chirp Fractional Fourier Transform

A typical radar received signal $s(t)$ in the FrFD $S_\theta(u_a)$ may be calculated from (3.7) as

$$S_\theta(u_a) = \int_{-\infty}^{\infty} s(u)\, K_\theta(u_a, u)\, du\,, \tag{4.10}$$

where the FrFT kernel $K_\theta(u_a, u)$ is calculated from (3.6) [72]. Using PSP, the phase of integrand can be described as

$$\varphi(u_a, u) = 2\pi(\phi_o) + \pi\left(\frac{\Delta f}{T}\right)(u-\tau)^2 + \pi(u_a{}^2\mathrm{K})\cot\theta + \pi(u^2/\mathrm{K})\cot\theta - 2\pi\, u u_a \csc\theta\,. \tag{4.11}$$

The stationary point u^* is calculated as

$$u^* = \frac{u_a + \dfrac{\Delta f}{T}\tau\sin\theta}{\dfrac{\Delta f}{T}\sin\theta + \cos\theta/\mathrm{K}}\,, \tag{4.12}$$

and $S_\theta(u_a)$ in FrFD is written as

$$S_\theta(u_a) = A\ rect\left(\frac{u^*-\tau}{T}\right) e^{-j2\pi\phi_o}\, e^{j\pi(\frac{\Delta f}{T})(u^*-\tau)^2}\, K(u_a, u^*)\,. \tag{4.13}$$

Letting $B = A e^{-j2\pi\varphi_o}$

$$S_\theta(u_a) = B\, rect\left(\frac{u^*-\tau}{T}\right) e^{j\pi(\frac{\Delta f}{T}+\cot\theta/\mathrm{K})u^{*2}}\, e^{j\pi(\frac{-2\tau\Delta f}{T}-2u_a\csc\theta)u^*}\, e^{j\pi(\frac{\tau^2\Delta f}{T}+\cot\theta\, u_a{}^2\mathrm{K})}\,. \tag{4.14}$$

Letting $\mathrm{D} = \dfrac{\Delta f}{T}$, the chirp signal representation in the FrFD may be written as :

$$S_\theta(u_a) = B\, rect\left(\frac{u_a - \tau\cos\theta/\mathrm{K}}{\Delta f\sin\theta + T\cos\theta/\mathrm{K}}\right) e^{j\pi\left(\frac{(\mathrm{D}+\cot\theta/\mathrm{K})}{(\mathrm{D}\sin\theta+\cos\theta/\mathrm{K})^2} + \frac{-2\csc\theta}{\mathrm{D}\sin\theta+\cos\theta/\mathrm{K}} + \cot\theta\,\mathrm{K}\right)u_a{}^2} \tag{4.15}$$

$$\times\, e^{j\pi\left(\frac{2\mathrm{D}^2\tau\sin\theta + 2D\tau\cos\theta/\mathrm{K}}{(\mathrm{D}\sin\theta+\cos\theta/\mathrm{K})^2} + \frac{-4\mathrm{D}\tau}{\mathrm{D}\sin\theta+\cos\theta/\mathrm{K}}\right)u_a}\, e^{j\pi\left(\frac{(\mathrm{D}\tau\sin\theta)^2(\mathrm{D}+\cot\theta/\mathrm{K})}{(\mathrm{D}\sin\theta+\cos\theta/\mathrm{K})^2} + \frac{-2\mathrm{D}^2\tau^2\sin\theta}{\mathrm{D}\sin\theta+\cos\theta/\mathrm{K}} + \tau^2\mathrm{D}\right)}\,.$$

Equation (4.15) can be considered as the general transformation of the received chirp signal (4.4) to the FrFD with angle θ. For a special case $\theta = 90^o$ the signal representation in FrFT $S_\theta(t_a)$ in (4.15) can be shown to be identical to (4.9).

4.3 Matched Filter

The matched filter in both the Fourier and the optimum fractional Fourier domains are discussed in this section using the PSP implemented mathematical formula of the radar received signal in these domains.

4.3.1 Matched Filter in the Frequency Domain

The matched filter $M_F(f)$ in the frequency domain for $S(f)$ is designed as the complex conjugate of the exponential part of the signal $S(f)$ in (4.9)

$$M_F(f) = \left(e^{-j\pi\left(f^2 \frac{T}{\Delta f}\right)} \right)^H . \tag{4.16}$$

The radar return chirp signal after the matched filter is

$$S(f) = B\,rect\left(\frac{f}{\Delta f}\right) e^{-j2\pi\tau f} . \tag{4.17}$$

To transform $S(f)$ to the time domain an inverse Fourier transform formula is used as

$$s_m(t) = \int_{-\infty}^{\infty} S(f)\, e^{j2\pi f t}\, df . \tag{4.18}$$

Therefore $s(t)$ can be written as

$$s_m(t) = B \int_{-\infty}^{\infty} rect\left(\frac{f}{\Delta f}\right) e^{j2\pi f(t-\tau)}\, df \tag{4.19}$$

$$s_m(t) = B\, sinc\left(\Delta f\,(t-\tau)\right). \tag{4.20}$$

4.3.2 Matched Filter in FrFD

The shape of the signal in the FrFD in (4.15) is characterized by $rect\left(\frac{t_a - \tau\cos\theta/\mathrm{K}}{\Delta f \sin\theta + T\cos\theta/\mathrm{K}}\right)$ in which the position of the signal in the a^{th} fractional

Fourier order depends on $\tau \cos\theta / \mathrm{K}$. This dependence means the FrFT of the same chirp signal with the same chirp width changes position in the FrFD depending on two parameters τ and θ. So the chirp shape in the FrFT depends on the start time T_{start} because $\tau = T_{start} + \frac{T}{2}$, the chirp bandwidth Δf and the chirp duration T because $\theta = -\tan^{-1}\left(\frac{F_s{}^2 T}{\Delta f\, L}\right)$.

As a result the matched filter implementation in the FrFD requires knowledge about the start time T_{start} which is an unknown parameter in our case because it depends on the target range R_t from (2.21). All other parameters are known. In the next section three methods for estimated T_{start} will be presented.

The design of a radar matched filter in the optimum FrFD is a more complex problem than the normal FT matched filter due to the need for estimating T_{start}. In the frequency domain transformation of the FT matched filter (4.9), the signal is characterized by $rect\left(\frac{f}{\Delta f}\right)$ which depends only on the chirp bandwidth Δf that is known from the transmitted chirp waveform generator.

4.3.3 Methods to estimate T_{start}

Estimating the chirp start time T_{start}, which is the time of radar received chirp, depends on the target range. This estimation is essential in order to design the radar matched filter in the FrFD. Figure 4.1 shows a simulated noisy target chirp received signal. The time delay T_{start} needs to be estimated in order to design the matched filter in the FrFD through using one of the following three methods:

(i) FT matched filter.

(ii) Optimum FrFT of the received chirp.

(iii) Optimum FrFT of both the received and a reference signal.

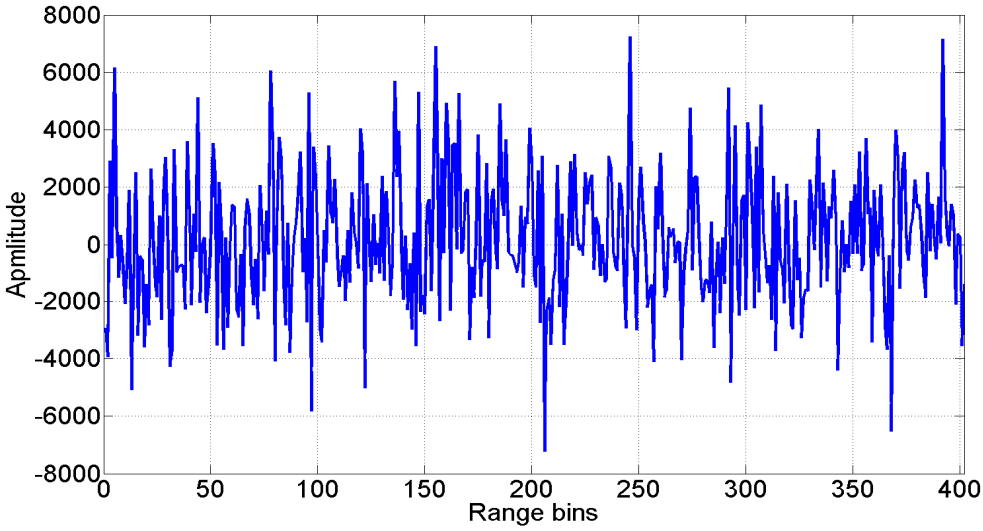

Figure 4.1 Noisy chirp received signal

4.3.3.1 Method 1: FT matched filter

Applying the matched filter formula (4.16) to the noisy chirp radar received signal (Figure 4.1), the signal output of the matched filter is seen in Figure 4.2. In Figure 4.2 a spike appears at the range bin 150 (related to the target range) which is the start bin of the bins occupied by the received chirp. This start bin R_{bin} (R_{bin} =150) is used to calculate the target range R_t which is used to calculate T_{start} from (2.21).

The target range R_t is calculated from the range bin by adding the range at bin 0, R_o, to the distance ΔR within the time window as:

$$R_t = R_o + \Delta R \tag{4.21}$$

and R_o is defined by

$$R_o = 0.5 c T_{w_1}, \tag{4.22}$$

where T_{w_1} is the start of time window and ΔR is calculated from:

$$\Delta R = 0.5(R_{bin} - 0.5) c / F_s . \tag{4.23}$$

The calculated target range R_t (from (4.21), (4.22), and (4.23)) is 156.975 km thus the estimated T_{start} from (2.21) is 0.001 sec.

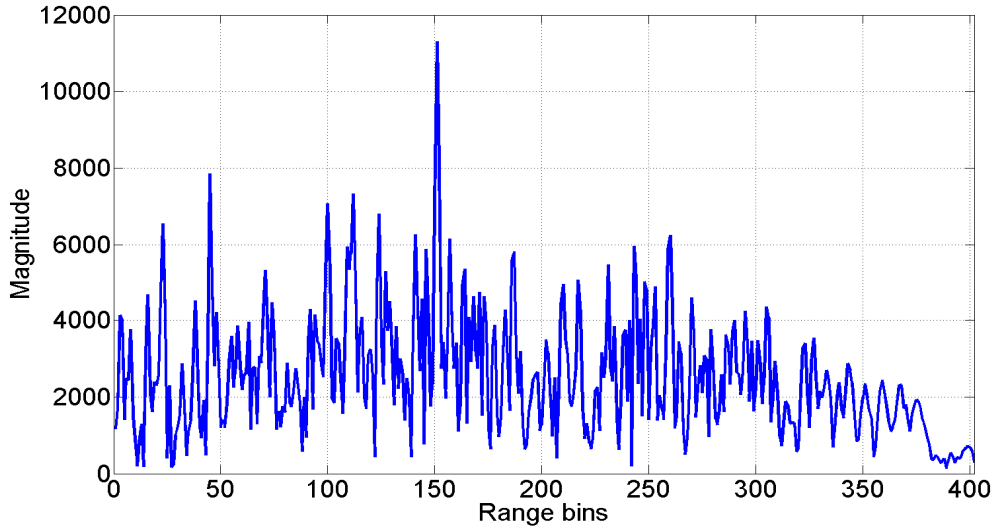

Figure 4.2 Estimate T_{start} using matched filter

4.3.3.2 Method 2: Optimum FrFT of the received chirp

Figure 4.3 shows the radar received signal transformed to the optimum FrFD using (3.1), (3.2) , and (3.14). A spike at sample 195 is seen in zoomed area of Figure 4.3. The chirp P_p sample number (195) is used to calculate t_{st} (the chirp start time sampling number) from (3.15) to be 150. The sample number t_{st} is used to calculate the target range R_t from (from (4.21), (4.22), and (4.23)) to calculate T_{start} from (2.21) to be 0.001 as in the previous method.

4.3.3.3 Method 3: Optimum FrFT for the received and a reference signal

In Figure 4.4, the radar received signal is transformed to the optimum FrFD as in the previous section, the target spike P_{pT} in the optimum FrFD is observed to be located at 195. A chirp signal with $T_{start} = 0$ in (4.4) is used as reference signal that is also transformed to the optimum FrFD, the location of the reference signal spike P_{pR} in the optimum FrFD is at sample 323. T_{start} is estimated from:

$$T_{start} = abs\left(\frac{P_{pT} - P_{pR}}{\cos\theta_{opt}}\right) / F_s + T_{w_1}. \tag{4.24}$$

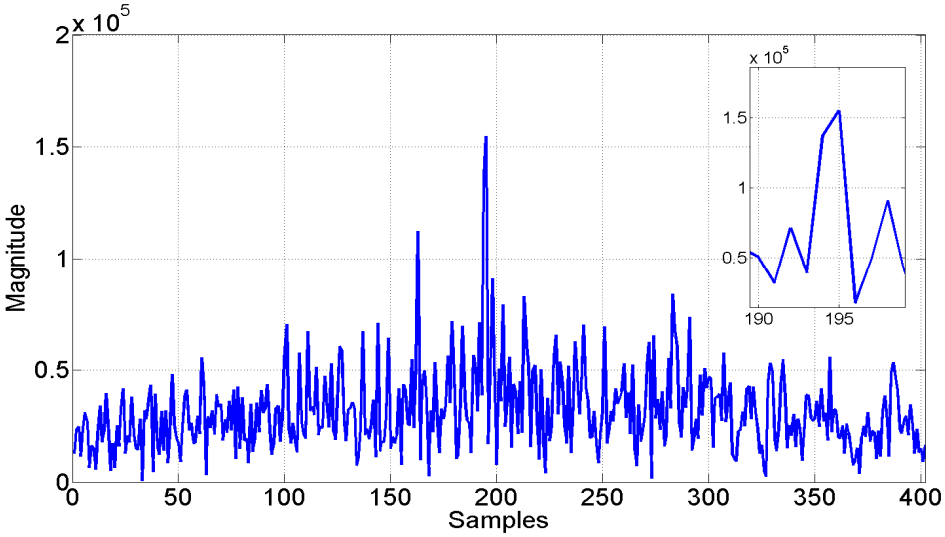

Figure 4.3 Estimate T_{start} using P_p

For the stating time window T_{w_1} is 8.97 micro sec, and calculated optimum angle θ_{opt} is 30.83^{o} in (4.24), the estimated T_{start} is .001.

4.3.4 Implementation of the Radar Matched Filter in FrFD

The Radar Matched Filter in FrFD is implemented as follows: the received signal, $s(t)$, is transformed to the optimal FrFD using *apriori* information from the transmitted chirp signal. This signal is convolved in the optimum FrFD with a replica signal. The mathematical formula of this replica signal in the time depends on the known or estimated value T_{start}.

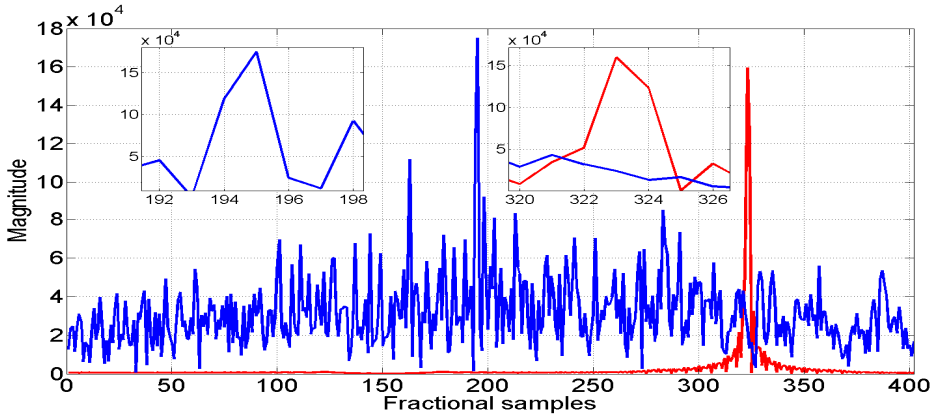

Figure 4.4 Estimate T_{start} using the difference in fractional bins

The convolution process is achieved by applying FT for both signals in the optimum FrFD, multiplying the two, then applying the inverse Fourier transform (IFT).
The required processing steps to perform the radar matched filter in FrFD are described in Table 4.1.

4.3.5 FrFT Matched Filter for Multiple Targets

The proposed optimum FrFD radar matched filter approach can be used for multiple targets detection in the received signal. In the case of multiple targets, as many echoes of the transmitted signal as the number of targets illuminated from the system are present in the received signal. A FrFT of the received signal will show the presence of multiple peaks, each one representing a target. In order to apply the fractional matched filter, an estimation of the unknown time delay must be performed for each target due to the shift variance property described in (3.16), meaning that a different replica must be used to extract each target. The procedure to extract the targets is described in Table 4.2

Table 4.1 Perform the Radar Matched Filter in FrFD algorithm

1	Optimum transformation order estimation: starting from the transmitting signal parameters (known signal parameters) the optimum fractional order is estimated using (3.14) to be used to transform the received signal to the optimum FrFD
2	FrFT of the received signal: the optimum FrFT of the received signal is performed to obtain a narrow peak detecting the presence of the received signal using (3.1) and (3.2)
3	T_{start} estimation: the chirp start time T_{start} is estimated by one of the previously described methods in subsection 4.3.3. This information is required in order to generate a suitable replica
4	Replica generation in the FrFD: using the known or estimated value of T_{start} a replica of the signal can be generated and its FrFT can be performed
5	Fourier Transform and matched filtering: to reduce the computational complexity of the matched filtering for the received signal and the replica optimum fractional version, both are transformed into their relative frequency domain and multiplied together.
6	Inverse Fourier Transform: IFT on the resulting signal after multiplying is performed to produce the matched signal output in the optimum FrFD. Steps 5 and 6 are done using FrFT cross correlation rule in (3.19).

Table 4.2 FrFT matched filter for multiple targets algorithm

1	**For** $1 \le k \le N_t$ **do** k is iteration index, N_t is the number of targets
2	Estimate the delay of the first echo with significant amplitude using of one of the previously methods described in subsection 4.3.3.
3	Generate the replica with the estimated delay and apply the fractional matched filter obtaining the target detection as mentioned in the algorithm in Table 4.1.
4	Subtract the k th echo from the received signal in order to perform the FrFD matched filter for the remaining targets. This subtraction is performed by subtracting the replica used for the FrFD matched filter from the received signal. The residual received signal contains another echo with a significant peak amplitude.
5	**End**
6	The output of each iteration can be added to the output from the previous iterations to obtain the final detections.

The procedure can be iterated a fixed number of times if the number of targets in the received signal is known or a stop rule for the iterations can be used, i.e. the algorithm can be stopped if the amplitude of the peak in the residual FrFT of the received signal is less than a certain threshold. A simulation of using FrFT matched filter for multiple targets will be provided in the next section (subsection 4.4.4).

4.4 Simulation Results

A linear chirp radar is simulated with a pulse width of 100 microseconds and a pulse repetition interval of 1.6 milliseconds with chirp bandwidth 500 KHz. The incoming baseband signals are sampled at 1 MHz. Also it is assumed that the radar operating range is 1:402 range bins. Two desired targets are known to exist at range bins equal to 50 and 250, respectively, with target signal to noise ratio (SNR) set to 60 dB and a Doppler frequency of 150 Hz. FrFT matched filter design dependence parameters that were described in subsection 4.3.2 are now investigated.

4.4.1 FrFT Radar Signal Dependence on T_{start}

The chirp signal for the target at range bin 50 is shown in Figure 4.5. It starts at range bin 50 with width 100 bins (equivalent to 100 microseconds). In a similar fashion the target at range bin 250 starts at range bin 250 with width 100 bins. Both target signals are filtered using a 200 kHz Gaussian band pass filter and the FFT of the output is computed. The magnitudes of the spectra are illustrated in Figure 4.6. As expected the spectra only depends on the chirp band width Δf . The FrFT of the target signals at range bins 50 and 250 are shown in Figure 4.7. The optimal order a_{opt} for the chirp signal calculated from (3.14) is 1.7061 and the absolute value of the FrFT of the signal is a spike at P_p sample number 293 (as seen in the zoomed figure) which could also be determined mathematically from (3.15). The target signal at range bin 250 appears at P_p sample number 114 in the optimum FrFD. From these results the FrFT dependence on start time T_{start} even when the chirp signal has the same chirp width is evident.

4.4.2 FrFT Radar Signal Dependence on Δf

Two different target chirp signals with bandwidths of 200 kHz and 500 kHz, respectively, are considered next. These radar chirp signals start at the same time and are completely overlapped in time as seen in Figure 4.8. The FFT of both signals is seen in Figure 4.9. As expected they overlap in the frequency domain. In Figure 4.10, the two spikes at P_p samples 2125 and 2285 (in the zoomed figures) demonstrate the dependence of the signal on the chirp band width Δf in the optimum FrFD. From Figure 4.10, it is observed that if the two chirp signals completely overlap in time and frequency they can be separated in the optimum FrFD.

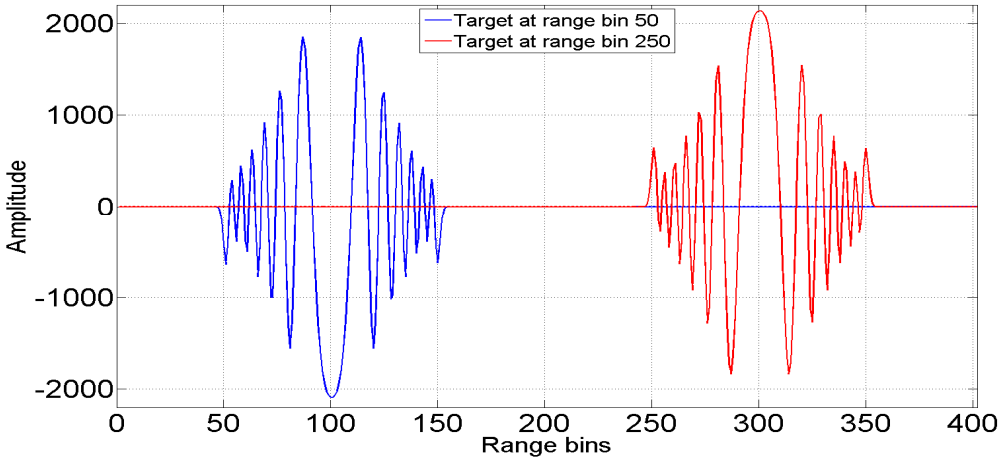

Figure 4.5 Chirp signals for different targets ranges

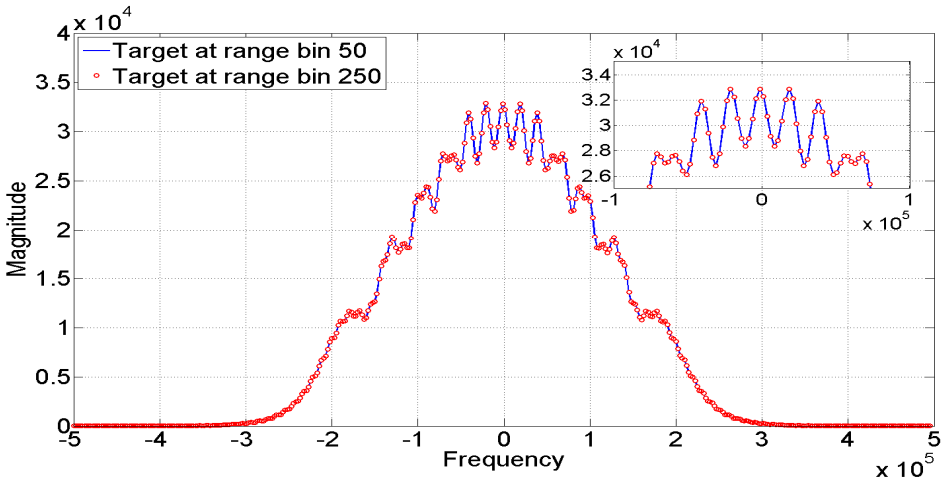

Figure 4.6 FFT for different targets ranges

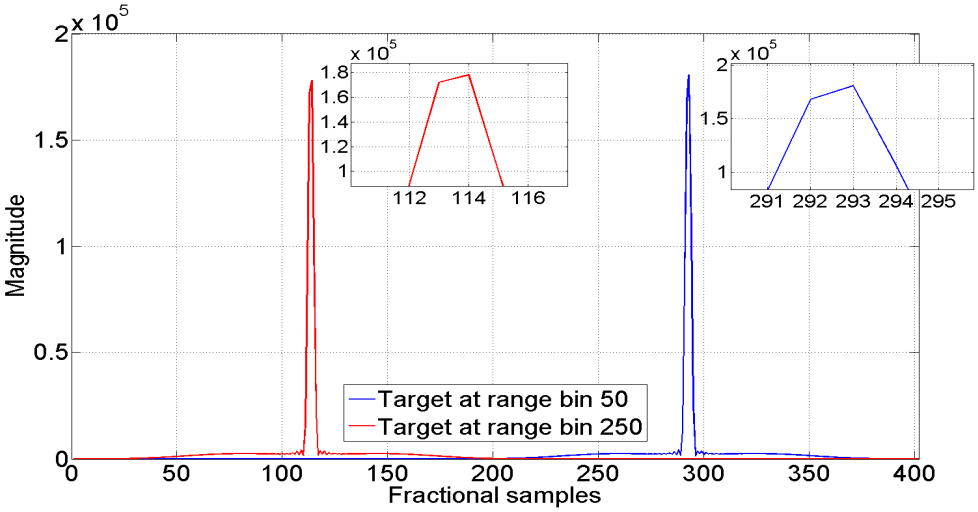

Figure 4.7 FrFT for different targets ranges

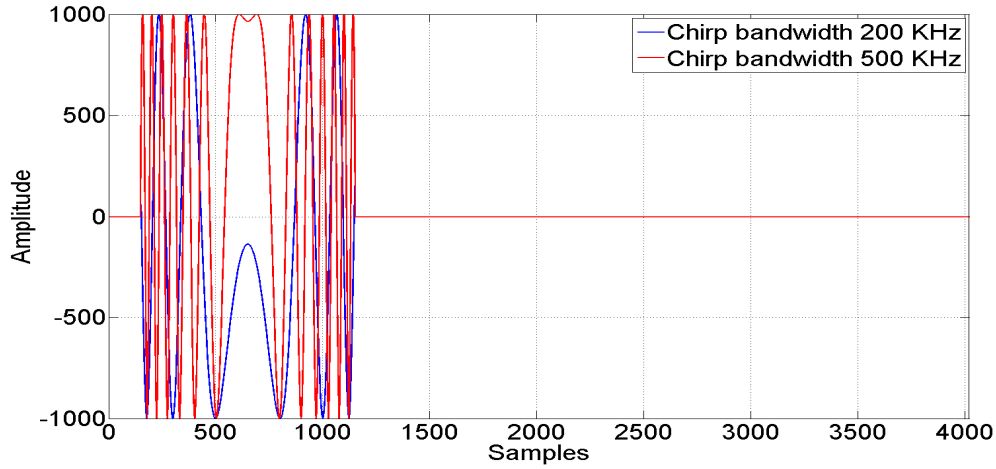

Figure 4.8 Chirp signals for different radars bandwidth

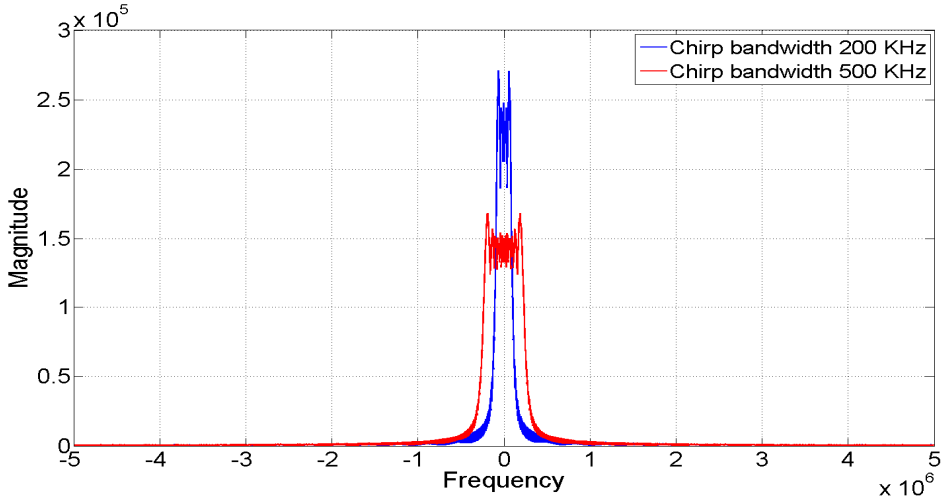

Figure 4.9 FFT of different radars bandwidth

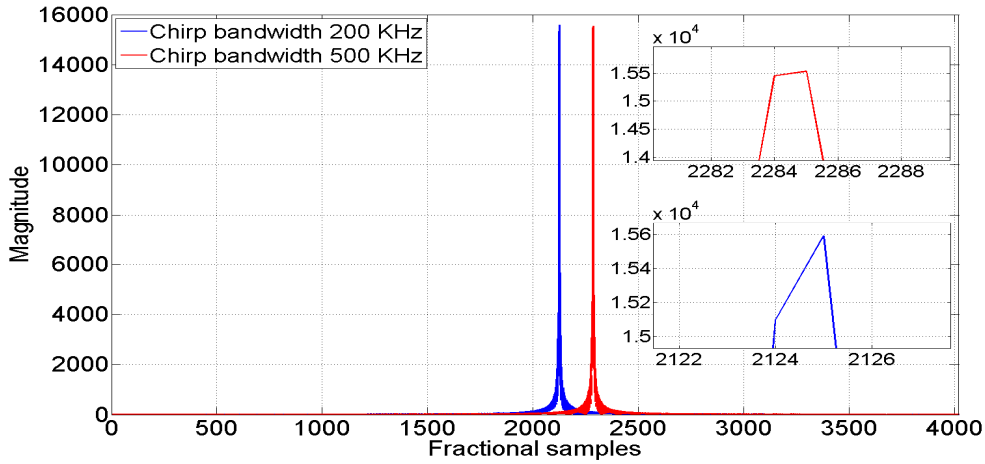

Figure 4.10 FrFT of different radars bandwidth

4.4.3 FrFT Radar Signal Dependence on Pulse Duration T

Consider a received radar signal that comprises two chirps with the same start time T_{start} but with different pulse width durations are seen in Figure 4.11. Both chirps start at range bin 150 with pulse width duration equal to 100 micro sec. and 120 micro sec. respectively. These two signals have the same chirp bandwidth so the FFT of both signals are identical as seen in Figure 4.12. The optimum FrFT of both signals is seen in Figure 4.13 in P_p sample 203 and 194 (shown in the zoomed figures) for the chirps with pulse width duration equal to 100 micro sec. and 120 micro sec., respectively. Thus the dependence of the matched filter design in FrFD on the chirp pulse with duration is observed.

4.4.4 FrFT Matched Filter for Multiple Targets

As described in subsection 4.3.5, the FrFD Matched filtering can be used for the case of multiple targets in the received signal. Figure 4.14 shows the case of two targets with a relative delay of 1 second. In this case the transmitted chirp has a bandwidth of 200 Hz with time duration of 1 second, the total range gate is of 2 seconds. The first target is placed after 0.5 seconds and the second after 1.5 seconds. In Figure 4.14-A and Figure 4.14-B the result of the first and the second iteration are shown while in Figure 4.14-C

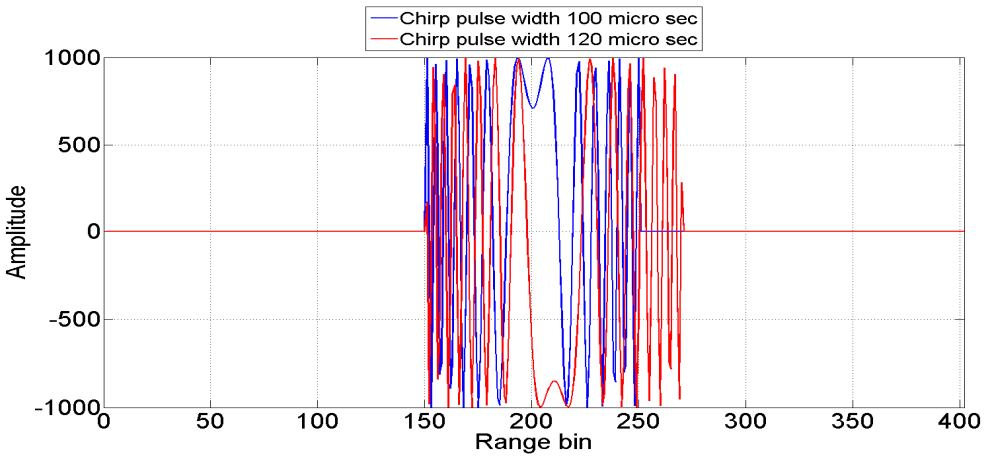

Figure 4.11 Chirp signals for different radars pulse duration

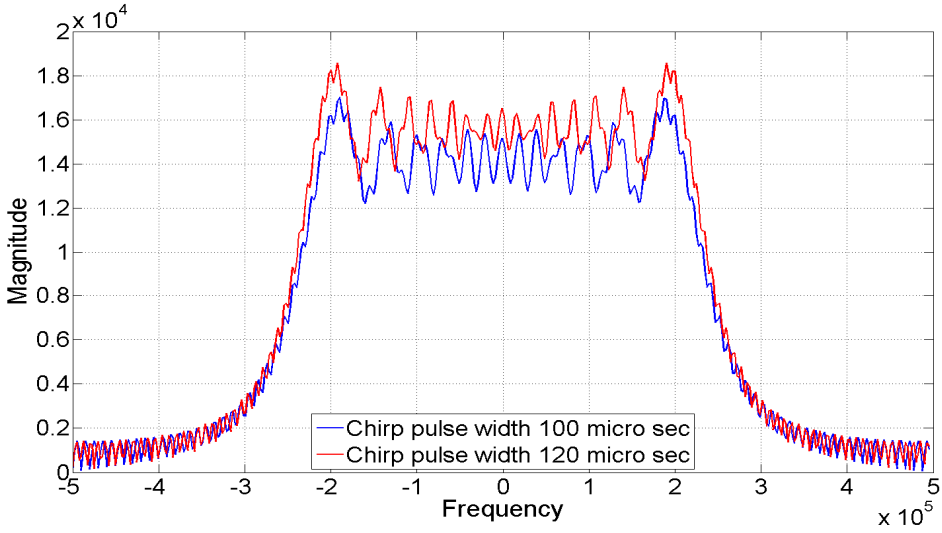

Figure 4.12 FFT for different radars pulse duration

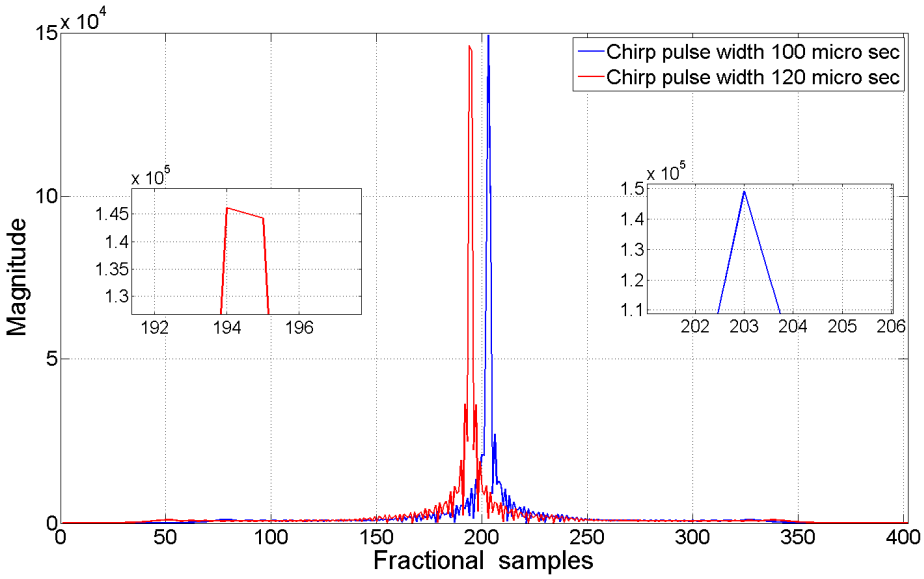

Figure 4.13 FrFT for different radars pulse duration

shows the final result. In the first iteration, Figure 4.14-A, the first target alone is detected while in the second iteration, Figure 4.14-B the second target is detected. The sum of the two iterations, Figure 4.14-C shows the detection of both the target.

The advantages provided by the use of the FrFT Matched Filtering compared to the Fourier approach are evident. In this case the -3 dB width of the main lobe is 17.3 times narrower than that obtained using the FT matched filter.

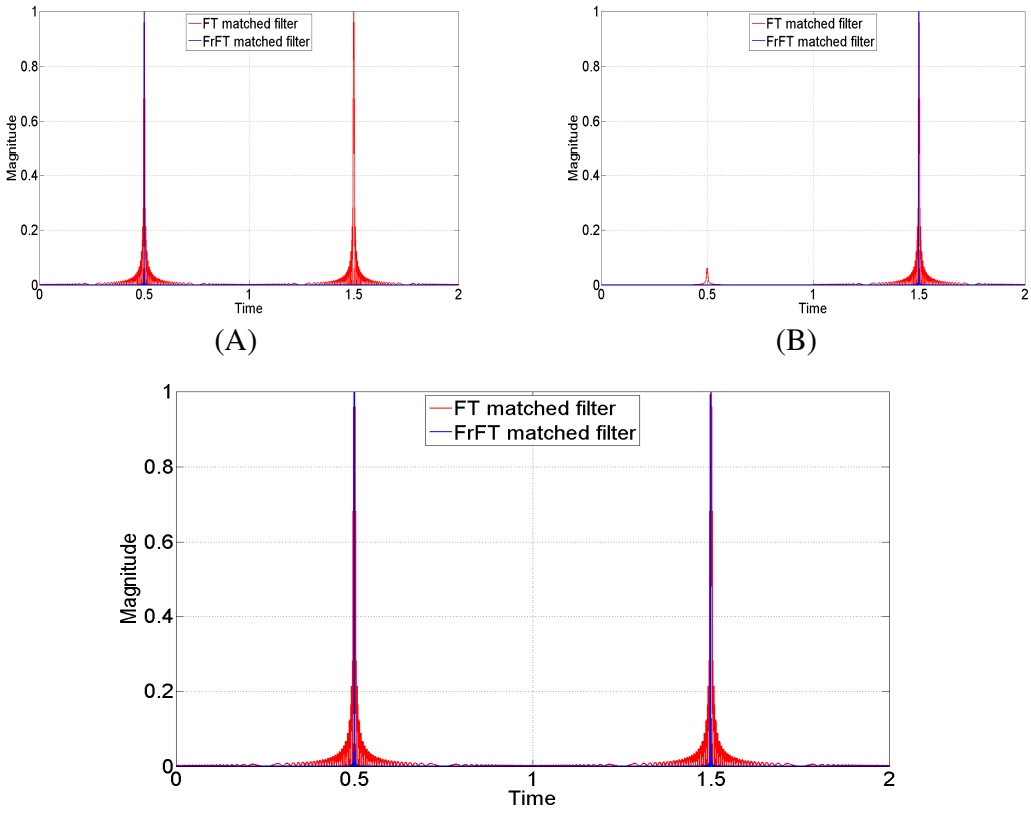

Figure 4.14 FT and FrFT Matched filters for multiple targets

(A) first target detection.
(B) secound target detection.
(C) resultant detection.

4.4.5 Performance Enhancement Using FrFT Matched Filter

It is clear from the mathematical model for the matched filter in FrFD (4.15) and the simulation results in subsections 4.4.1, 4.4.2and 4.4.3 that to obtain a matched filter in the FrFD the time delay of the received chirp is required. This time delay is estimated as described previously in subsection 4.3.3. The FT and FrFT matched filter outputs for two chirp signals with duration 1 sec. and chirp bandwidth 30 Hz starting at zero and 7.5 sec are shown in Figure 4.15 ($T_{start} = 0$) and Figure 4.16 (estimated T_{start}), respectively. In these figures an improvement of the chirp compressed width using the FrFT matched

filter rather than the FT matched filter for the applications with for $T_{start} = 0$ or estimated T_{start} is observed.

In Figure 4.15 and Figure 4.16, it is shown that the FrFT matched filter output is narrower than the FT matched filter output. At the 3 dB point the ratio between the widths of the FT matched filter output to that of the FrFT matched filter out is approximately 3.706. A significant reduction in side lobe using the FrFT matched filter is also observed in both figures. Figure 4.16 shows that the total side lobe power using the FrFT matched filter results to be 6.49 dBs less than that obtained using the FT matched filter.

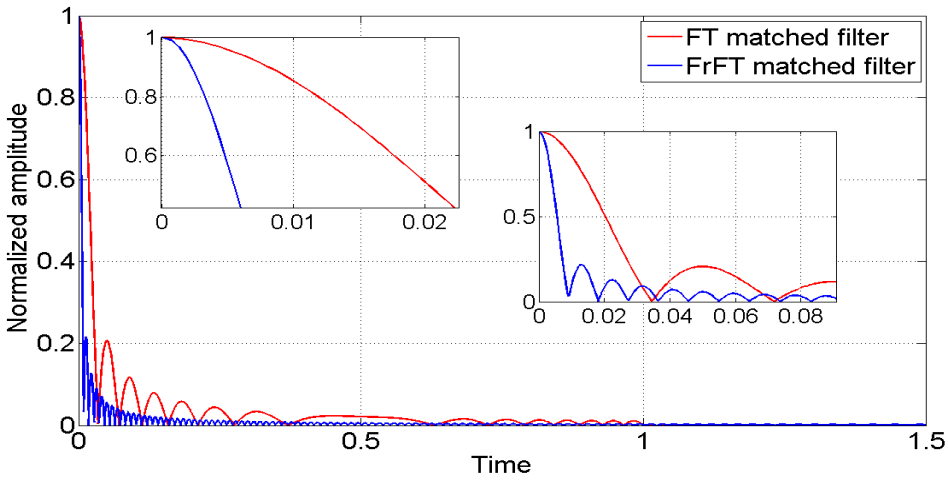

Figure 4.15 FT and FrFT Matched filters for $T_{start} = 0$

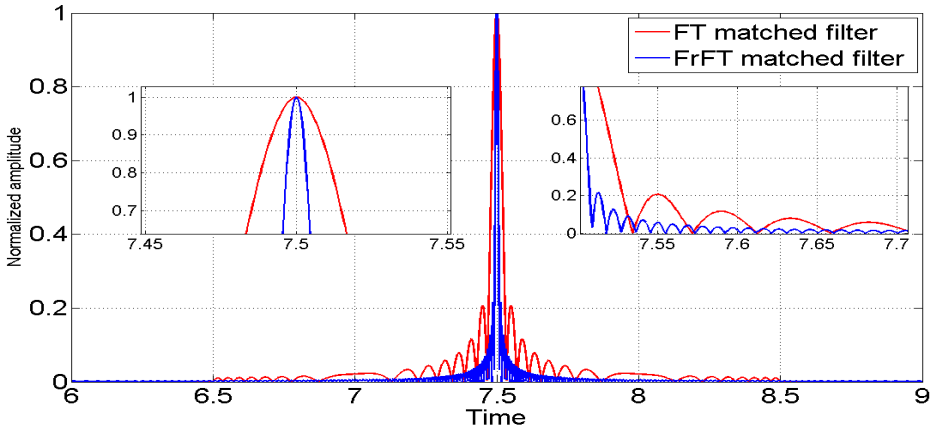

Figure 4.16 FT and FrFT Matched filters for known T_{start}

4.4.6 FrFT and FT Matched Filter Enhancement at Different SNRs

Simulation results for a chirp signal ($\Delta f = 30$ Hz, $T_{start} = 2$ sec with chirp duration 2.5 sec, $T = 5$ sec, and $F_s = 100$ Hz) in a noisy environment with different SNRs applied to both FT and FrFT matched filters is shown in Figure 4.17. This shows improvements in SNR output for the chirp signal for the two matched filters. The results in Figure 4.17 comprise an average over 500 independent noise generations. It shows an average improvement of approximately 3 dB by using FrFT matched filter compared to the FT matched filter for different input SNRs in range -15:20 dB. This gain in performance is accompanied with an increase in complexity as will be analysed in Section 4.5 for the implementation of matched filter in FrFD as well as the extra processing required for estimating the radar received parameters. For different simulation scenarios (different T_{start} , Δf , T , F_{start} , F_{stop} , and F_s), it is found that a SNR improvement is achieved using FrFT matched filter compared to using the FFT matched filter. The results are somewhat surprising, given that the matched filter is widely accepted as the optimum detector in the case of white noise and linear processing.

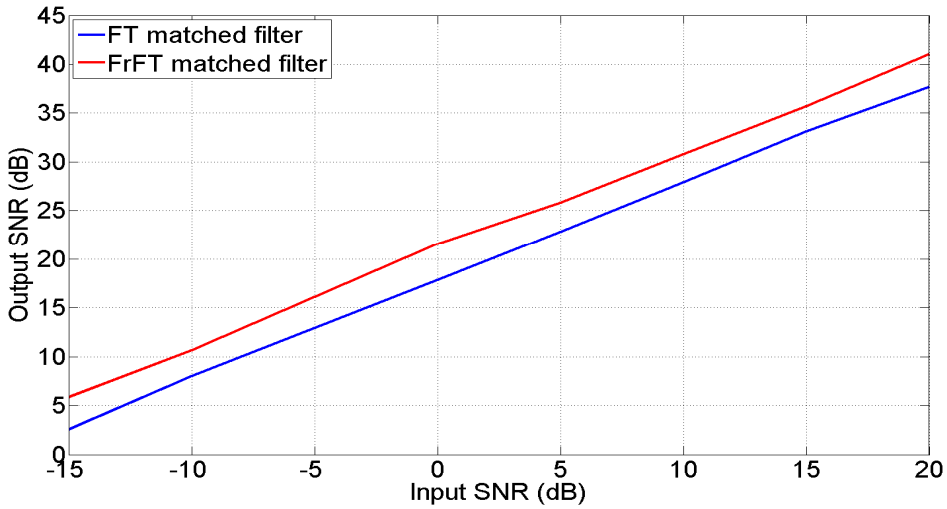

Figure 4.17 SNR signals output using FT and FrFT matched filtering

4.5 Discussion on Matched Filter Complexity using FT and FrFT

Performing the matched filtering in the FrFD is advantageous over the regular Fourier domain in that it achieves a narrower main lobe, reduces the side lobe levels, and enhances the SNR of the output. The chirp parameters (Δf , T , F_{start} , and F_{stop}), the chirp received time in the radar receiving window T_{start} , and the sampling Frequency F_s are the parameters that affect the extent of these enhancements. These improvements when using the proposed matched filter in the FrFD compared to the matched filter in the Fourier domain face an increased complexity requirement. To compare the matched filtering complexity in both the Fourier and the fractional Fourier domains, it is required to know the complexity of fast Fourier transform (FFT) algorithm and FrFT algorithm which will be described in the following:

- The complexity (complex multiplications) for an L -point FFT algorithm is $(L/2)\log_2 L$ (for L power of two).
- Various methods [63, 88, 105] are used to implement the FrFT algorithm. The complexity of these algorithms is approximated to $L\log_2 L$.

Table 4.3 shows a comparison of complexity between the matched filter implementation in both Fourier domain and FrFD. It shows that the matched filter in Fourier domain implemented by the FFT of the received radar signal multiplied by stored FFT replica of the received signal followed by inverse fast Fourier transform (IFFT) has a complexity approximated by $L\log_2 L$ (the same complexity as the FrFT). The implementation of the matched filter in FrFD starts with FrFT of the received radar signal multiplied by FrFT replica of the received signal (the mathematical formula of this replica depends on estimation of the start time T_{start}) followed by inverse fast Fourier transform. Depending on this implementation the total complexity for a matched filter in FrFD as seen in Table 4.3 is approximated by $2.5L\log_2 L$. Thus the complexity for implementing the matched filter in FrFD is approximately 2.5 times the complexity of the matched filter in Fourier domain.

Table 4.3 Complexity for matched filtering in the FT and fractional Fourier domains

filter / comparison	**Matched Filter (FT)**	**Matched Filter (FrFT)**
implement by	1 FFT 1 multiplications 1 IFFT	2 FrFT 1 multiplications 1 IFFT
complexity	$1\ L$ (required multiplications) $+(L/2)\log_2 L$ (1 FFT) $+(L/2)\log_2 L$ (1 IFFT) $\approx L\log_2 L$	$1\ L$ (required multiplications) $+2L\log_2 L$ (2 FrFT) $+(L/2)\log_2 L$ (1 IFFT) $\approx 2.5L\log_2 L$

4.6 Conclusion

In this chapter matched filters in the Fourier domain and the FrFD were investigated. The limitation of using matched filter in the optimum FrFT for a chirp signal was shown to be dependent on the chirp shape in this domain, on the chirp start time and chirp band width. The complexity of FrFT matched filter increases by approximately 2.5 times compared to the normal FT matched filter. In the special cases where specific parameters can be estimated then a significant enhancement results when using matched filter in the optimum FrFD compared to the conventional FT approach.

An average improvement of approximately 3 dB is gained by using FrFT matched filter compared to the FT matched filter for different input SNRs in range -15:20 dB in the considered case (the results are somewhat surprising, given that the matched filter is widely accepted as the optimum detector in the case of white noise and linear processing, and future investigation will aim to confirm the experimentally obtained results). At the 3 dB point the ratio between the widths of the FT matched filter output to that of the FrFT matched filter output is approximately 3.706. A significant reduction in side lobe using the FrFT matched filter is achieved in the cases studied.

FrFT based matched filtering can be used for target detection in chirp radars with the advantages of increasing the output SNR, reducing the side lobe power, that is applicable for multiple targets detection with the limitation of estimating the target received time (T_{start}) and increasing complexity compared to FT based matched filtering.

5. FrFT Based Monopulse Processor

5.1 Introduction

Monopulse radar processors are used to track a target that appears in the look direction beam width. The distortion produced due to many reasons such as manmade high power interference and additive unwanted targets that appear in the look direction beam width may lead to errors in the target tracking angles resulting in target mistracking.

A scenario where more than one target exists in the monopulse radar half power beam width is shown in Figure 5.1. The resultant distortion due to this interference will affect the induced target error voltage and consequently the radar tracking ability.

The distortion produced when manmade high power interference (jamming) is introduced to the radar processor through the radar antenna main lobe (main lobe interference) or antenna side lobe (side lobe interference) may affect the induced target error voltage and consequently the radar tracking ability. A scenario where manmade high power interference introduced to monopulse radar of main lobe jamming or side lobe jamming is shown in Figure 5.2. The resultant distortion due to this interference may lead to errors in the target tracking angles resulting in target mistracking.

This chapter consists of two main sections (5.2 and 5.3). It introduces new algorithms that aim to overcome the monopulse distortion problems mentioned previously. This chapter is organized as follows: Section 5.2 proposes a new structure of the FrFT based monopulse radar processor and derives the new algorithm, FrFT-ATF, for optimum FrFT to reduce the interference due to more than one target appear in the radar look direction. Later on Section 5.2, a set of simulation results is presented for single and multiple targets using the new monopulse processor.

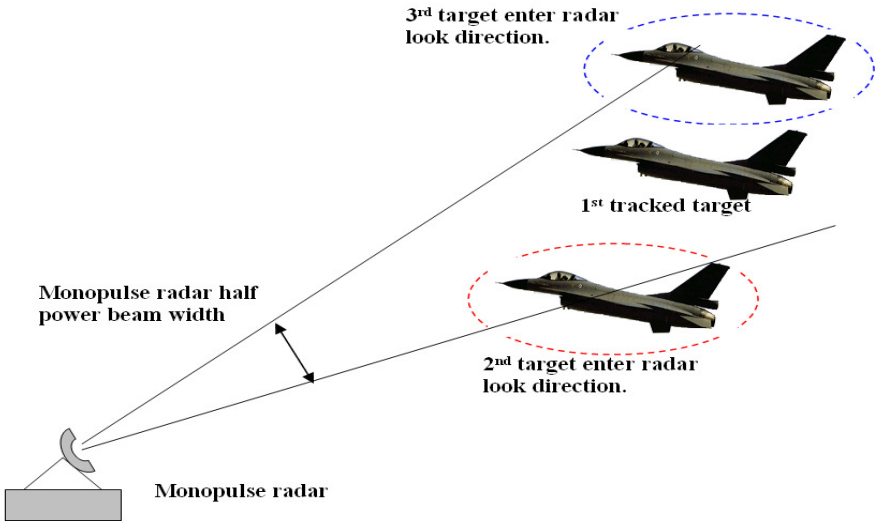

Figure 5.1 Three targets scenario for Monopulse radar

Section 5.3 proposes a new structure of the FrFT based monopulse radar processor, FrFT-NIF, to mitigate high power jamming signal introduced to the radar processor through the radar antenna. A set of simulation results using simulated and real data is presented for the new monopulse structure that shows the improved reduction in the interfered signal and improves the tracking performance for the FrFT based monopulse radar compared to the conventional monopulse radar are included. Section 5.4 concludes the chapter.

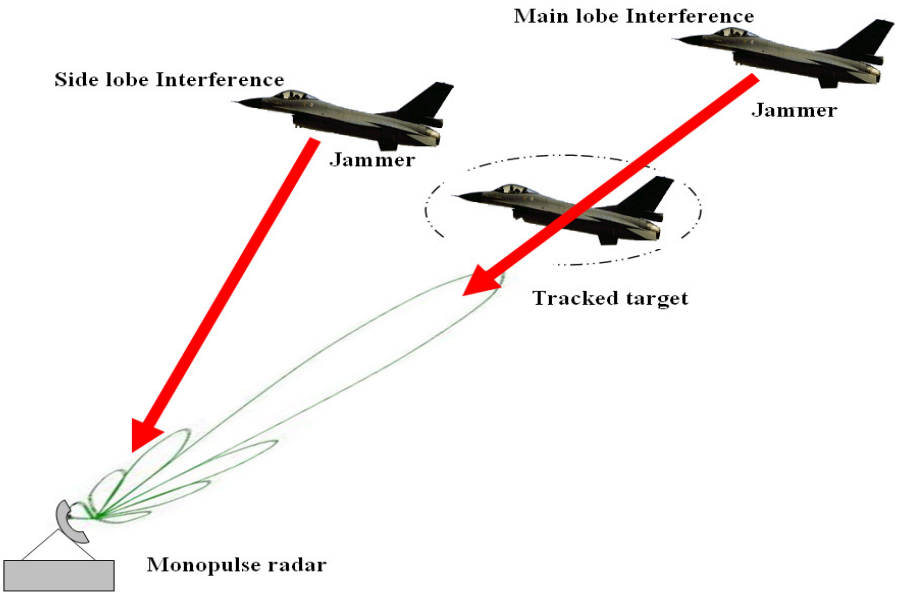

Figure 5.2 Interference scenarios for monopulse radar.

5.2 A New Structure of Monopulse Radar for Multi Targets in Look Direction

Various methods [36, 106, 107] for combating high noise power interference have been published.

Seliktar [37] suggested adding more constraints to the monopulse processor to cancel the distortion effect due to more targets appearing in the look direction using constraint matrix $\boldsymbol{C}$ and constraint vector $\boldsymbol{c}$ in (2.15). However this would require knowledge of the position of the additive targets. Our work proposes the use of an optimal FrFT filter to cancel the additional targets' signals that appear in the look direction half power beam width without adding any more constraints to the monopulse processor.

The proposed new structure of the monopulse radar is shown in Figure 5.3. In Figure 5.3 the optimum fractional filter obtains information about the shape of the chirp signal from the waveform generator and the updated target range from the range calculation. This information is used to determine the optimal FrFD.

The new optimum fractional filter (shown as red block in Figure 5.3) is illustrated in Figure 5.4. For N receiving channel in which the received signal from each of the N antenna elements fills L range gates, the total radar data size is therefore equal to

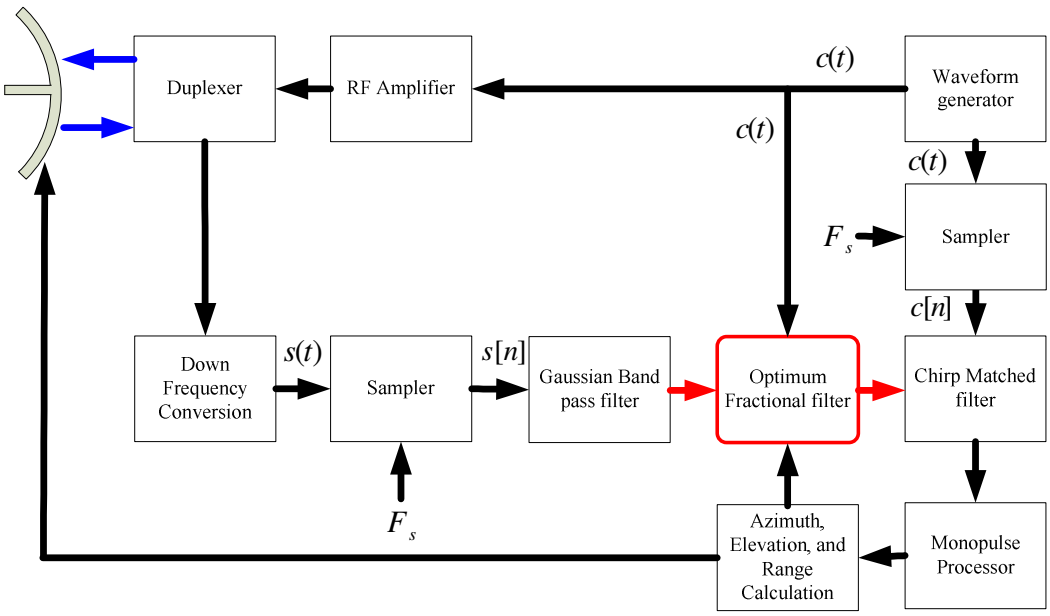

Figure 5.3 New structure of the proposed monopulse radar

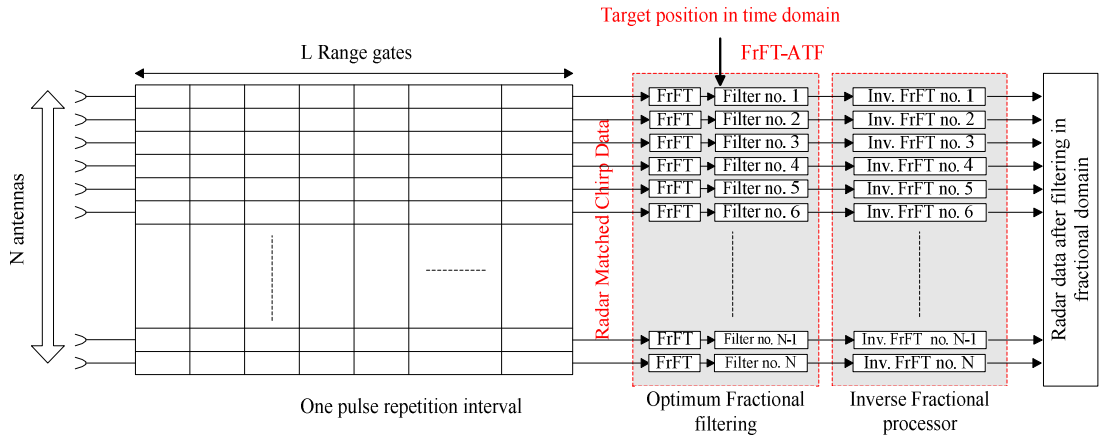

Figure 5.4 FrFT multi targets filtering radar data

$N \times L$ for each pulse return. The optimum FrFD is calculated for each receiving channel data with size $1 \times L$ to filter the signal in the FrFD. The resultant filtered data (useful signal) is converted back from the optimum FrFD using inverse FrFT to the time domain. The $1 \times L$ data output from N FrFT processors are applied to azimuth, elevation, and range calculator to determine the target information parameters.

5.2.1 The FrFT-ATF algorithm

The following steps in Table 5.1 describe the proposed FrFT filtering algorithm for additive targets (FrFT-ATF) that may be employed to cancel more than one target signal arriving in the look direction of the main beam while extracting the 1st target signal.

The mathematical description for the previous steps is now described in detail:

Applying the signal model of (3.20) to our radar system in which $\boldsymbol{H}$ is considered to be unity matrix (no system degradation)

$$\boldsymbol{Z} = \boldsymbol{S} + \boldsymbol{S}', \tag{5.1}$$

where the useful signal $\boldsymbol{S}$ is the received signal of tracked target signal and the distortion signal $\boldsymbol{S}'$ is the sum of the additional targets' signals (in the simulation, the 2nd target signal and the 3rd target signal).

The target received signal is a chirp signal given by (2.20). The optimum FrFT order a_{opt} for this chirp can be computed by applying (3.14) to the radar system as:

Table 5.1 FrFT for additive targets filtering (FrFT-ATF) algorithm

1	Calculate a_{opt} to determine the optimal FrFD for the 1st (tracked) target signal from the information supplied from the waveform generator.
2	Estimate the correlation matrix for the tracked target and the additive targets
3	Estimate the cross correlation matrix for the tracked and the other targets in the optimum FrFD and the auto correlation matrix of the additive targets in the optimum FrFD.
4	**For** $1 \le k \le N$ **do** (for each receiving channels), k is iteration index
5	Design the optimum filter in the FrFD
6	Extract the useful signal (the tracked target signal) by using the optimum FrFT matrix
7	Transform the filtered signal back to time domain using inverse FrFT with the known optimal order $-a_{opt}$.
8	**End**
9	Use the filtered $N \times L$ data to re-calculate the target information (target bin position, azimuth and elevation angles)

$$a_{opt} = -\frac{2}{\pi}\tan^{-1}\left(\frac{F_s^{\,2} \times T}{(F_{stop} - F_{start}) \times L}\right), \tag{5.2}$$

The required information to calculate correlation matrices is obtained from the fact that a previous knowledge of the target position is achieved (already tracked before the other targets enter the radar look direction) and from the sample signal of the waveform generator (parameters of the transmitted chirp signal). So $\boldsymbol{R}_{ss}$ apart from a scale factor A is computed as:

$$\boldsymbol{R}_{ss} = E(\boldsymbol{s}_e.\boldsymbol{s}_e^H), \tag{5.3}$$

where $\boldsymbol{s}_e$ is an estimate chirp signal of the first target at range R_t:

$$\boldsymbol{s_e} = \exp(-2j\pi \times \phi_s)\exp\left(j\pi\left(\frac{F_{stop} - F_{start}}{T} \right)\left(t_n - T_{start} - \frac{T}{2} \right)^2 \right), \tag{5.4}$$

where ϕ_s is a random phase shift similar to that used in (2.21) and T_{start} is calculated from (2.21) for target at range R_t.

In the same fashion $\boldsymbol{R}_{s's'}$ is calculated from:

$$\boldsymbol{R}_{s's'} = E(\boldsymbol{s}'_{\boldsymbol{e}}.\boldsymbol{s}'^{H}_{\boldsymbol{e}}), \tag{5.5}$$

where $\boldsymbol{s}'_{\boldsymbol{e}}$ is an estimate chirp signal at the other targets range:

$$\boldsymbol{s}'_{\boldsymbol{e}} = \exp(-2j\pi \times \phi_{s'})\exp\left(j\pi\left(\frac{F_{stop} - F_{start}}{T} \right)\left(t_n - T_{start'} - \frac{T}{2} \right)^2 \right), \tag{5.6}$$

where $\phi_{s'}$ is a random phase shift similar to that used in (2.20) and $T_{start'}$ is calculated from (2.21) for target at range $R_t + \Delta R_t$ and ΔR_t is the maximum range difference between the 1st target and any of the additive targets that cannot be resolved by a range gate canceller. ΔR_t can also be considered as the number of range bin occupied by the 1st target. ΔR_t in (5.6) ensures that no need to acquire any information about the range of the additive targets.

The next step is to calculate the cross correlation matrix $\boldsymbol{R}_{s_a z_a}$ for the 1st and the sum of the targets and the auto correlation matrix $\boldsymbol{R}_{z_a z_a}$ of the targets sum in the calculated optimum FrFD by applying (3.20) and (3.21), respectively, as

$$\boldsymbol{R}_{s_a z_a} = \boldsymbol{F}^{a_{opt}} \boldsymbol{R}_{ss} \boldsymbol{I}^H \boldsymbol{F}^{-a_{opt}}, \text{ and} \tag{5.7}$$

$$\boldsymbol{R}_{z_a z_a} = \boldsymbol{F}^{a_{opt}} (\boldsymbol{I}\, \boldsymbol{R}_{ss}\, \boldsymbol{I}^H + \boldsymbol{R}_{s's'}) \boldsymbol{F}^{-a_{opt}}. \tag{5.8}$$

Then the optimum filter in the optimum FrFD $\boldsymbol{g}_{opt,q}$ is given by

$$\boldsymbol{g}_{opt,q} = \frac{\boldsymbol{R}_{s_a z_a}(q,q)}{\boldsymbol{R}_{z_a z_a}(q,q)} \quad q = 1,2,\ldots..,L \ . \tag{5.9}$$

The filtered signal $\hat{\boldsymbol{s}}$ in the time domain is calculated from (3.24). All the outputs signals from the N FrFT filters are supplied to the monopulse processor (the processors mathematical models were presented in Section 2.6) to calculate the target information.

Proposed FrFT filtering technique

To understand the proposed FrFT filtering algorithm (FrFT-ATF) applied to cancel additive targets in the radar data, the following target parameters are considered, the tracked target's SNR equals 50 dB, the additive target's SNR equals 47 dB, at an angle that varies randomly near to the tracked target (the radar is locked on the 1st target before the additive targets enter the radar half power beam width) but still in the look direction beam width), and at range bin 153.

Figure 5.5-A shows the absolute value for the radar received signal in the 1st channel of the radar channels. The radar received signal is transformed to the optimum FrFD using the calculated optimum index a_{opt} equal to 1.7074 (Substituting the monopulse radar parameter values into (5.2)) and a spike for the tracked target appears at fractional sample 205 and for the additive appears at fractional sample 202 as seen in Figure 5.11-A. Applying FrFT filtering algorithm (FrFT-ATF), the additive target magnitude in the optimum FrFD is highly decrease in this domain as seen in Figure 5.5-B. this reduction in the additive target magnitude improves the tracking performance as seen later in the simulation section (section 5.2.2).

5.2.2 Simulation Results

In the simulations the radar comprises the same radar parameters considered previously in subsection 2.9.1. The target is considered at range bin=150 at angle 32^o from the look direction with SNR set to 50 dB with Doppler frequency 150 Hz.

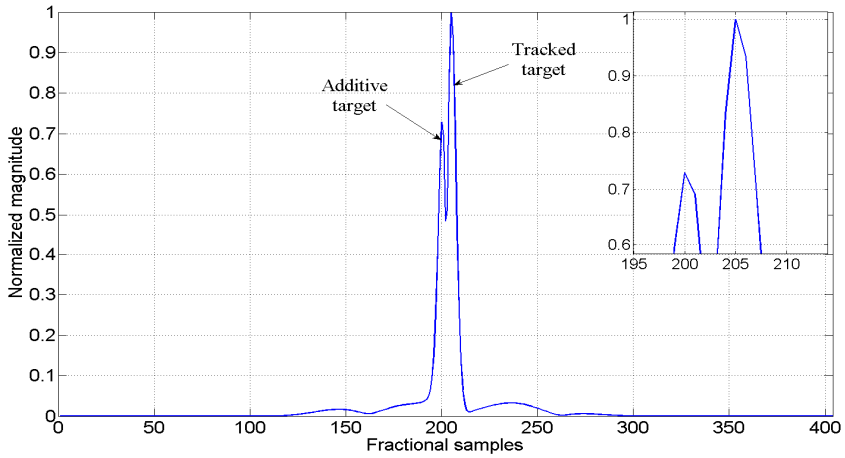

(A) Two targets in optimum FrFD (No filtering)

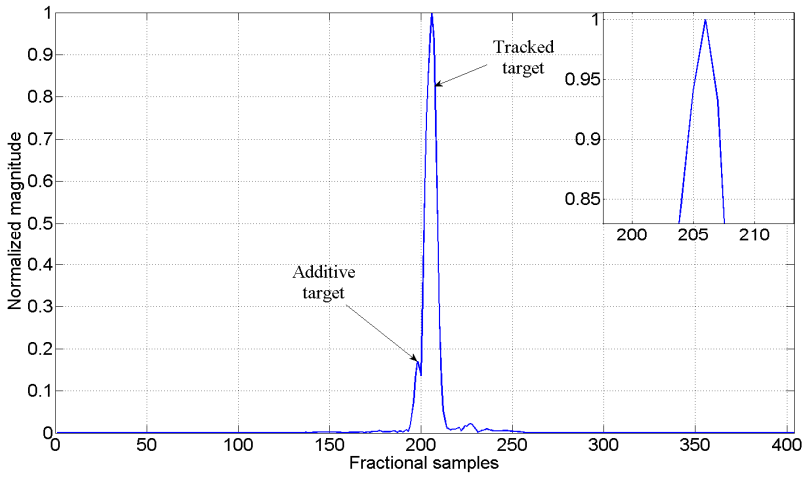

(B) Two targets in optimum FrFD (FrFT filtering)

Figure 5.5 FrFT filtering algorithm (FrFT-ATF).

5.2.2.1 Single Target

As seen in Figure 2.12-A that the sum pattern has maximum at the look direction angle 32^{o} and null at the same angle for the difference pattern in Figure 2.12-B. A well sloped curved for monopulse error voltage is calculated from (2.10) and is shown in Figure 2.12-D. It determines the target position by mapping this voltage onto the MRC in Figure 2.12-C to get $\hat{\phi}$. Any distortion to this curve will affect the target position

calculation. The processor output is determined from (2.9). From Figure 5.6-A, it is seen that there is only one target at the range bin 150 in the operating radar range bins.

Similary, the spatial processor pattern is calculated from (2.17), the processor output from (2.9), and the monopulse error voltage from (2.10). It is shown in Figure 2.13-A that the sum pattern has maximum at the look direction angle 32^o and null at the same angle for the difference pattern in Figure 2.13-B. It looks like the same pattern shape of the conventional processor because there is no signal interference due which the sum and difference patterns change their shape to try to cancel the effect of this interference. Again a well sloped curved for monopulse error voltage is obtained. From Figure 5.6-B, it is seen that there is only one target at the range bin 150 in the operating radar range bins.

5.2.2.2 Multiple Targets

In the simulation for two targets the following target parameters are considered, the second target's SNR equals 53 dB (double the power of the 1st target), at an angle that varies randomly near to the 1st target (the radar is locked on the 1st target before the additive targets enter the radar half power beam width) but still in the look direction beam width), and at range bin 153. Note that this second target cannot be resolved because the 1st target occupied bins include 7 bins with the same Doppler frequency of the 1st target. For the three targets scenario, the third target SNR is considered to be equal 50 dB (equal power of 1st target), also at an angle that varies randomly near to

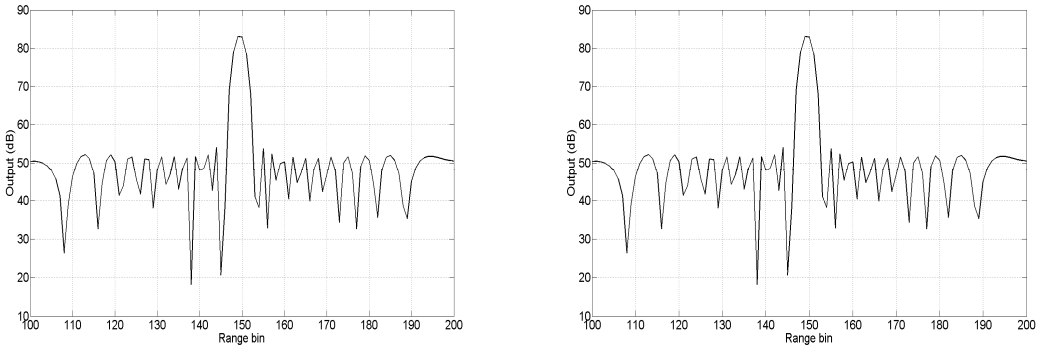

(A) Conventional processor (B) Spatial adaptive processor

Figure 5.6 Monopulse processor outputs.

the 1st target but still in the look direction beam width), and at range bin 147 (nearer than the 1st target to the tracking radar) with the same Doppler frequency as the 1st target.

Two Targets Scenario

The conventional and the spatial processor outputs using (2.9) are seen in Figure 5.7-A and Figure 5.8-A, respectively. It is clear that in these figures that the second target cannot be cancelled using range gate canceller (overlapped with the 1st target). The two target problem causes deviation in the monopulse error voltages from their original values to distorted curves as seen in Figure 5.7-B and Figure 5.8-B. This distortion in the error voltage will affect the tracking angle of the 1st target resulting in a probable mistracking outcome.

From Figure 5.7-D, the STDAE for the conventional processor is much higher at 2.9 for different target SNR (from 20-100 dB), so the system is completely distorted and the radar cannot track the 1st target. In the case of the spatial adaptive processor in Figure 5.8-D, it starts to achieve good tracking results from approximately 60 dB because of the adaptive characterization of the beam pattern that attempts to cancel the 2nd target signal. Despite the low STDAE values (average value 0.3) the processor still introduces considerable error in the 1st target angle calculation.

Three Targets Scenario

The conventional and the spatial processor outputs using (2.9) are seen in Figure 5.7-A and Figure 5.8-A, respectively. It can be seen in these figures that both the additive targets cannot be cancelled using range gate canceller (overlapped with the 1st target). There is now significant deviation in the monopulse error voltages from their original values to distorted curves as seen in Figure 5.7-B and Figure 5.8-B due to the third target. From Figure 5.7-D, the STDAE for the conventional processor is much higher at 2.9 for different target SNR, so the system is completely distorted and the radar cannot track the 1st target. In case of the spatial adaptive processor in Figure 5.8-D, it starts to achieve good tracking result from approximately 70 dB.

5.2.2.3 Monopulse Processors using Optimum FrFT Filter

Substituting the specific monopulse radar parameters in (5.2), the order of the optimal FrFD a_{opt} is computed as 1.7074. Following the steps described in subsection 5.2.1, the correlation matrix for the 1st target R_{xx} and the additive targets R_{yy} by considering $\Delta R_t =$ 7 range bin (more than 7 range bin there is no problem because the radar can cancel the additive targets using rage gate canceller) by using (5.3) and (5.5), respectively, are calculated. All the steps in subsection 5.2.1 are continued until the filtered data is produced.

Two Targets Scenario with FrFT

Applying the filtered data to the radar processors to calculate the processors outputs using (2.9), it is seen from Figure 5.7-C and Figure 5.8-C that only one strong target appears in the output and the 2nd target is significantly suppressed (more than 20 dB reduction). As seen in Figure 5.7-A and Figure 5.8-A, the resulting monopulse curve for the two targets scenario with FrFT are nearly identical to their original values (only one target). As a result the significance of the distortion due to the 2nd target in the monopulse look direction has been minimized. The resultant STDAE using (2.18) for different SNR (20:100 dB) for the conventional processor is particularly low (average value less than 0.1) as shown in Figure 5.7-D. In Figure 5.8-D the STDAE for the spatial processor in case of two targets using FrFT are particularly low (average value less than 0.1). The new system configuration enhances the system performance for the two target scenario at all SNR for the considered radar processors. If the scenario has only targets in the tracked target background then the calculated STDAE decreases to average 0.1 due to the highly signal suppression in this case. This implies that both processors are able to track the first target correctly and the introduced error due to the existence of the additive target is significantly reduced.

Three Targets Scenario with FrFT

Applying the filtered data to the radar processors to calculate the processors outputs using (2.9), it is seen from Figure 5.7-C and Figure 5.8-C that only one strong target appears in the output and the 2nd target is significantly suppressed (more than 20 dB

reduction) and the 3rd target is suppressed (more than 5 dB reduction). The same results are obtained when only one additive targets is exists, in other words when only one additive target exists, its signal is suppressed by 5 dB reduction and 20 dB reduction for the near target and far target, respectively. As seen in Figure 5.7-B and Figure 5.8-B, the resulting monopulse curve for the three targets scenario with FrFT are slightly different to their original values (only one target). As a result the problem of the distortion due to the 3rd target in the monopulse look direction has been resolved. The resultant STDAE using (2.18) for different SNR (20:100 dB) for the conventional processor is low (average value less than 0.3) as shown in Figure 5.7-D. In Figure 5.8-D the STDAE for the spatial processor in case of three targets using FrFT are particularly low (average value less than 0.3). The higher values for STDAE in this case because the 3rd target is nearer to the radar than the 1st one. In other words if the 3rd target is in the background of the 1st target, the STDAE will reduce to 0.1 (similar to the two target scenario).

The previous suppression of the additive targets signals power and also the enhancements in the STDAE values were tested for up to six targets (3 near target and 3 far targets) and generally a similar SNR reduction of approximately 20 dB was observed for all far targets while a SNR reduction of approximately 5 dB was observed for all near targets.

5.3 A New Structure of Monopulse Radar for Mitigate High Power Interference

In the previous section (section 5.2), the mistracking problem due to additional far and near targets appearing in the radar look direction along with the tracked target that leads to potential target mistracking especially in fire and forget tracking systems was addressed using the filtering in the optimum FrFD (FrFT-ATF). A very high improvement in the radar tracking ability for different target SNR was gained by using the proposed FrFT-ATF based on FrFD cancelling technique (more than 20 dB reduction for the far targets and more than 5 dB reduction for the near targets).

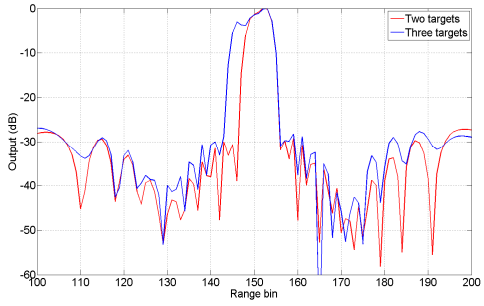

(A)

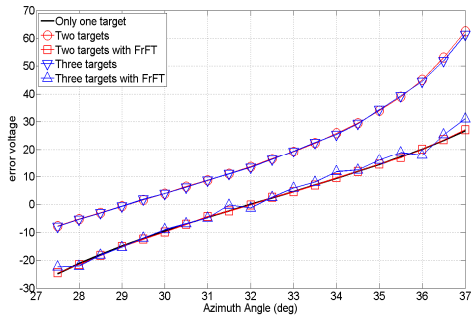

(B)

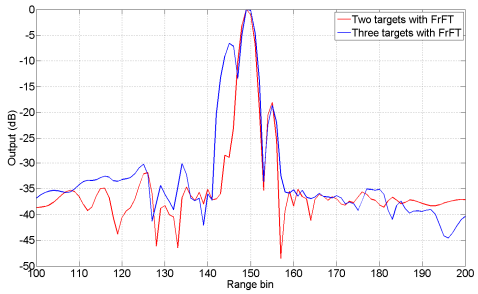

(C)

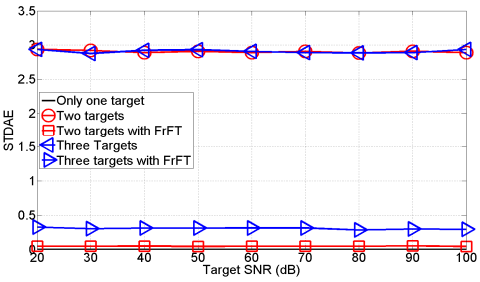

(D)

Figure 5.7 Conventional
(A) processor output (No Filtering).
(B) error voltage curve.
(C) processor output (FrFT Filtering).
(D) STDAE.

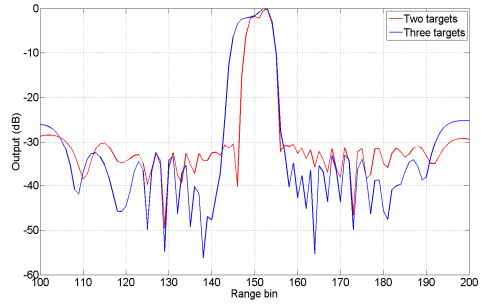

(A)

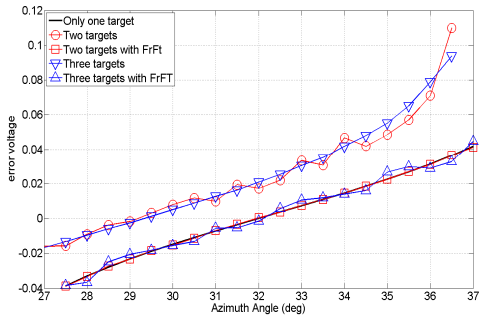

(B)

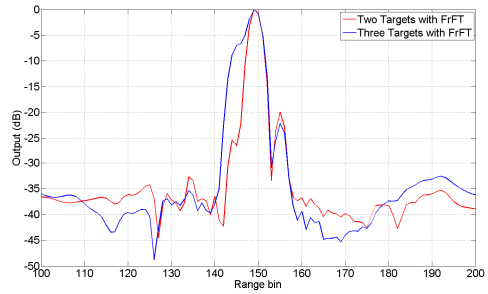

(C)

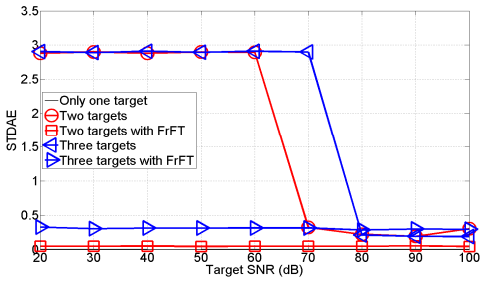

(D)

Figure 5.8 Spatial adaptive
(A) processor output (No Filtering).
(B) error voltage curve.
(C) processor output (FrFT Filtering).
(D) STDAE.

In this section a new monopulse based FrFT processor is presented. The FrFT monopulse processor algorithm uses FrFT optimal noise interference filtering (FrFT-NIF) to significantly reduce the effect of high power interference (jamming) signals.

Seliktar et al. [37] presented a monopulse processor to reduce the effect of the noise interference prior to target information extraction. Our new FrFT filtering algorithm depends on the range information extracted from the sum channel output in the monopulse processor (conventional monopulse and spatial adaptive processor). This output (that still remains noisy) is used as a guide when FrFT filtering of the received signal is carried out to enhance interference suppression.

5.3.1 The FrFT-NIF algorithm

The proposed FrFT noise interference filtering (FrFT-NIF) based monopulse processor is illustrated in Figure 5.9. It comprises a conventional monopulse processor subsystem along with additional FrFT and related processing blocks. The new FrFT based monopulse processor replaces the conventional monopulse processor seen in Figure 2.14. Thus in the new monopulse radar structure, a pulsed chirp signal $c(t)$ defined in (2.5), produced by the waveform generator, is up-converted to the radar carrier frequency, amplified and passed through the duplexer to be transmitted.

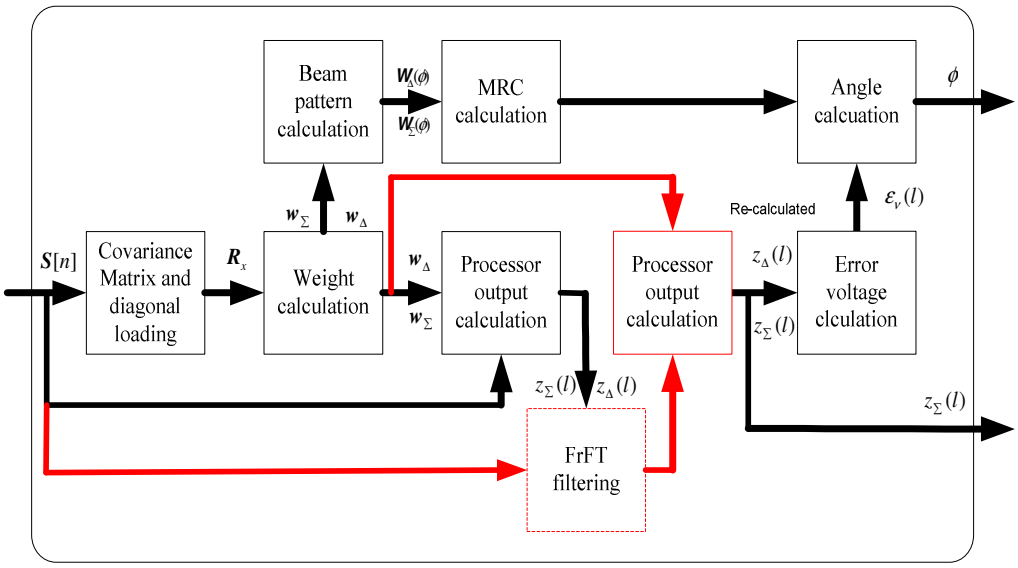

Figure 5.9 New structure of the proposed FrFT based monopulse processor

The down-converted received signal $s(t)$ passes through a band limited Gaussian filter before passing through the chirp matched filter to maximize the target return signal. The target information parameters are then calculated by the monopulse processor (conventional monopulse and spatial adaptive processor) from $z_{\Sigma}(l)$. The target range (the range bin number) with the optimal fractional order information from the chirp waveform generator is used to determine the target position in the optimum FrFD from (5.2). This position is used in the FrFT filtering by canceling the noise in the FrFD before transforming back to the time domain using the inverse FrFT. The filtered radar data is used again to re-calculate the target information parameters. The optimal FrFT filtering process illustrated in Figure 5.10 (dashed block in Figure 5.9) consists of N receiving channels in which the received signal from each of the N antenna elements will fill L range gates. The total radar data size is therefore equal to $N \times L$ for each pulse return. The optimum FrFD is calculated for each receiving channel data with size $1 \times L$ to filter the signal in the FrFD. The resultant filtered data (useful signal) is converted back from the optimum FrFD using an inverse FrFT to the time domain. The $1 \times L$ data output from N FrFT processors are re-processed to re-determine the target information parameters.

The following steps in Table 5.2 are involved in the proposed algorithm that may be used to cancel the noise interference signal:

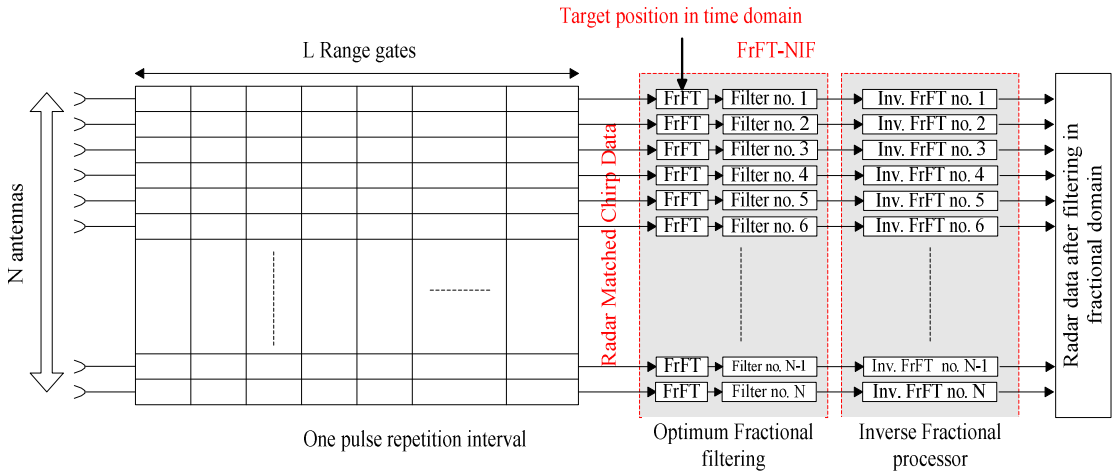

Figure 5.10 FrFT noise interference filtering radar data

Table 5.2 FrFT noise interference filtering (FrFT-NIF) algorithm

1	Calculate a_{opt} to determine the optimal FrFD for the tracked target signal from the information supplied from the waveform generator.
2	Calculate the target range information.
3	Calculate the peak position P_p of the target in the optimal FrFD
4	**For** $1 \le k \le N$ **do** (for each receiving channels), k is iteration index
5	Filter the received data by keeping the target data (peak position sample and its adjacent samples) and force all the remaining samples in the tracking window to zero.
6	Transform the filtered signal back to time domain using inverse FrFT with the known optimal order $-a_{opt}$.
7	**End**
8	Use the filtered $N \times L$ data to re-calculate the target information (target bin position, azimuth and elevation angles)

The mathematical description for the steps is now described. For the received target signal given by (2.20) overlapped with noise interference jamming signal $\boldsymbol{N}_{jam}$ by (2.24), a signal model of our radar system [3] with size $N \times L$ considering only one pulse return is:

$$\boldsymbol{Z} = \boldsymbol{S} + \boldsymbol{N}_{jam}. \tag{5.10}$$

The optimum FrFT order a_{opt} for the chirp can be computed by applying (5.2) to the radar system. From the target position in the return radar window, the chirp start time sampling number t_{st} is determined. Consequently the target peak position in the optimum FrFT can be calculated from (3.15). As all other variables in this equation are known as the peak position in the FrFD can be written as:

$$P_p = \sin(\theta_{opt})\left[\frac{-(\Delta f/2)}{(F_s/L)} + \frac{\Delta f\,(L/M_T)}{2(F_s/L)}\right] - \cos(\theta_{opt})\,t_{st}. \tag{5.11}$$

In each receiving channel, the peak position sample P_p and its adjacent samples (5

samples on both sides, the number of these samples depends on the estimate chirp band width in optimum FrFD) are kept and all other samples in the tracking window are set to zero to get the filtered data in the optimal FrFD $\boldsymbol{z}^{a_{opt}}$. The filtered signal $\hat{\boldsymbol{s}}$ in the time domain is obtained by applying the inverse FrFT using negative value for the same optimal operator $-a_{opt}$ (for each receiving channel) as:

$$\hat{\boldsymbol{s}} = F^{-a_{opt}}(\boldsymbol{z}^{a_{opt}}). \tag{5.12}$$

All the output signals from the N FrFT filters are then re-processed to get the target information parameters after applying the proposed filtering technique using (2.9) and (2.10).

During the re-calculation for the azimuth and elevation target angles, the weights $\boldsymbol{w}_{\Sigma}$ and $\boldsymbol{w}_{\Delta}$, which are generated using the noisy radar data, are kept and not re-generated using the new FrFD filtered data to maximize the benefit of the monopulse processors spatial cancelling as shown in Figure 5.9. Hence the processor output is generated using the filtered data in the optimum FrFD with the weights $\boldsymbol{w}_{\Sigma}$ and $\boldsymbol{w}_{\Delta}$ corresponding to the spatial distribution of the noisy radar data. This idea can be applied to different types of the spatial noise cancelling monopulse processor in conjunction with FrFT.

5.3.2 Simulation Results

In the simulations the radar comprises the same radar parameters considered previously in subsection 2.9.1. The target is considered at range bin=150 at angle 32^{o} from the look direction with SNR set to 50 dB with Doppler frequency 150 Hz.

5.3.2.1 Proposed FrFT filtering technique

To understand the proposed FrFT filtering algorithm (FrFT-NIF) applied to cancel noise interference in the radar data, the following jamming signal is injected to the target simulated signal with interference to noise ratio (INR) set to 82 dB at angle 32^{o} from the look direction (main beam jamming). Figure 5.11-A shows the absolute value for a noisy received signal in the 1st channel of the radar channels. This noisy signal is transformed to the optimum FrFD using the calculated optimum index a_{opt} equal to 1.7074

(Substituting the monopulse radar parameter values into (5.11)) and a spike for the target received chirp signal appears at fractional sample 205 as seen in Figure 5.11-B . Using the information that the target is detected at range bin 150, the P_p in the optimum FrFD exists at fractional sample 205 to confirm the target sample position (in case of very high interference scenario). In Figure 5.11-C all the samples in the tracking window in the FrFD are forced to zero except the samples from 200 to 210 (peak position sample and its five adjacent samples). The inverse FrFT with a_{opt} equal to -1.7074 transforms the filtered signal back to the time domain after filtering a shown in Figure 5.11-D (real and imaginary values) in Figure 5.11-E (absolute values). This process is repeated for all the receiver channels N . Hence the filtered radar data $N \times L$ is used to re-compute the azimuth, elevation target angles and processor output can then be computed.

5.3.2.2 Simulated Data Jamming Scenario

A jamming signal with INR set to 82 dB with two scenarios, first at angle 32^o from the look direction (main beam jamming) and second at angle 62^o from the look direction (side lobe beam jamming) are introduced. The jamming interference causes deviations in the monopulse error voltages from their original values (no jamming). This distortion affects the tracking angle of the tracked target resulting in a probable mistracking outcome. The error voltage is calculated from (2.10).

Figure 5.12-A shows the error voltage curve for the conventional processor. It is clear that in case of main lobe interference the curve is highly affected by interference so it is expected to get high STDAE while in the case of side lobe interference it is less affected by the interference and the error decreases to form a lower STDAE characteristic.

The error voltage curves for the spatial adaptive processor are shown in Figure 5.12-B. In the case of main lobe interference it is seen that the tracking angle is very sensitive to any change in the error voltage. This is due to the radar adaptive pattern which shifts to the left thus decreasing the beam width. On the other hand in case of side lobe interference the error voltage is nearly the same as when no interference which implies that the processor successfully cancels the noise interference signals.

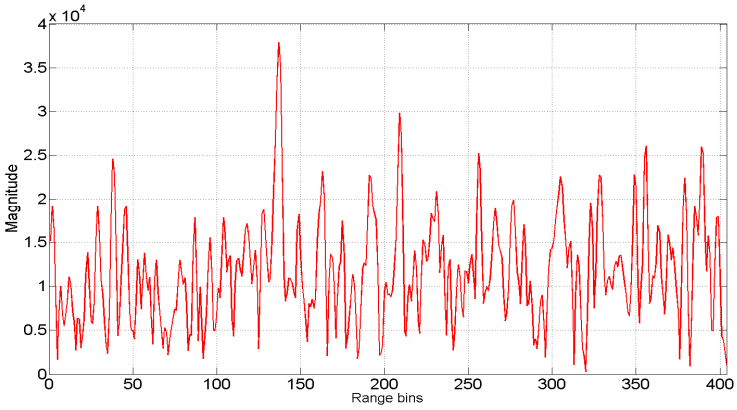

(A)

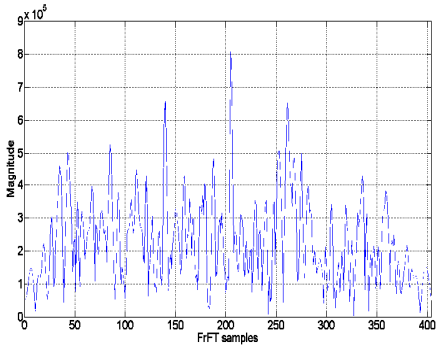

(B)

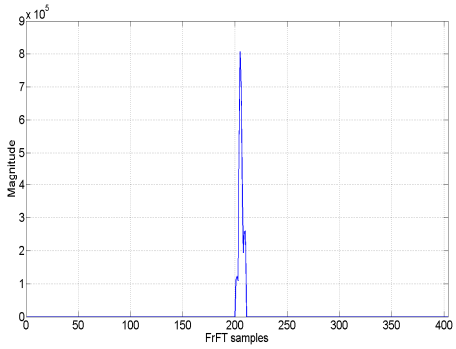

(C)

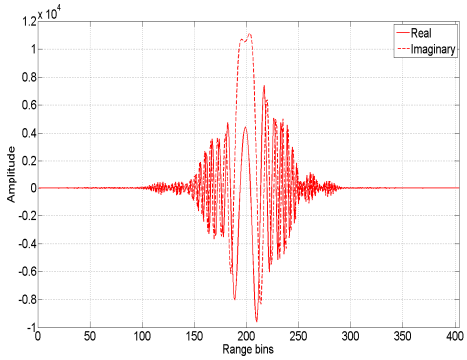

(D)

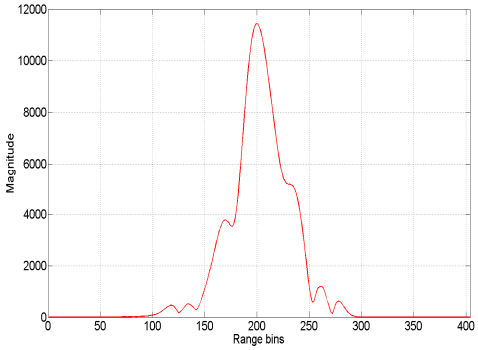

(E)

Figure 5.11 FrFT Filtering algorithm (FrFT-NIF) details

(A) absolute value for a noisy received signal.
(B) received signal in the optimum FrFD.
(C) NIF in the optimum FrFD.
(D) Fitered received signal.
(E) magnitude of the received signal.

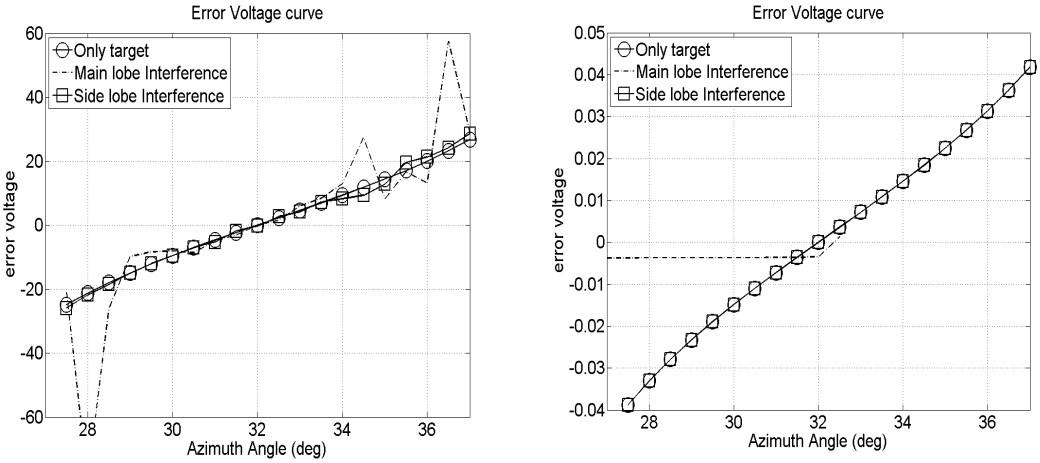

(A) (B)

Figure 5.12 Error voltage curves

The processors' outputs using (2.9) for target SNR=70 dB is shown in Figure 5.13-A and Figure 5.13-B for the main lobe interference and in Figure 5.14-A and Figure 5.14-B for the side lobe interference, for the conventional and spatial adaptive processors, respectively. In all these figures the target exists at range bin 150. Using FrFT filtering, the processors' output, in case of main lobe interference, decreases the noise level as seen in Figure 5.13-A and Figure 5.13-B. The noise interference signal is reduced by approximately 25 dB in the conventional case and by approximately 5 dBs in the case of the spatial adaptive processor. In the case of side lobe interference as shown in Figure 5.14-A and Figure 5.14-B, the proposed FrFT filtering technique helps to decrease the noise levels by approximately 12 dBs and 4 dBs at the outputs of the conventional and spatial adaptive processors, respectively.

Output *OINR* (7) is used to quantify the improvement. It is used to compare the mitigation performance for both monopulse processors using (2.19), knowing that the lowest *OINR* value represents the best mitigation performance. *OINR* values in Table 5.3 show that the FrFT filtering technique enhances the processors mitigation due to

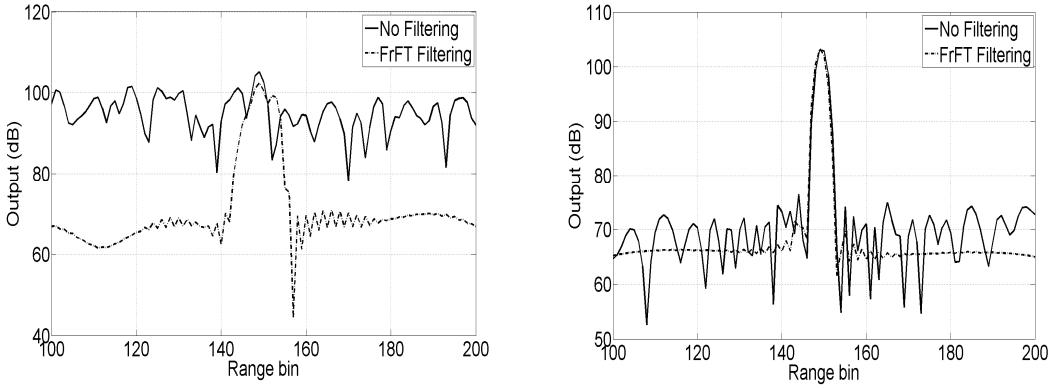

(A) (B)

Figure 5.13 Monopulse processor Outputs (main lobe)

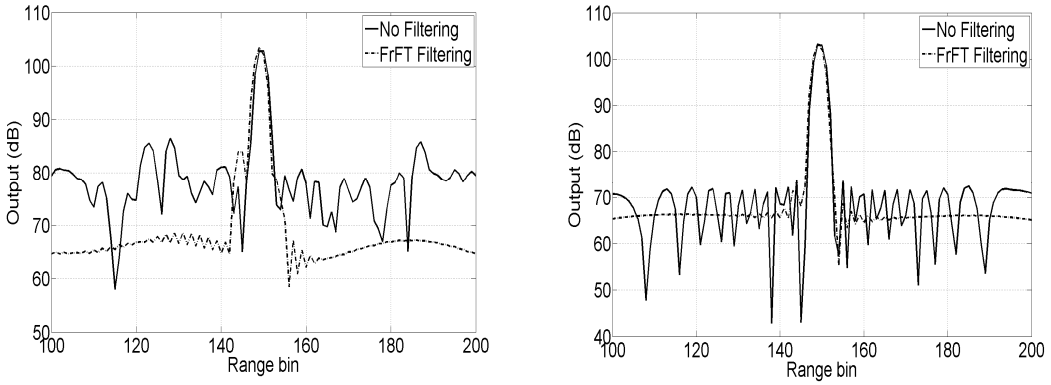

(A) (B)

Figure 5.14 Monopulse processor Outputs (side lobe)

noise for both jamming scenarios. From Table 5.3 it is observed that the *OINR* values for main lobe interference are always higher than those for the side lobe inference (that is clear because the distortion effect of side lobe interference is less than the main lobe interference). Also it is seen that the *OINR* values using FrFT filtering are always less than the *OINR* values without filtering (the proposed filtering technique helps to decrease the noise level for all processors in all noise interference cases). From Table 5.3 in case of conventional processor the *OINR* values are improved by approximately 15 dB and 9.7 dB for main lobe interference and side lobe interference, respectively, using FrFT filtering. In the case of spatial adaptive processor the *OINR* values are improved by approximately 3.6 dB and 9.5 dB for main lobe interference and side lobe interference, respectively.

Table 5.3 OINR in dB for monopulse processors

Monopulse processor	Main lobe interference	Side lobe interference
Conventional processor		
(a)No filtering	14.31	-3.3
(b)FrFT filtering	-1.33	-12.99
Spatial processor		
(a)No filtering	-19.69	-77.18
(b)FrFT filtering	-23.3	-86.75

Figure 5.15 and Figure 5.16 show the STDAE curves for the conventional and the spatial processors, respectively, for both cases of the interference scenarios. STDAE is calculated for different target SNR (from 20-100 dB). Particular values of STDAE are extracted from Figure 5.15 and Figure 5.16 and tabulated in Table 5.4. These show the SNR values at which both processors start tracking at the different interference scenario (main lobe and side lobe) for the conventional structure of the radar (No filtering) and proposed new structure (with FrFT filtering).

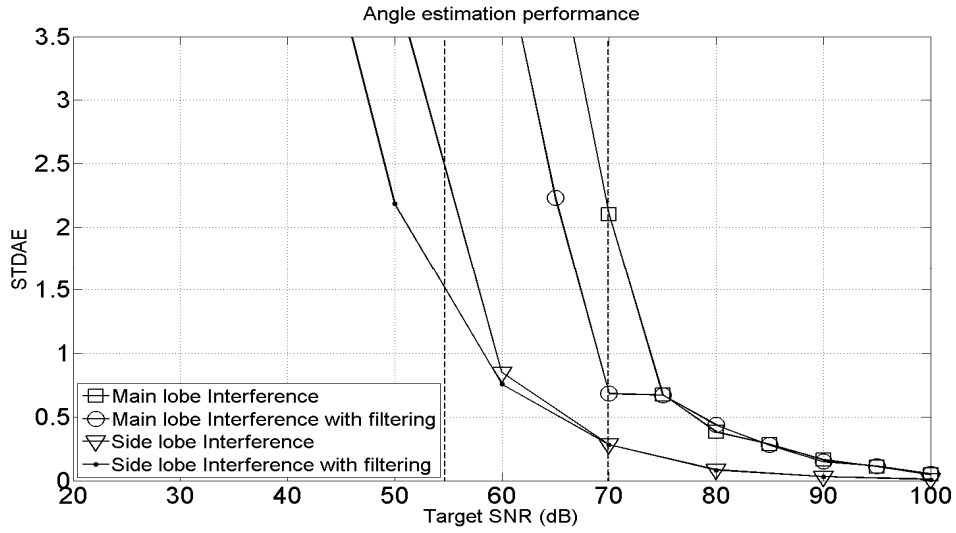

Figure 5.15 Conventional processor at main lobe and side lobe interference

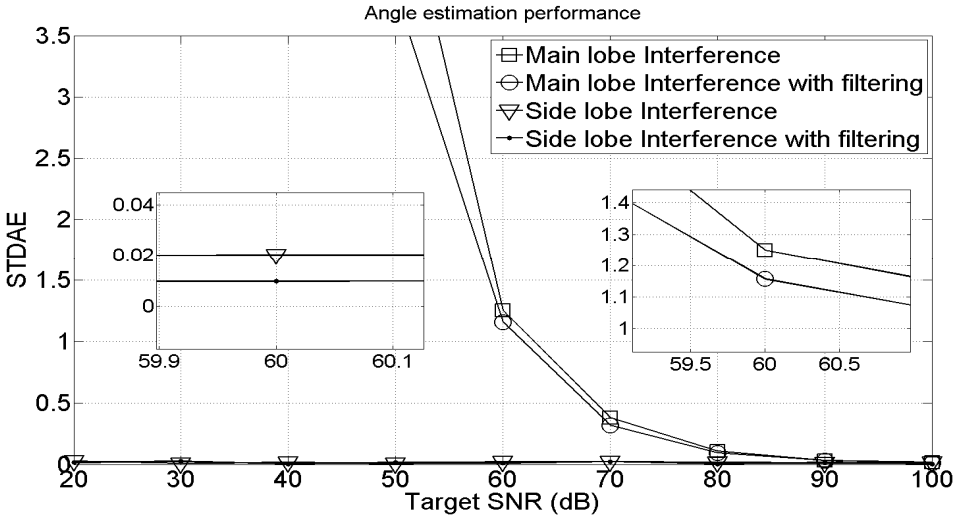

Figure 5.16 Spatial processor at main lobe and side lobe interference

Table 5.4 indicates an improvement of approximately 5 dBs in both interference scenarios for the conventional processor when using the FrFT based monopulse radar. In the case of spatial adaptive processor, Table 5.4 indicates an improvement of 3 dBs when using the FrFT based monopulse radar for the main lobe interference.

Figure 5.15 and Figure 5.16 show that for each target SNR the STDAE value decreases in the case of using FrFT filtering which indicates an improvement in the tracking performance. For example in Figure 5.15 at target SNR equal 70 dB (vertical dashed line) the STDAE value decreases from 2.1 to 0.7 in the main lobe jamming and at target SNR equal 53 dB (vertical dashed line) from 2.5 to 1.5 in the side lobe beam jamming. In a similar fashion Figure 5.16 shows at target SNR equal 60 dB (zoomed portion of the figure) the STDAE value decreases from 1.25 to 1.15 in the main lobe jamming. Also it is clear that in case of side lobe interference the processor succeeds in reducing the inference (very low STDAE about 0.02) while still providing lower STDAE values using FrFT filtering as shown in the zoomed portion of the figure in Figure 5.16.

5.3.2.3 Real Data Jamming Scenario

As a second experiment an evaluation of the new monopulse structure based FrFT filtering was conducted on real experimental dataset stap3001 mentioned in subsection 2.9.3.2.

In Figure 5.17 the STDAE is calculated for different target SNR (from 20-120 dB). Figure 5.17 and the corresponding extracted values in Table 5.5 indicate an improvement of approximately 2 dB in both processors at an STDAE value of 3.5 when using the FrFT based monopulse radar. From Figure 5.17 it is clear that for each target SNR the STDAE value decreases when using FrFT filtering. For example in case of the conventional processor at target SNR equal to 100 dB the STDAE value decreases from 2.2 to 1.8 and for the spatial processor at target SNR equal 60 dB from 1.15 to 0.95.

All previous STDAE values of the new monopulse based FrFT filtering structure are superior to those obtained from the conventional and the spatial processors at different target SNR using no filtering. For higher SNR the new system does not introduce a large enhancement to the tracking performance due to the fact that the target signal is much higher than the interference signal. The proposed system will work in an effective manner when one target is in the look direction with and without interference without any additional constrains on the radar processor so it can work with any monopulse processor.

Table 5.4 Target SNR at an STDAE value for both monopulse processors at different interference scenario (simulated data)

Monopulse processor	Main lobe interference		Side lobe interference	
	SNR	STDAE	SNR	STDAE
Conventional				
(a)No filtering	66.6	3.5	51.5	3.5
(b)filtering	61.6	3.5	46.5	3.5
Spatial				
(a)No filtering	54	3.5	20	0.02
(b)filtering	51	3.5	20	< 0.02

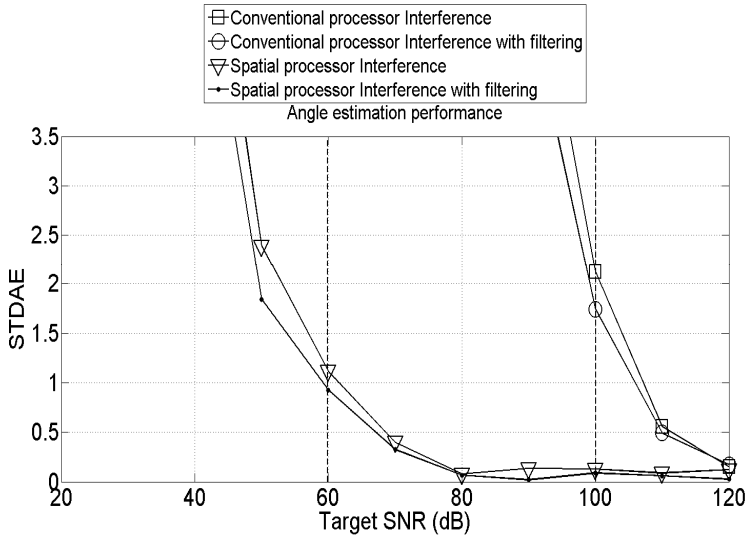

Figure 5.17 Monopulse processor at main lobe and side lobe Interference

Table 5.5 Target SNR at an STDAE value for both monopulse processors at different interference scenario (real data)

Monopulse processor	Side lobe interference	
	SNR	STDAE
Conventional		
(a)No filtering	96.5	3.5
(b)filtering	94.5	3.5
Spatial		
(a)No filtering	57.5	3.5
(b)filtering	55.5	3.5

5.4 Conclusion

In this chapter, solutions for the distortion problem due to the unwanted targets appearing in the monopulse look direction beam and the distortion resulting from jamming interference are presented. The following two subsections review the work presented and summarize its results.

A new monopulse system configuration with new FrFT filtering algorithm (FrFT-ATF) is used to overcome the problem of unwanted targets appearing in the monopulse look direction. The proposed system configuration with the optimum *N* FrFT filters succeeds to effectively reduce the additive targets' signal and minimize the STDAE for the both considered monopulse processors. A very high improvement in the radar tracking ability for different SNR (because of very low STDAE) is gained by using the suggested canceling technique (more than 20 dB reduction for the far targets and more than 5 dB reductions for the near targets). One of the key advantages of the proposed system is that it works in an excellent manner when only one target in the look direction (normal case) as well as when more than one target exists in the look direction.

The distortion resulting from jamming interference appearing in the monopulse main lobe and side lobe has been solved with a proposed FrFT algorithm (FrFT-NIF) based monopulse processor. The proposed monopulse radar system configuration successfully reduces the interference noise signal and minimizes the STDAE for the both considered monopulse processors compared to the monopulse radar without filtering. For both simulated and real experiments an improvement in the radar tracking ability for different SNR (lower STDAE) is gained by using the proposed FrFT based monopulse radar technique compared to the monopulse radar without filtering. It was experimentally observed that, for simulated jamming scenario, effective tracking (STDAE values of 3.5) started at a target SNR 5dB earlier for both conventional and the spatial adaptive processors using the FrFT based monopulse radar. In the case of real experimental data an improvement of 2 dB was measured. One of the key advantages of the proposed system is that it will work efficiently even when no jamming (normal case).

6. EMD Based Monopulse processor

6.1 Introduction

In the previous chapter, the FrFT-NIF algorithm is introduced to decrease the distortion produced when manmade high power jamming is introduced to the monopulse radar that may affect the induced target error voltage and consequently the radar tracking ability. In this chapter, another signal processing algorithm, EMD, is used to address the same problem to enhance the monopulse tracking performance. Also another filtering algorithm (EMD-FrFT) based on the hybrid use of EMD and FrFT. EMD-FrFT filtering is carried out for complex noisy radar chirp signals to decrease the signal's noisy components.

This chapter is consists of two main section (6.2 and 6.3) to introduce new algorithms to overcome the monopulse distortion problems mentioned previously in addition to Section 6.4 that conclude this chapter. This chapter is organized as follows: Section 6.2 proposes a new monopulse radar that employs an EMD based monopulse processor to reduce the interference due to high power jamming. Later on Section 6.2, a set of simulation results is presented for different jamming scenarios at different target SNR that demonstrates the superior performance of the new structure. Section 6.3 proposes a new EMD-FrFT interference filtering algorithm. A set of simulation results is presented for the received signal improvement at different SNRs is also introduced. The last part of this chapter is Section 6.4, it concludes the chapter.

6.2 A New EMD Based Structure of Monopulse Radar for Mitigate High Power Interference

Flandrin et al [96, 103] suggests applying EMD algorithm to reconstruct a signal from some of the non-noisy IMFs. In the technique a threshold energy model is used to determine the number of IMFs where the energy crosses a particular threshold. The sum of these IMFs is considered as the non-noisy part of the original noisy signal. Kopsinis et al [98] developed a denoising technique inspired by translation invariant Wavelet thresholding method that were applied to the EMD signal to cancel the additive noise and enhance the SNR. In this section, denoising techniques for complex chirp signals by applying bivariate EMD to the received radar signal with the resultant real and imaginary IMFs treated as two identical paths are developed.

In the new EMD based structure of monopulse radar [17, 18], EMD filtering is carried out for the complex radar chirp signal with subsequent detrending, thresholding, and denoising processes. These processes are used to decrease the noise level in the radar processed data to improve the signal to noise ratio. The performance enhancement using the monopulse radar tracking system with EMD based filtering is included using the STDAE for different jamming scenarios and different target SNRs. The proposed system configuration is shown to reduce the interfered signal and to minimize the STDAE for high power interference signal presence in the main lobe and side lobe.

In the proposed EMD filtering method, the radar signal is processed using a proposed EMD filtering algorithm to reduce the interference noise before supplying the received radar data to the processor output calculator. EMD denoising is introduced in this section as a method to enhance monopulse processors not as separate noise cancelling processor. Monopulse processors are superior in spatial noise cancelling while EMD based filtering improves its temporal noise cancelling with an overall enhanced tracking performance.

6.2.1 A New Monopulse Radar Structure

The proposed EMD based monopulse radar is illustrated in Figure 6.1. It comprises a conventional monopulse subsystem along with an additional high frequency sampler and

a new monopulse based EMD processor. Again, a pulse chirp signal $c(t)$ defined in (2.5) is produced from the waveform generator and is up-converted to the radar carrier frequency, amplified and passed through the duplexer to be transmitted. The down-converted received signal passes through a high frequency sampler before being passed to the new monopulse based EMD processor.

As seen in Figure 6.1 the new monopulse based EMD processor obtains the received radar high sampled data $s'[n]$ from the high frequency sampler with a sampling frequency F_s'.

6.2.2 New EMD Based Monopulse Processor

The detailed construction of the proposed monopulse based EMD processor is shown in Figure 6.2. It starts by splitting the input signal, $s'[n]$ into two paths. In the first path the signal is down sampled to the sampling frequency F_s of the radar system. This path uses the basic monopulse processor. The signal in the second path passes through the EMD filtering algorithm block (that will be described in subsection 6.2.3) before being down

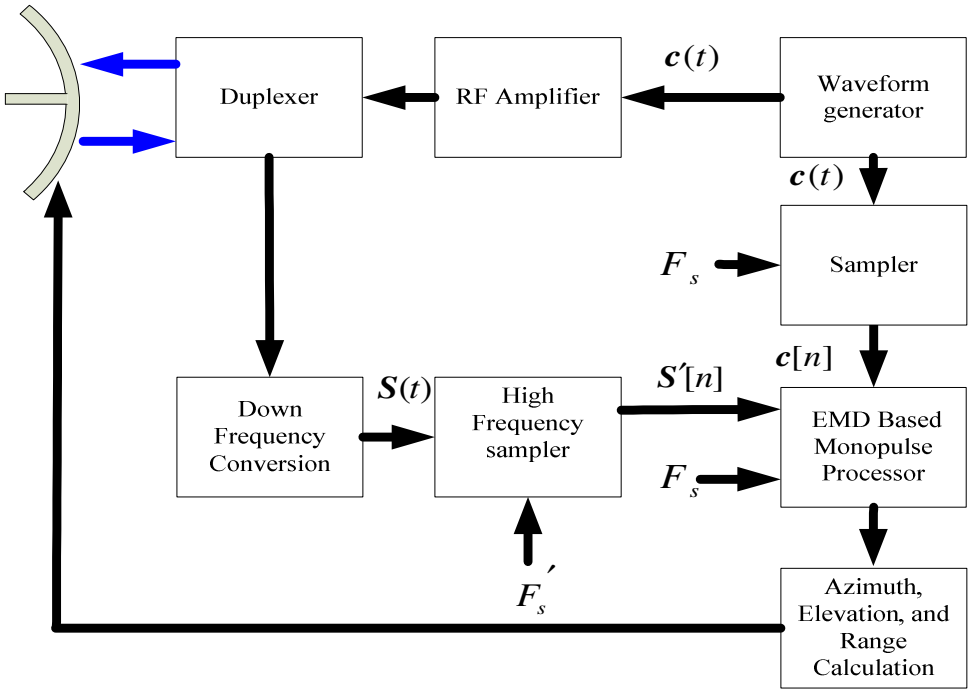

Figure 6.1 Proposed monopulse radar

sampled to the regular sampling frequency F_s of the radar system. Subsequently the filtered output is down sampled to produce the filtered $s[n]$ before passing through the Gaussian band pass filter. The filtered data is input to a chirp matched filtering process to maximize the target return signal. As mentioned previously the EMD denoising is introduced as a method to enhance monopulse processors and not as a separate noise cancelling processor.

The filtered matched signal is multiplied by the weights calculated from the original data to produce the sum and difference outputs $z_{\Sigma}(l)$ and $z_{\Delta}(l)$, respectively, from (2.9). This new monopulse processor structure keeps the enhancement in SNR introduced by weights calculation for adaptive processors (weight are calculated from the original data before EMD filtering) in addition to the SNR enhancements introduced by EMD filtering to the data before the calculation of the sum and difference outputs (multiplying the unchanged weight generated from the original data with the filtered EMD data).

6.2.3 EMD Filtering Algorithm

In Figure 6.3, the high sampled complex chirp radar signal return is input to a bivariate EMD to produce the complex IMFs. The bivariate EMD complex IMFs are input to two identical paths, one for the real IMFs and one for the imaginary IMFs. The real IMFs are detrended and thresholded to estimate the non-noisy IMFs according from (3.36)-(3.39).

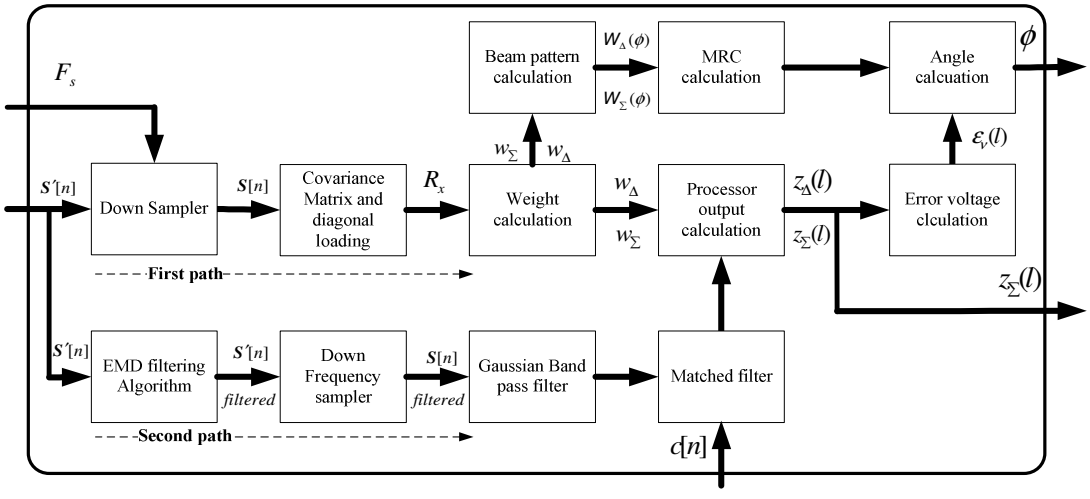

Figure 6.2 EMD based monopulse processor

Only IMFs whose energy exceeds the threshold as in (3.38) are kept. The real non-noisy IMFs pass through the denoising algorithm block which applies one of the denoising algorithms EMD-IT, EMD-IIT, and EMD-CIIT mentioned in subsection 3.3.3. The resultant thresholded IMFs are combined to produce the real part of the signal (detrended, thresholded, and denoised). The imaginary IMFs are processed in a similar fashion. Finally the real part and imaginary part of the signal are combined to produce the complex filtered signal. The EMD filtered signal is down sampled to the sampling frequency used in the radar system to continue data processing. All the output signals from the N EMD filters are then passed to the matched filter and supplied to the processor output calculation as illustrated in Figure 6.2.

6.2.4 Simulation Results for EMD Based Monopulse Processor

In the simulations the radar comprises the same radar parameters considered previously in subsection 2.9.1. For target signal to noise ratios (SNR) set to 40, 60, 80, 100 dB, respectively, with a jamming signal with interference noise ratio (INR) set to 75 dB at angle 32^o from the look direction (main beam jamming) is considered with the simulated radar system. The improvement in output SNR after applying EMD filtering using the three denoising algorithms (EMD-IT, EMD-IIT, and EMD-CIIT) is given in

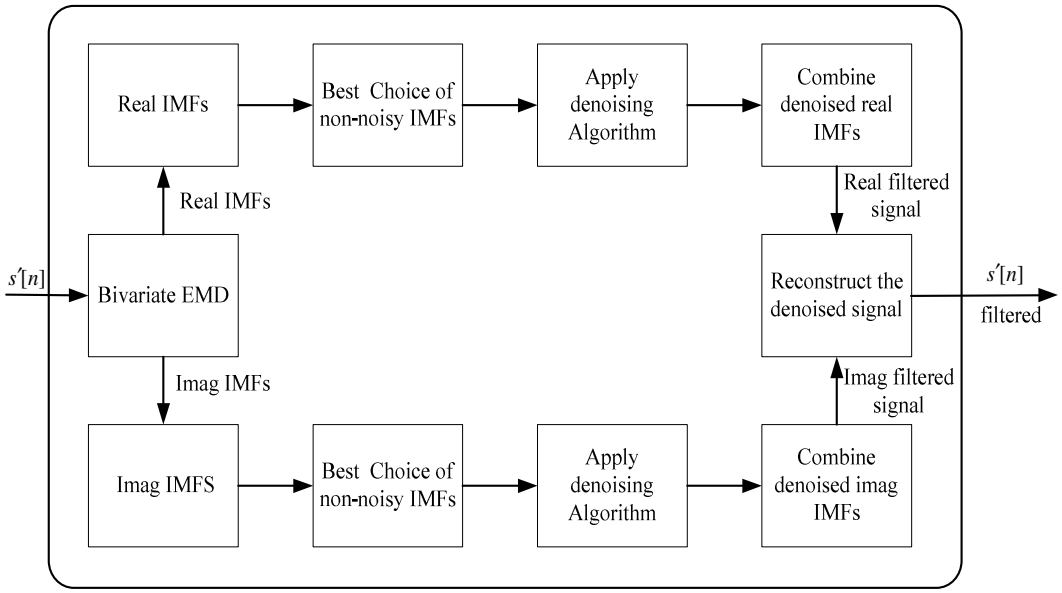

Figure 6.3 Proposed EMD Filter Structure

Table 6.1. Hard thresholding has been employed and the number of iterations is 20 with a fixed number of sifting equal to 8. The results comprise an average over 50 independent noise generations.

Table 6.1 is used to find an algorithm and a sampling frequency that provides a gain for the complete range of target SNRs. From Table 6.1 it is observed that a sampling frequency F_s' = 10 MHz (10 times the radar sampling frequency F_s) and the CIIT denoising method are the best choice. This result is used in the rest of simulation results. Although higher gains are observed in Table 6.1, these are only obtained for specific values of target SNRs and sampling frequency.

6.2.4.1 EMD Filtered Chirp Radar Signal

The real and imaginary part of the received signal $s(t)$ which is over sampled to $s'[n]$ when no jamming signal comprises a chirp signal that starts at bin 1500 (target range) and pulse width of 1000 bins (100 msec.) with a target signal SNR=70 dB and interference noise ratio (INR) set to 75 dB at angle 32^o with sampling frequency F_s' = 10 MHz are shown in Figure 6.4-A and Figure 6.5-A, respectively. In Figure 6.4-B and Figure 6.5-B, the real and imaginary part of the received signal is highly corrupted with the jamming signal.

The distortion affects the tracking angle of the tracked target resulting in a probable mistracking outcome.

Table 6.1 : Signal gains at different sampling frequency for different denoising methods

Sampling frequency	1 MHz			10 MHz			30 MHz			50 MHz		
Denoising method	IT	IIT	CIIT	IT	IIT	CIIT	IT	IIT	CIIT	IT	IIT	CIIT
Target SNR [dB]	Gain [dB]											
40	**13.12**	**14.42**	**19.15**	**11.94**	**13.90**	**13.62**	**11.07**	**12.90**	**13.21**	**12.35**	**13.94**	**14.75**
60	**12.32**	**13.66**	**16.38**	**7.89**	**9.26**	**9.22**	**4.91**	**7.23**	**5.61**	**4.35**	**6.63**	**3.81**
80	**3.3**	**3.32**	**4.65**	**3.64**	**6.61**	**6.83**	**2.69**	**4.677**	**4.06**	**3.14**	**5.30**	**3.22**
100	**-5.19**	**-5.49**	**-4.93**	**3.33**	**3.41**	**4.80**	**2.73**	**3.61**	**3.80**	**2.74**	**3.97**	**4.16**

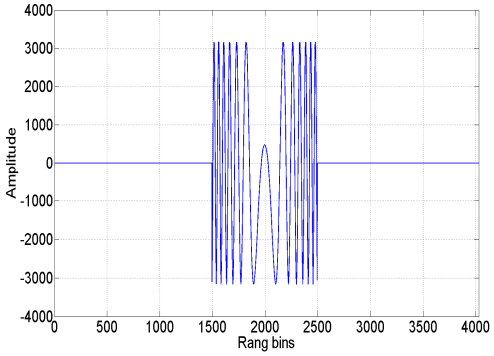

(A)

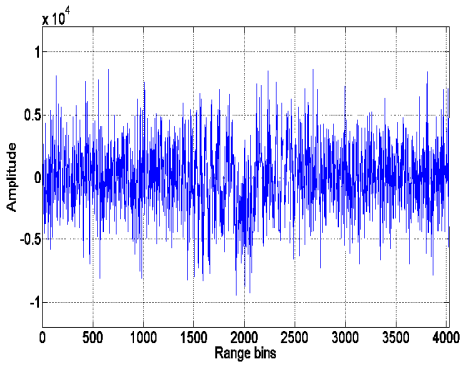

(B)

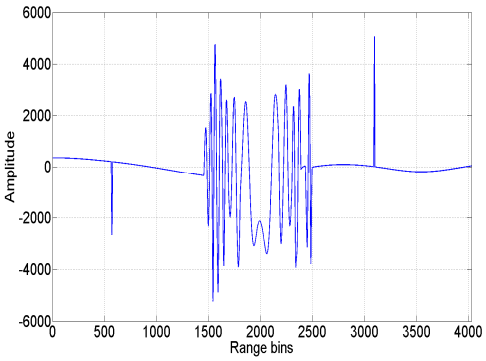

(C)

Figure 6.4 Received signal real part
(A) no jamming
(B) with jamming and no filtering
(C) with jamming and EMD filtering

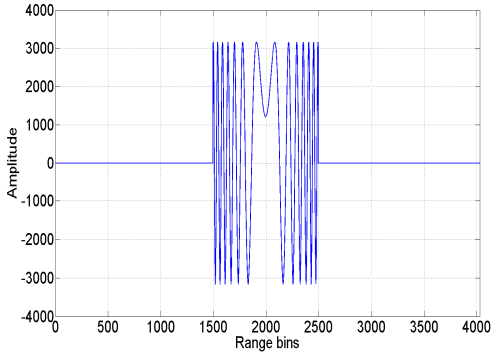

(A)

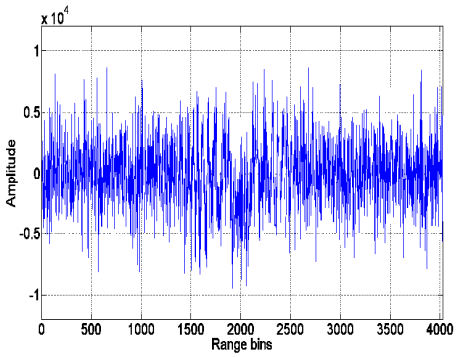

(B)

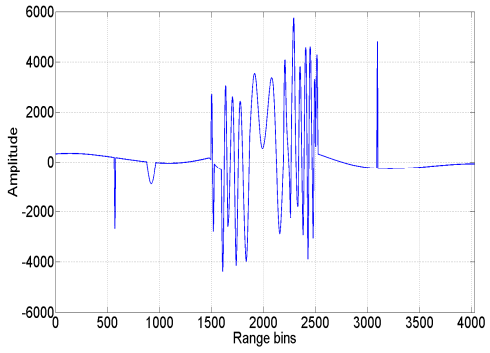

(C)

Figure 6.5 Received signal imaginary part
(A) no jamming
(B) with jamming and no filtering
(C) with jamming and EMD filtering

The EMD filtered signal is shown in Figure 6.4-C and Figure 6.5-C. It is clear that from these figures that the jamming interference signal is highly reduced and the enhancement

in the signal is significant using the EMD-CIIT. A SNR gain equal 6.98 dB (average of 50 noise generations) is achieved.

In the next subsection the EMD filtering process is applied to chirp radar signal which is our main interest in this subsection. However as indicated in Appendix G it can also be applied for different signals shape with different SNR.

6.2.4.2 Simulated Jamming Scenario

In this jamming situation (interference noise ratio (INR) set to 75 dB and target signal SNR=70 dB both at angle 32^o) the conventional and the spatial processor outputs using (2.9) are seen in Figure 6.6 and Figure 6.7, respectively. It is clear from Figure 6.6 that the target appears with high noise level in the case of the basic structure of monopulse processor (no EMD filtering). The noise level decreases by approximately 10 dB (improves the target SNR output as seen in Table 6.1) and the target can be resolved at range bin 150 using complex EMD filtering as illustrated in Figure 6.6. For the spatial processor the noise level decreases about 10 dB in a similar fashion and the target level w.r.t the noise is also subsequently improved as illustrated in Figure 6.7.

The tracking radar system performance is measured by STDAE in (2.18). The higher the STDAE the less the tracking performance achieved. STDAE is calculated for different target SNRs (from 20-100 dB) for a jamming scenario with high power interference noise ratio (INR) set to 82 dB with two angles, first at angle 32^o from the look direction (main beam jamming) and second at angle 62^o from the look direction (side lobe beam jamming) are introduced.

The STDAE at each SNR is calculated by determining the half power beam width of the radar pattern at the radar look direction which changes according to the weights calculation of the received radar data (for main beam jamming the radar pattern is tapered and shifted away from the interference and in side lobe jamming it puts null in the jamming direction). The target signal is injected at each angle using a resolution of 0.5^o in the look direction beam width. STDAE is calculated at each of these angles from (2.18) and the considered STDAE at the radar look direction is the maximum value of these STDAEs.

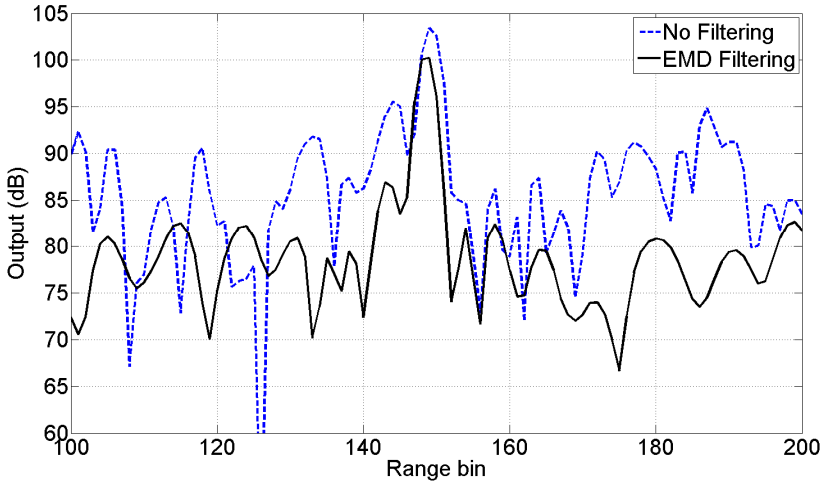

Figure 6.6 Conventional processor output

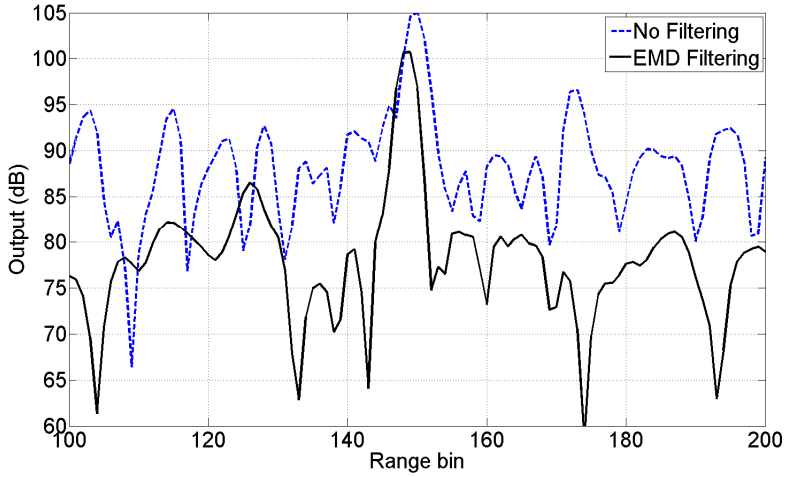

Figure 6.7 Spatial adaptive processor output

In Figure 6.8, the STDAE is presented for both main lobe and side lobe interference for the conventional monopulse processor with and without EMD filtering. It is clear that for each target SNR the STDAE value is lower in the case of using the new EMD based filtering processor with a resulting improvement in the tracking performance. For example at target SNR equal 70 dB (vertical dashed line) the STDAE value decreases from 3.15 to 2.2 for main lobe jamming and from 0.56 to 0.23 in the case of side lobe beam jamming.

The STDAE for the spatial adaptive monopulse processor is lower using EMD filtering

in the case of main lobe interference as shown in Figure 6.9. For example at target SNR equal 70 dB at the STDAE value decreases from 1.7 to 1.1 in the main lobe jamming. However in the case of side lobe interference EMD filtering fails to make improvements in STDAE. This is because the characteristic of the spatial adaptive processor is superior as it actually places a null in the interference direction. For example at target SNR equal 70 dB the STDAE value increases from 0.21 with no filtering to 0.94 with EMD filtering in the case of side lobe interference at angle 42^o. In the case of side lobe interference at angle 62^o the spatial adaptive processor can mitigate the interference better than in the case at 42^o as observed by the lower STDAE that are obtained at lower SNR (without EMD filtering) which is seen to be slightly better than that obtained using EMD filtering. The STDAE values are approximately similar for the spatial adaptive processor with and without EMD filtering in the case of 62^o for a target SNR higher than 40 dBs.

In Figure 6.8 and Figure 6.9, it is observed that the higher the SNR, the less enhancement is noticed in the STDAE values due to the fact that the target signal power is increased. This is highlighted in the zoomed area in both figures.

6.2.5 Discussion

Figure 6.8 and Figure 6.9 show that an improvement in the radar tracking ability for different SNR (lower STDAE) is gained by using the EMD filtering monopulse radar

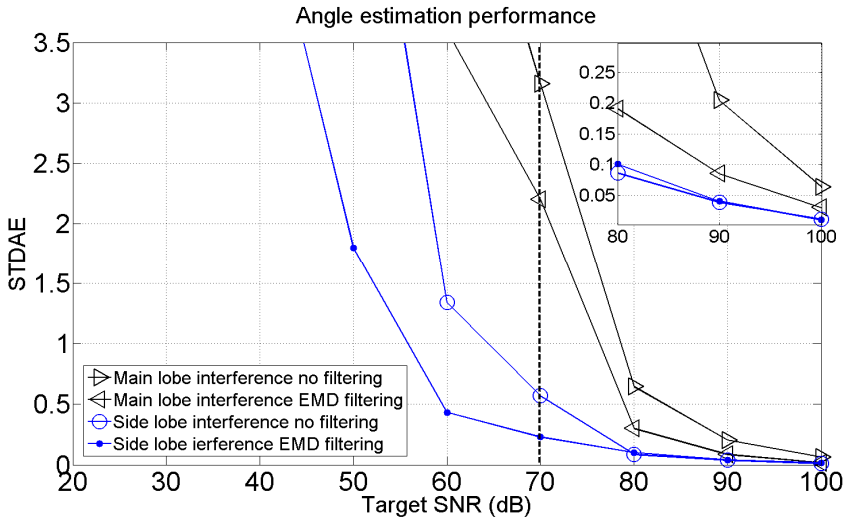

Figure 6.8 STDAE for Conventional processor configuration

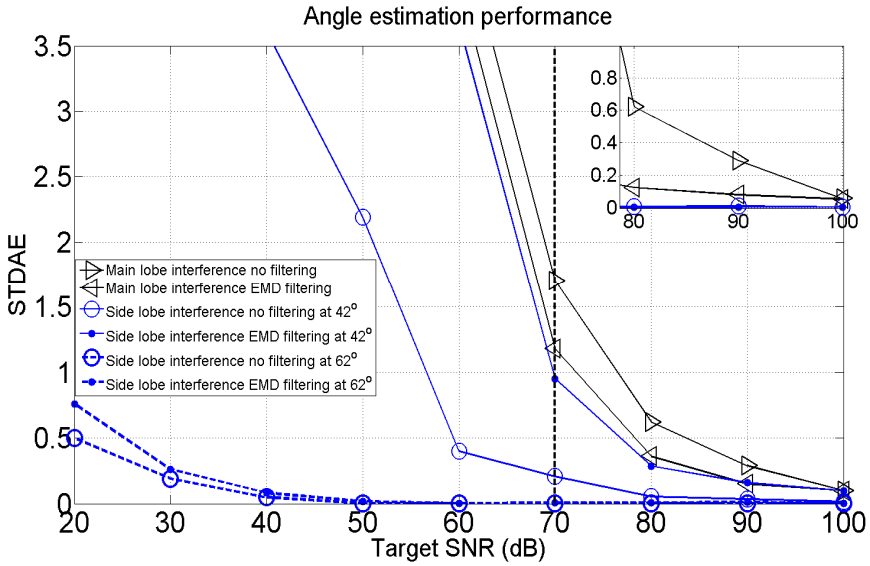

Figure 6.9 STDAE for Spatial adaptive processor configuration

however it does not provide any enhancement (higher STDAE) in the case of side lobe inference for the spatial adaptive processor. This behaviour may be explained as follows:

(1) The spatial distribution of the target signal (over the antenna elements and over the range cells) is very important information for monopulse tracking radar. It is used to determine the target angle and hence affects the STDAE calculation. Therefore it is essential to keep the phase information unchanged during filtering technique in monopulse radars. Filtering the noisy signal in two paths (real and imaginary) as shown in Figure 6.3 enhances the resultant SNR for both paths and thus enhances the overall SNR as seen previously in Table 6.1. However this process cannot preserve phase relation between the real and imaginary parts of the target data especially in the lower SNR situations.

(2) In the spatial adaptive processor, the angle measurements depend on the weights $\boldsymbol{w}_{\Sigma}$ and $\boldsymbol{w}_{\Delta}$. These weights depend on the spatial distribution of the tracked target and also the additive noise. So any change in the phase information of the filtered data will affect $z_{\Sigma}(l)$, $z_{\Delta}(l)$ and consequently will affect the error voltage $\varepsilon_{v}(l)$ especially in side lobe interference. However in the case of main beam interference the spatial adaptive processor tends to be less dependant on the received data because in this case no nulls can be placed in the look direction.

It is concluded that the improvement in the STDAE values for the EMD based conventional processor incase of main lobe and side lobe interferences is due to the fact that the processor obtains lower STDAE (high tracking performance) at the higher SNR (60-100 dB) and its weights are fixed. Similarly the main lobe interference in the EMD based spatial adaptive processor yields an improvement due to the fact that it yields lower STDAE at higher SNR (60-100 dB) and its weights tend to similar to the weights in the case of the conventional processor. The higher values of STDAE in the case of side lobe interference for the spatial adaptive processor are obtained because this processor obtains high tracking performance (lower STDAE) at lower SNR (from 40 dB) and the weights depend on the received radar data spatial distribution.

6.3 Filtering Based EMD-FrFT Algorithm

In our previous work, the mistracking problem due to interference signals was addressed using FrFT-NIF algorithm (section 5.3) and using EMD (in section 6.2). In Section 6.3 the use of both EMD and FrFT to implement N EMD-FrFT filters in an attempt to reduce the very high power interference signals introduced from the radar antenna.

Normally the magnitude of chirp signal in the optimum FrFT domain would be significantly higher than the noise signal in the FrFD. However in high power jamming scenarios this is not usually true and it becomes difficult to distinguish between the target spike and the noise spikes in the optimal FrFT domain. Thus, EMD-FrFT algorithm is proposed to combat the high power noise interference by filtering the received signal in the optimal FrFD using the transmitted chirp radar information after applying EMD filtering.

The proposed EMD-FrFT radar filtering process, which must be applied to the received signal before the band pass filter, is shown in Figure 6.10. The radar received noisy complex chirp signal $s(t)$ is sampled using the radar sampling frequency to form $s[n]$. The $s[n]$ signal recovery is carried out in two stages: (i) EMD filtering stage and (ii) FrFT filtering stage.

EMD filtering stage

In stage one the received signal $s[n]$ is input to a bivariate EMD to produce the complex IMFs $\boldsymbol{h}^{(i)}[n]$. The complex IMFs are detrended and thresholded to estimate the non-noisy IMFs using (3.36)-(3.39) as described in subsection 3.3.2. Only IMFs whose energy exceeds the threshold are retained. The resultant thresholded IMFs are combined to produce the complex denoised signal as in (3.40).

FrFT filtering stage

For the second stage, the complex denoised signal in the optimal FrFD is calculated from the information supplied from the transmitted chirp signal as in (3.14).

The following steps in Table 6.2 are involved in the proposed EMD-FrFT filtering algorithm that may be used to cancel the noise interference signal.

Table 6.2 EMD-FrFT noise interference filtering algorithm

1	Calculate a_{opt} to determine the optimal FrFD for tracked target signal from the information supplied from the waveform generator as in (3.14).
2	**For** $1 \le k \le N$ **do** (for each receiving channels), k is iteration index
3	Apply EMD filtering stage.
4	Transform the EMD filtered received radar to the optimal FrFD using (3.1) and (3.2).
5	Estimate the peak position sample of the target in the FrFD.
6	Filtering the received data by keeping the target data (peak position sample and its adjacent samples) and force all the rest of the samples in tracking window to be equal to zero.
7	Transform the filtered signal back to time domain using inverse FrFT with the known optimal order $-a_{opt}$.
8	**End**
9	Use the filtered $N \times L$ data to calculate the target information (target bin position, azimuth and elevation angles)

The EMD-FrFT filtered data is supplied to the radar processor to continue data processing to calculate the target information.

The EMD-FrFT filtering process illustrated in Figure 6.10 is attached to N receiving channels in which the received signal from each of the N antenna elements will fill L range gates. The total radar data size is therefore equal to $N \times L$ for each pulse return. The EMD-FrFT filter block consists of N EMD-FrFT filters shown in Figure 6.10. The overall filtered data ($N \times L$) are processed to determine the target information parameters.

6.3.1 Simulation Results for EMD-FrFT Algorithm

In the simulations the radar comprises the same radar parameters considered previously in subsection 2.9.1. The target is considered at range bin=150 at angle 32^o from the look direction with target signal to noise ratio (SNR) set to 56 dB. A jamming signal with interference noise ratio (INR) set to 75 dB at angle 32^o from the look direction (main beam jamming) is introduced.

6.3.1.1 High Power Interference Scenario

Considering the simulation parameters for one of the 14 receiving channels (1st channel), the receiving target chirp signal appears at range bin 150 in case of no jamming while the chirp signal is completely corrupted in the time domain (also in the frequency domain) by the noise due to high power jamming signal as seen in Figure 6.11.

The bivariate EMD is applied to the noisy signal to produce the complex IMFs. Due to the fact that the higher the number of samples, the higher the accuracy of detrending

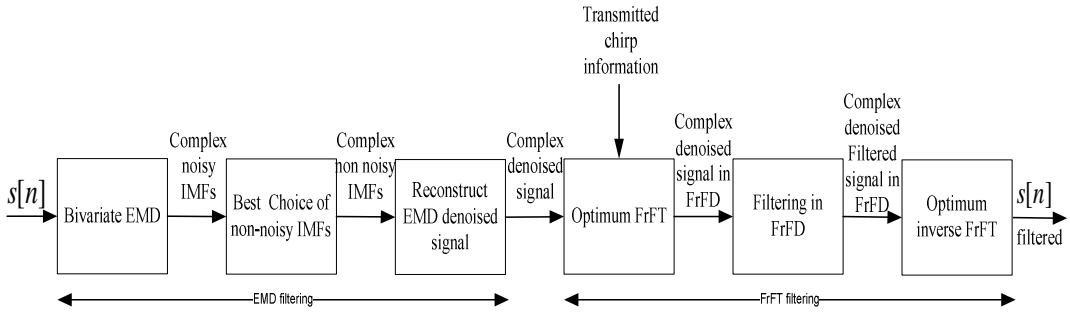

Figure 6.10 EMD-FrFT filtering

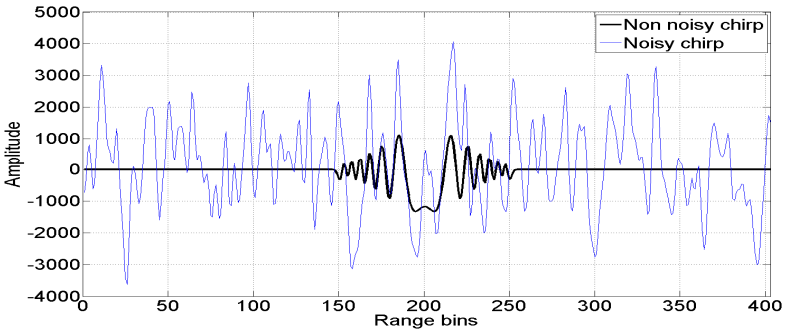

Figure 6.11 High noisy chirp signal in time domain (real)

IMFs in EMD-DT algorithm, so the sampling frequency is increased to 10 MHz (10 times the radar sampling frequency F_s). The resultant complex IMFs from applying the bivariate EMD to the noisy chirp 1×4029 produces 14 IMFs each of length 4029. Keeping only IMFs whose energy exceeds the threshold using the EMD-DT algorithm described in subsection 3.3.2 the signal is reconstructed summing the non-noisy IMFs from 6-14 to obtain the filtered signal after applying EMD-DT algorithm.

Substituting the monopulse radar parameter values given above into (3.14) with a high sampling frequency of 10 MHz, the order of the optimal FrFT domain a_{opt} is computed as 1.1266. The EMD filtered signal is transferred to the optimal FrFD using the optimal order FrFT domain a_{opt} 1.1266.

Transforming the radar received signal directly to the optimum FrFD using the calculated a_{opt}, is expected to produce a high magnitude value (spike) due to transferring the chirp signal to the optimum FrFD. However as seen in Figure 6.12, due to the high power interference, the spike of the target chirp is highly corrupted also by noise spikes in the optimum FrFD and cannot be filtered in this domain.

It is therefore difficult to distinguish between the target spike and the noise spikes in the optimal FrFD. The proposed EMD-FrFT filtering algorithm is used to address this problem. Figure 6.13 shows the EMD denoised chirp in optimum FrFD. It is evident that the noise is significantly reduced especially the high frequency components and the chirp target spike is also the highest spike which is shown in the zoomed portion of Figure 6.13.

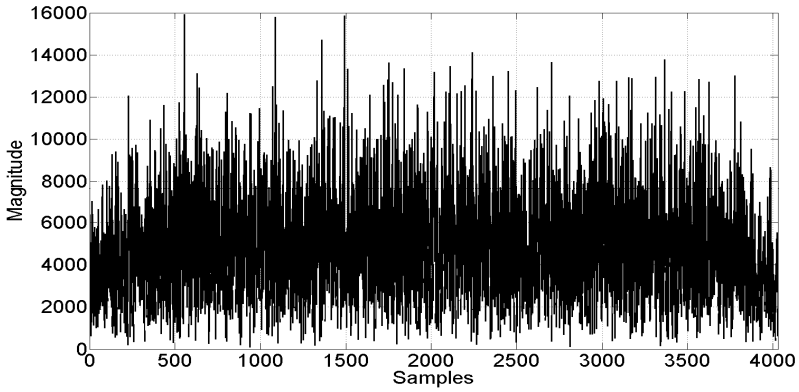

Figure 6.12 High noisy chirp signal in optimum FrFD

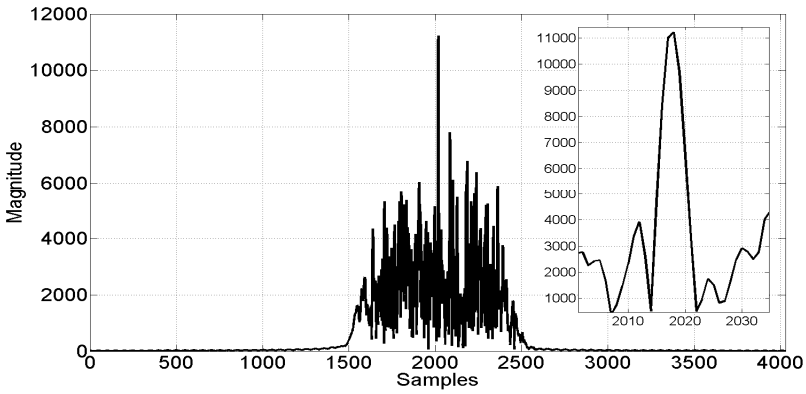

Figure 6.13 EMD denoised chirp in optimum FrFD

The proposed filtering algorithm in the optimum FrFD keeps the sample with maximum magnitude (sample no. 2018) and its 10 adjacent samples from 2013-2023 while forcing all other samples window to zero. The filtered signal is then transformed back to time domain by applying inverse optimum FrFT using $-a_{opt}$ (-1.1266) by applying (3.1). The real and imaginary parts of the denoised signal (recovered) after applying the proposed EMD-FrFT filtering algorithm is shown in Figure 6.14.

Figure 6.14 compares the denoised chirp signal using EMD-FrFT filter with the non noisy signal. In the simulation example, the considered signal total input SNR is approximately equal -8 dB (after adding the jamming noise) and the output SNR is approximately 10 dB. The proposed EMD-FrFT filtering algorithm offers signal enhancement of approximately 18 dB.

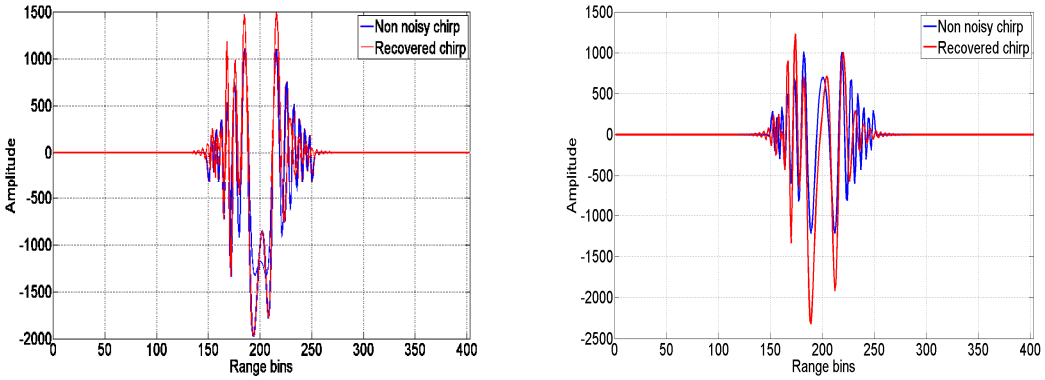

(A) real (B) imaginary

Figure 6.14 Recovered chirp signal

6.3.1.2 Signal Improvement at Different SNR

Table 6.3 shows the improvement results of applying different target SNR for the same jamming scenario (INR set to 75 dB at angle 32^{o}) and calculating the total input SNRs to the radar receiving channel. The results in Table 6.3 comprise an average over 50 independent noise generations.

Table 6.3 indicates an improvement of approximately 18.1 dBs for input SNR= -7.7 dB and an improvement of approximately 4.9 dBs for input SNR=10.6 dB. The proposed EMD-FrFT algorithm yields a higher improvement for the lower SNRs rather than the higher SNRs.

Table 6.3 INR for monopulse processors

Input SNR (dB)	-7.7	-5.6	-2.9	-1.8	0.2	1.7	5.6	10.6
Output SNR (dB)	10.4	10.8	13	13.4	14.8	15.4	15.8	15.5
Gain (dB)	18.1	16.4	15.9	15.2	14.6	13.7	10.2	4.9

6.4 Conclusion

In this chapter, solutions for the distortion problem resulting from high power jamming interference are presented. The following two subsections review the work presented and summarize its results.

A new solution to the distortion problem in the monopulse tracking radar due to high power manmade interference was presented. The distortion resulting from jamming interference appearing in the monopulse main lobe and side lobe has been investigated. The proposed new EMD based monopulse radar system configuration with *N* EMD filters successfully reduces the interference noise signal for the new monopulse processors compared to the basic monopulse processor structure (without EMD filtering) in the case of main lobe high power interference. A resulting improvement in the radar tracking ability for different SNR (lower STDAE) is gained by using the EMD filtering monopulse radar however it does not provide any enhancement in the case of side lobe inference for the spatial adaptive processor. One of the key advantages of the proposed system is that it works efficiently even when only one target in the look direction (normal case) and there is no high power interference exists.

A proposed EMD-FrFT filtering algorithm to reduce the distortion problem due to high power interference in chirp radar systems is presented. This algorithm successfully decreases the high power noise interference and improves the received radar SNR. A resulting improvement in the radar received signal is obtained for different SNR and the highest gain is achieved in the case of lower SNR (up to 18 dB in the considered case).

7. Conclusion and Future Work

7.1 Introduction

The primary aim of the work described in this thesis was to explore and develop new signal processing techniques for monopulse tracking radars. The key achievements of the research are two fold. A new monopulse radar processor based filtering algorithm was developed to solve the interference problem due to more than one target appears in the monopulse radar half power beam width. The second objective was to investigate algorithms to mitigate the problem of high power interference (jamming) introduced to the radar processor and enhance the monopulse radar tracking performance. This chapter concludes the research work presented and indicates areas where future work could be directed.

7.2 Conclusion

This thesis focused on interference cancelling techniques associated with monopulse radars and was based on new non traditional signal processing tools and methods that provide enhanced tracking performance and reduced signal interference.

The review of the monopulse radars (sum and difference) and the most important factors that affect its operation and performance with brief introduction to different monopulse processors, its advantages and limitations were presented in chapter 2.

A discussion on FrFT and EMD algorithms that are used to design and implement advanced monopulse radar systems is introduced in chapter 3. FrFT is the generalized formula for the Fourier transform that transforms a function into an intermediate domain between time and frequency. Signals with significant overlap in both the time and frequency domain may have little or no overlap in FrFD thus transforming signals into a particular FrFD may help in minimized or complete cancellation of the effect of undesired signals. EMD was developed for analysing non-linear and non-stationary real

and complex data thus it is used with monopulse radar data. Many EMD filtering algorithms are used to filter the noisy data depends on the EMD decomposing such as EMD-DT, EMD-IT, EMD-IIT, and EMD-CIIT.

Matched filters in the Fourier domain and the FrFD were investigated in chapter 4. The limitation of using matched filter in the optimum FrFT for a chirp was shown to be dependent on the chirp shape in this domain, on the chirp start time and chirp band width. The complexity of FrFT matched filter increases compared to the normal FT matched filter. An average improvement is gained by using FrFT matched filter compared to the FT matched filter for different input SNRs. A reduction in the widths of the FT matched filter output to that of the FrFT matched filter output is occurred and a significant reduction in side lobe using the FrFT matched filter is achieved in the cases studied in chapter 4.

Solutions for the distortion problem due to the unwanted targets appearing in the monopulse look direction beam using FrFT-ATF algorithm and the distortion resulting from jamming interference using FrFT-NIF algorithm are presented in chapter 5. A new monopulse system configuration with new FrFT filtering algorithm (FrFT-ATF) is used to overcome the problem of unwanted targets appearing in the monopulse look direction. A very high improvement in the radar tracking ability for different SNR is gained by using the suggested canceling technique. A proposed FrFT algorithm (FrFT-NIF) based monopulse processor is used to mitigate the distortion resulting from jamming interference appearing in the monopulse main lobe and side lobe has been solved with. The proposed monopulse radar system configuration successfully reduces the interference noise signal and minimizes the STDAE for the both considered monopulse processors compared to the monopulse radar without filtering.

Finally, chapter 6 presented another signal processing algorithm, EMD, for the problem of high power manmade interference to enhance the monopulse tracking performance. Also it introduce another filtering algorithm (EMD-FrFT) based on the hybrid use of EMD and FrFT. Firstly, a new EMD based monopulse radar system solution to the distortion problem in the monopulse tracking radar due to high power manmade interference. The new system configuration successfully reduces the interference noise

signal for the new monopulse processors compared to the basic monopulse processor structure in the case of main lobe high power interference however it does not provide any enhancement in the case of side lobe inference for the spatial adaptive processor. Secondary, A proposed EMD-FrFT filtering algorithm to reduce the distortion problem due to high power interference in chirp radar systems is presented. This algorithm successfully decreases the high power noise interference and improves the received radar SNR. A resulting improvement in the radar received signal is obtained for different SNR and the highest gain is achieved in the case of lower SNR.

7.3 Future Directions

Based on the research presented throughout this thesis, the following areas are of interest for potential further investigation:

Combination of FrFT-ATF and FrFT-NIF algorithms: both algorithms used separately to overcome the problem of additive targets in the look direction and high power interference, respectively. A combination of both algorithms (FrFT-ATF and FrFT-NIF) in the same monopulse processor to reduce the additive targets' signals and mitigate the jamming noise simultaneously is to be addressed for different additive targets SNRs and different INRs for jamming signals at different insertion angles.

New monopulse processor based EMD-FrFT algorithm: the proposed EMD-FrFT filtering algorithm is used to reduce the distortion problem due to high power interference in chirp radar systems. A new monopulse processor based EMD-FrFT to be investigated to mitigate high power interference for different target SNR.

Non linear chirp radar: all the proposed filtering algorithms in this thesis are used with linear chirp monopulse radar**.** Non linear chirp radar are affected as the linear chirp radar with different types of interferences, adaptive formulas of the new algorithms may be used with the non linear chirp radar to mitigate the interference problems.

Other applications: the proposed algorithms and its applicability to work in many other areas of interest including sonar, biomedical engineering, and communications are to be addressed.

Appendices

A. Methods to Generate Sum and Difference Patterns

The main issue when designing both sum and difference patterns is that they must be characterized by a peak at boresight and a null there for the difference pattern. Also it is required that the resultant MRC is well slope. There are three main methods to generate the sum and the difference pattern as the following:

Displaced Beam Method (DBM)[37]

It is the most straight forward method, the sum and difference beams are the sum and difference of two orthogonal steering vectors cantered about boresight and separated by a normalized spatial frequency of $\frac{1}{N}$,

$$\boldsymbol{v}_{\Sigma} = \frac{\boldsymbol{a}\left(\nu_t + \frac{1}{2N}\right) + \boldsymbol{a}\left(\nu_t - \frac{1}{2N}\right)}{2}, \quad \boldsymbol{v}_{\Delta} = \frac{\boldsymbol{a}\left(\nu_t + \frac{1}{2N}\right) - \boldsymbol{a}\left(\nu_t - \frac{1}{2N}\right)}{2}, \tag{A.1}$$

where $\boldsymbol{v}_{\Sigma}$ and $\boldsymbol{v}_{\Delta}$ are the spatial steering frequency vectors for the sum and difference channel, respectively, $\boldsymbol{a}(\nu) = \frac{e^{-j\pi\nu(N-1)}}{\sqrt{N}}\left[1 \;\; e^{j2\pi\nu} ..... \;\; e^{j2\pi\nu(N-1)}\right]$ is the centre phase normalized steering vector in the look direction, ν is the spatial steering frequency, and ν_t is the spatial steering frequency snapshot at time instant t. The normalized spatial steering frequency ν is estimated from

$$\nu = f_c \Delta t = f_c D \sin\phi / c, \tag{A.2}$$

where f_c is the monopulse radar carrier frequency.

The conventional processor comprising two sets of weights set to the sum and difference weights vectors $\boldsymbol{w}_{\Sigma}$ and $\boldsymbol{w}_{\Delta}$, respectively, defined as [36, 40]:

$$\boldsymbol{w}_{\Sigma} = \boldsymbol{v}_{\Sigma}, \; \boldsymbol{w}_{\Delta} = \boldsymbol{v}_{\Delta}. \tag{A.3}$$

The sum and difference patterns $\boldsymbol{w}_{\Sigma}(\phi)$ and $\boldsymbol{w}_{\Delta}(\phi)$ are seen in Figure A.1-A1 and Figure A.1-B1, respectively. The difference pattern $\boldsymbol{w}_{\Delta}(\phi)$ has very good deep null at the look direction angle. The MRC shown in Figure A.1-C1 appears as a linear relation between the error voltage and the corresponding angle. Note that, the flatter the MRC, the greater the resulting error in angle reading for a given deviation of error voltage. Therefore, it is desirable to have a "well sloped" curve such as seen the next method.

Half Phase Reversed Method (HPRM)[10, 37, 47]

The sum weights are taken to be a steering vector in the look direction, and the difference weights are obtained by phase reversing the latter half of the components of the steering vector

$$\boldsymbol{v}_{\Sigma} = \boldsymbol{a}(\nu_t), \quad \boldsymbol{v}_{\Delta} = -j\boldsymbol{t}_d \boldsymbol{.a}(\nu_t), \tag{A.4}$$

where $\boldsymbol{t}_d = \left[1_{1\times\frac{N}{2}} \quad -1_{1\times\frac{N}{2}} \right]^T$. Substituting in (A.3), the monopulse sum and difference patterns $\boldsymbol{w}_{\Sigma}(\phi)$ and $\boldsymbol{w}_{\Delta}(\phi)$ are seen in Figure A.1-A2 and Figure D.1-B2, respectively. Figure A.1-B2 shows the difference weight $\boldsymbol{w}_{\Delta}(\phi)$ has little deep null at the look direction but a very good sloped curve for MRC as seen in Figure A.1-C2.

Derivative method (DM)[37, 40]

The sum weights to be a steering vector in the look direction and the vector of difference weights to be the derivative of the steering vector with respect to normalized spatial frequency

$$\boldsymbol{v}_{\Sigma} = \boldsymbol{a}(\nu_t), \ \boldsymbol{v}_{\Delta} = \left. \frac{\partial \boldsymbol{a}(\nu)}{\partial \nu} \right|_{\nu_t}, \tag{A.5}$$

The monopulse sum and difference patterns $\boldsymbol{w}_{\Sigma}(\phi)$ and $\boldsymbol{w}_{\Delta}(\phi)$ are seen in Figure A.1-A3 and Figure A.1-B3. The difference pattern $\boldsymbol{w}_{\Delta}(\phi)$ has little deep null at the look direction. Figure A.1-C3 shows that the MRC is a very good sloped curve which is the best requirements for monopulse pattern.

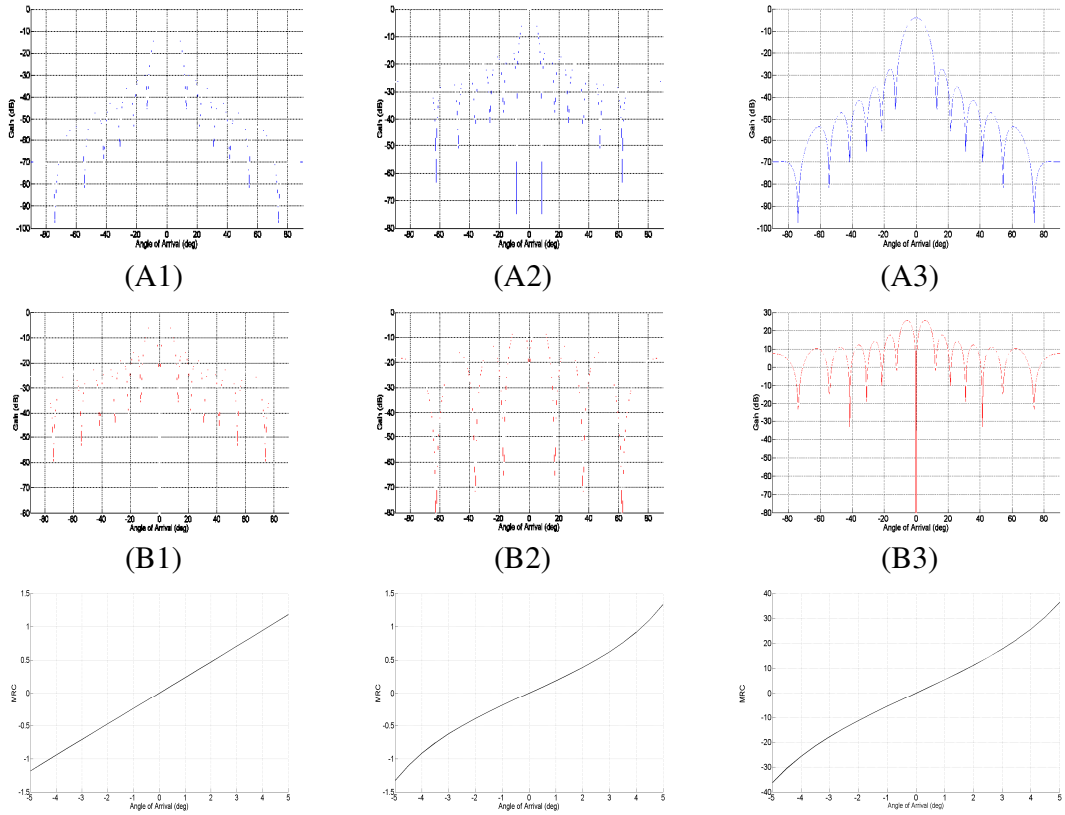

(A1) (A2) (A3)

(B1) (B2) (B3)

(C1) (C2) (C3)

DBM HPRM DM

Figure A.1 Methods to generate sum and difference patterns

B. Covariance Matrix Estimation

In this Appendix, the data from the CPI should be used as secondary data (data that contains little or no target signal) is determined. The approach is to use as few range bins as possible so as to exclude the assumed target bin as much as possible. In order to minimize the extent in range of the secondary data, the advantage of the availability of multiple CPI's is considered. Figure B.1 shows how the target bins are removed from CPI to construct the secondary data.

As an example with one CPI and for one antenna, consider the following illustrative example:

xxxxxxxxxxxxSSSSSSSSTTTTTSSSSSSSSxxxxxxxxxxxxx

where range bins that contain target information are indicated with a "T" and those that may be considered secondary data with an "S". Those marked with an "x" is considered left over range bins that are not used. In this example five bins are assumed to contain target info, while 16 bins are used as secondary data. With additional CPI's, less "S"

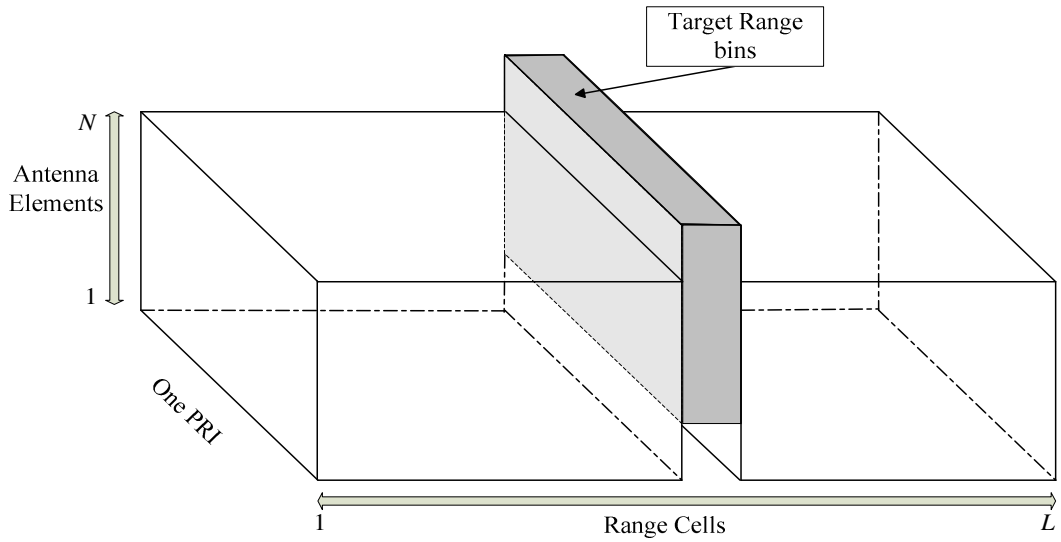

Figure B.1 Range bins excluding from CPI

bins can be used from each CPI and thus reduce the range extent of the secondary data if needed.

Considering the secondary data $\boldsymbol{X}_{SEC}$ is of length $N \times (L - \kappa)$, where κ is the number of range bins occupied by target data, the covariance matrix $\boldsymbol{R}_x$ can be estimated as

$$\boldsymbol{R}_x = \frac{\boldsymbol{X}_{SEC}\, \boldsymbol{X}_{SEC}^{H}}{L - \kappa}. \tag{B.1}$$

C. Optimization Criterion

To generalize the monopulse concept to SFT (space fast time) it is required to:

- Directly minimize angle estimation error
- Exercise control over the spatial /temporal response of the processor so that the effects of target spreading and overlapping targets are reduced.

To achieve both requires a highly nonlinear solution that is not of practical consideration. In Table C.1, a comparison between Maximum likelihood angle estimation (ML) and Min variance technique (MV) (the 2^{nd} method is used in our work to implement the monopulse radar in SFT) is provided.

Table C.1 A comparison between ML and MV as angle estimator

Maximum likelihood angle estimation (ML) [42, 43]	**Min variance technique (MV) [37, 44]**
• ML offers direct minimization capability for the spatial case. • The simplified form of the ML criterion in isotropic noise suggests that it is particularly suitable for monopulse processors. On the other hand, for non isotropic noise interference the standard monopulse criterion does not yield the best angle estimate. • Since the general solution is nonlinear, computing it can be difficult. However, by making certain assumptions and simplifying approximations, Davis et al. [12] were able to arrive at closed form solutions to the ML estimator. Note that non isotropic noise and interference (barrage noise jammers, MSC, and TSI) prevent conventional monopulse processing and ML angle estimation from being equivalent. • There is a lack of control over the SFT responses of the sum and difference processors.	• MV provides a simple linear solution that allows for a controlled response. However, because the angle estimation is not the criteria being optimized, a small but acceptable price may be paid in terms of angle estimation performance. • In other words, the use of linear constraints in MV allows the designer to exercise a great deal of control over both the spatial and temporal behavior of the SFT sum and difference processors, thus assuring robustness by providing a means to avoid target spreading and other distorting effects. The disadvantage of the linearly constrained approach is that it cannot be used to directly to minimize an angle estimation performance criterion as is the case with the maximum likelihood approach. At best it is able to minimize the residual interference in the respective sum and difference outputs.

A comparison between MV and ML based on simulated results

In order to make the comparisons fair, the angular region over which the search takes place corresponds to the angular region used in the analysis of the MV monopulse processor (i.e., the invertible MRC region within the beam width of the MV processor). For both techniques a Monte Carlo simulation method for an on-boresight target was used to arrive at STDAE performance. The resultant STDAE for different SNR for both methods is shown in Figure C.2 [6].

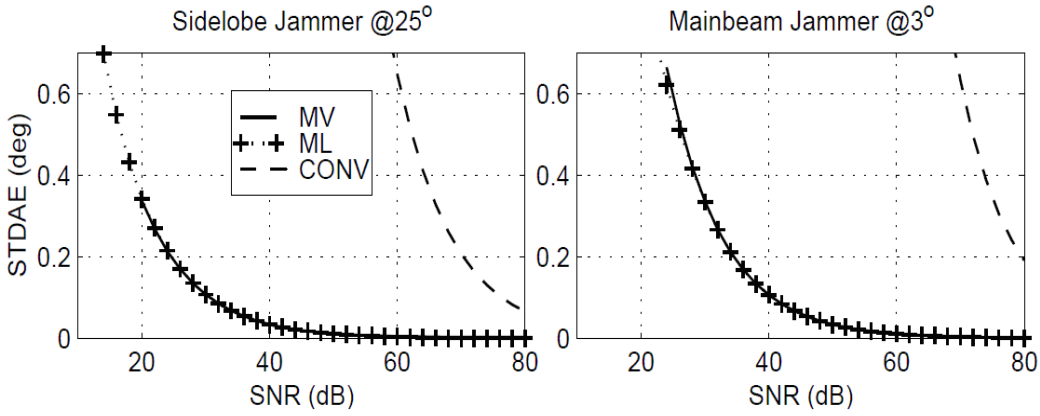

Figure C.2 STDAE for different SNR for MV and ML

The curves for MV and ML approximately overlap for both side lobe and main beam jamming, suggesting that indeed the MV technique may be a good approximation to the ML technique, if the SNR is high enough. Clearly both ML and MV improve significantly over the conventional monopulse processor (dashed).

D. Optimum FrFT Order of Chirp Signal

A general linear chirp signal $c(t)$ formula can be written as

$$c(t) = Exp[\, j2\pi(\gamma t^2 + \varepsilon t + \rho)]\,, \tag{D.1}$$

where γ is the chirp rate parameter and ε, ρ are constants. The chirp instantaneous frequency f_{inst} is the derivative of chirp phase as[62, 92]

$$f_{inst}(t) = 2\gamma t + \varepsilon\,. \tag{D.2}$$

Thus, the relation between the chirp rate γ and the optimum FrFT index a_{opt} can be shown in Figure D.1.

As mention previously in section 3.2.4, the relation between optimum FrFT order a_{opt} and the optimum FrFT order θ_{opt} is given by

$$\theta_{opt} = a_{opt}\,\pi/2\,. \tag{D.3}$$

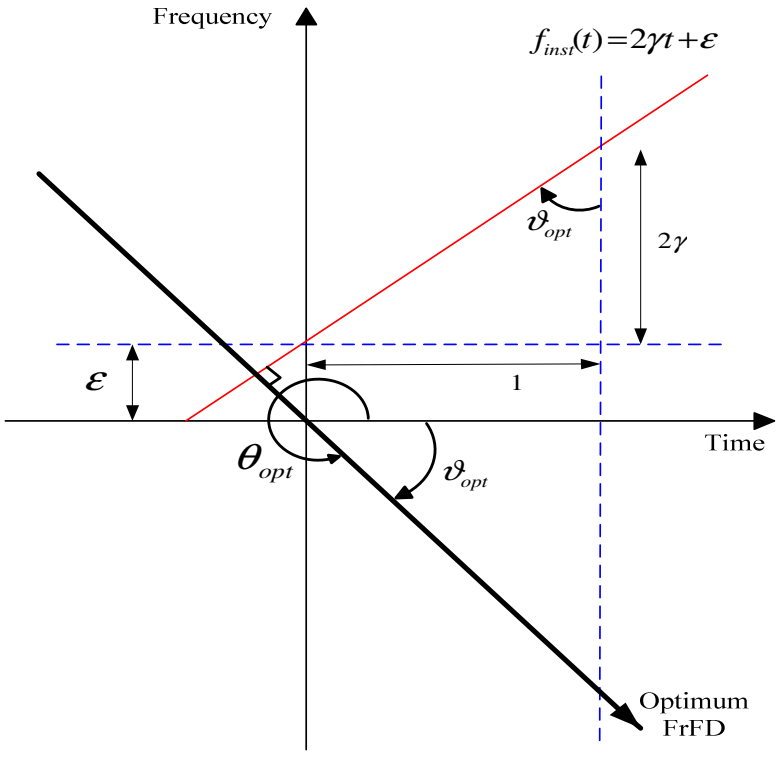

Figure D.1 Relation between the chirp rate and the optimum order

The optimum FrFD for the chirp signal $C(t)$ shown in (D.1) is the domain at which the chirp signal transformation reaches the narrowest band width and appears as a spike. This domain is perpendicular on the chirp instantaneous frequency f_{inst} as shown in Figure D.1. This optimum domain rotation is achieved by time axis rotation with anti clockwise rotation angle θ_{opt} or clockwise $-\vartheta_{opt}$. Thus, from (D.3) the optimum FrFT order a_{opt} can be written as

$$a_{opt} = -(2/\pi)\vartheta_{opt}. \tag{D.4}$$

Geometrical from Figure D.1, it is easy to show that

$$\vartheta_{opt} = \tan^{-1}(1/2\gamma). \tag{D.5}$$

From (D.5) in (D.4)

$$a_{opt} = -(2/\pi)\ \tan^{-1}(1/2\gamma). \tag{D.6}$$

The time-frequency discretization for a chirp sampled signal is shown in Figure D.2. The continuous values for both time and frequency and converted to its discretization form using the sampling frequency F_s with δt is the time resolution and δf is the frequency resolution as follows

$$1 \xrightarrow{\text{no of samples}} 1/\delta t, \tag{D.7}$$

$$\text{and } 2\gamma \xrightarrow{\text{no of samples}} 2\gamma/\delta f$$

Hence, the discretization form of (D.6) using (D.7) can be written as

$$a_{opt} = -\frac{2}{\pi}\tan^{-1}\left(\frac{\delta f/\delta t}{2\gamma}\right). \tag{D.8}$$

This sampled version for the optimum order value, a_{opt} of the general linear chirp signal is used in (3.14).

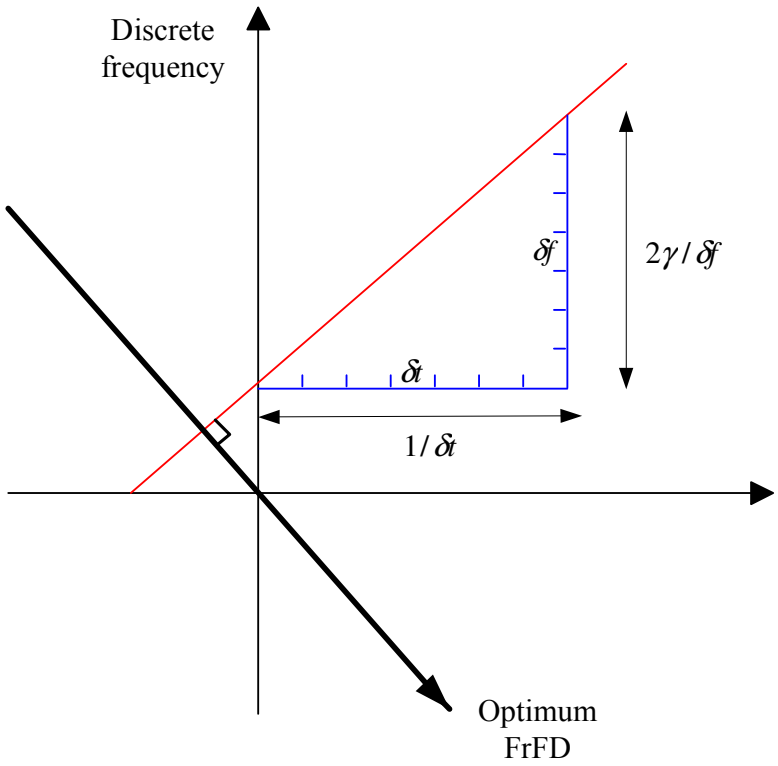

Figure D.2 Discrete relation between the chirp rate and the optimum order

E. The peak position of a chirp signal in the FrFD

The peak position P_p of a chirp signal in the FrFD (compact form) is estimated as shown previously in (3.15) as:

$$P_p = \sin(\vartheta_{opt}) \left[\frac{F_{start}}{\delta f} + \frac{\Delta f \ (L / M_T)}{2 \ \delta f} \right] - \cos(\vartheta_{opt}) \, t_{st} \, . \tag{E.1}$$

To understand this formula, four graphical representations of a chirp signal in time-frequency domain for different time-frequency parameters are demonstrated to give understanding for the previous P_p formula as follows:

(i) Single-sided chirp in time-frequency domain

For normal chirp signal $c_s(t)$ is can be represented as

$$c_s(t) = \exp\left(j2\pi \left(\frac{F_{stop} - F_{start}}{2T} \right) (t)^2 \right), \tag{E.2}$$

where t is the time, T is the chirp time duration (pulse duration), F_{start} is the chirp start frequency, and F_{stop} is the chirp stop frequency. The chirp instantaneous frequency f_{inst} is the derivative of chirp phase as[62, 92]

$$f_{inst}(t) = \frac{F_{stop} - F_{start}}{T} t = \frac{\Delta f}{T} t \, . \tag{E.3}$$

This chirp signal appears at time-frequency domain as the red line shown in Figure E.1. Figure E.1 shows the optimum FrFD for this chirp which is perpendicular on the chirp instantaneous frequency f_{inst}.

The discrete form of the chirp band width Δf is written as $\Delta f / \delta f$ where δf is the frequency resolution. Thus the peak position P_p (the blue thick line) in this case is given by

$$P_p = \sin(\theta_{opt}) \left[\frac{\Delta f}{\delta f} \right]. \tag{E.4}$$

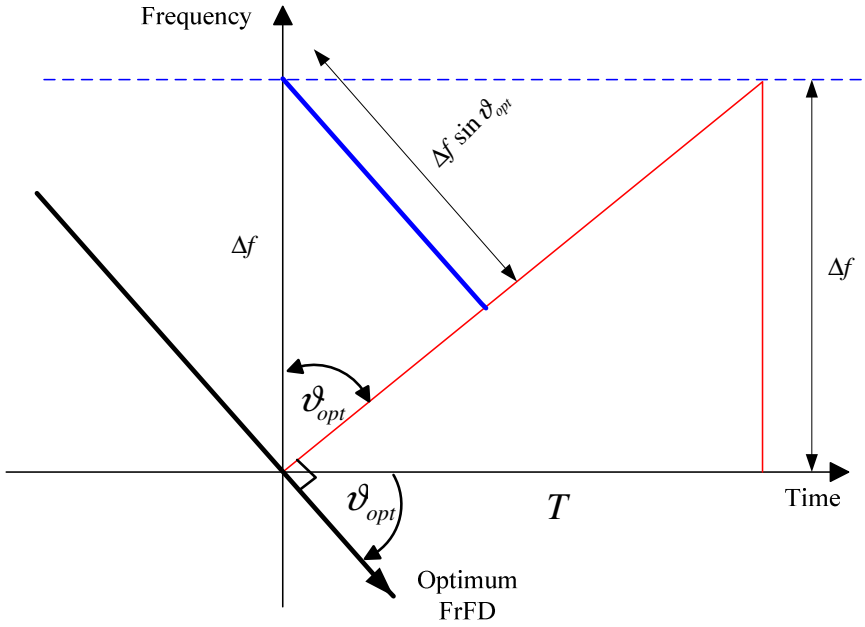

Figure E.1 The relation between the chirp rate and the optimum order

(ii) Double-sided chirp in time-frequency domain

For double sided chirp $c_d(t)$ given by

$$c_d(t) = \exp\left(j2\pi \left(\frac{F_{stop} - F_{start}}{2T} \right) \left(t - \frac{T}{2} \right)^2 \right). \tag{E.5}$$

The chirp instantaneous frequency f_{inst} is the derivative of chirp phase as

$$f_{inst}(t) = \frac{\Delta f}{T} t - \frac{\Delta f}{2}. \tag{E.6}$$

This instantaneous frequency f_{inst} for the double sided chirp is shown in Figure E.2. Hence, the peak position P_p (the blue thick line) in this case is given by

$$P_p = \sin(\vartheta_{opt}) \left[\frac{\Delta f}{2\delta f} \right]. \tag{E.7}$$

The double sided chirp signal will be used during the rest of chirp demonstrations. The P_p formula in (E.7) is a special case of (E.1) when both F_{start} and t_{st} equal zero.

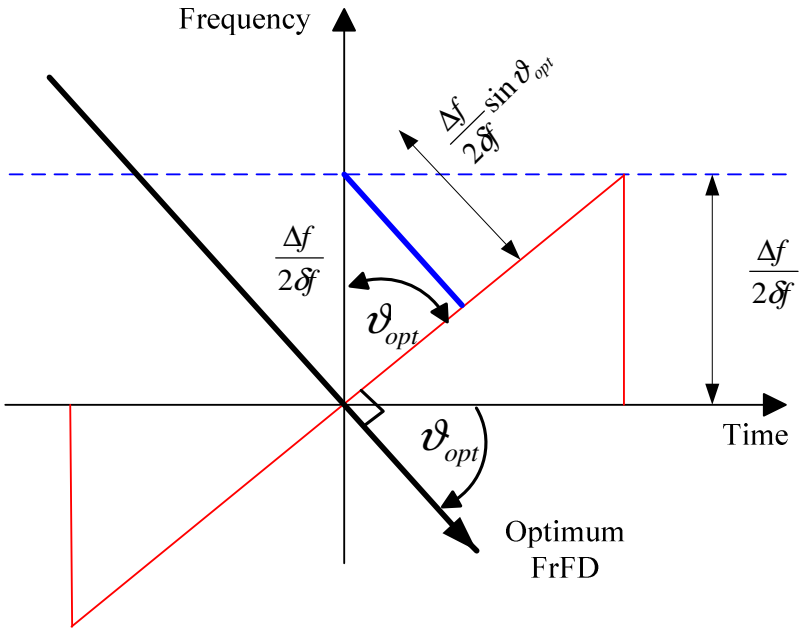

Figure E.2 Double sided chirp and the optimum order

(iii) Double sided chirp in time-frequency domain with shift in frequency

Considering only the upright part of the chirp signal as our field of interest as seen previously for the double sided chirp, if the chirp in this case is shifted in frequency by F_{start}, the number of shifted bins equals to $\frac{F_{start}}{\delta f}$. Figure E.3 shows the peak position P_p (the blue thick line) in this case is given by

$$P_p = \sin(\vartheta_{opt})\left[\frac{F_{start}}{\delta f} + \frac{\Delta f}{2\ \delta f}\right]. \tag{E.8}$$

The P_p formula in (E.8) is a special case of (E.1) when t_{st} equal zero.

(iv) Double sided chirp in time-frequency domain with shift in time

Figure E.4 shows that peak position P_p (the blue thick line) for double sided chirp with shift in time by time samples t_{st} is given by

$$P_p = \sin(\vartheta_{opt})\left[\frac{\Delta f\ (L/M_T)}{2\ \delta f}\right] - \cos(\vartheta_{opt})\,t_{st}\,. \tag{E.9}$$

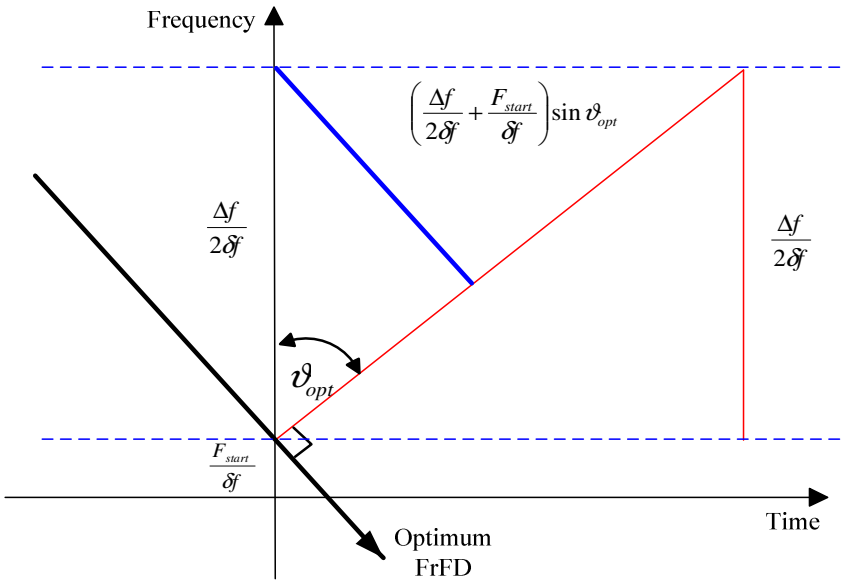

Figure E.3 Double sided chirp with shift in frequency

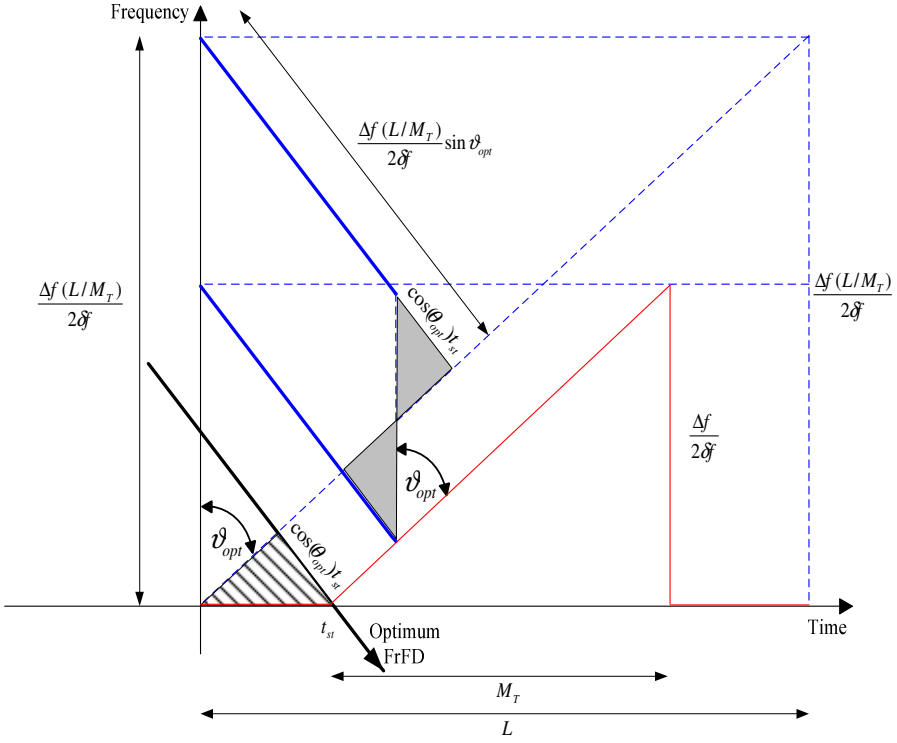

Figure E.4 Double sided chirp with shift in time

Combine the P_p formulas for double sided chirp with shift in time by time samples t_{st} and shifted in frequency by F_{start} show in (E.9) and (E.8), respectively, the general formula for P_p in (E.1).

F. FrFT for Some Special Functions

Using the FrFT definition in (3.6) and (3.7), some of the actual transforms of some elementary functions are shown in Table F.2.

Table F.2 The FrFT of some basic functions

	$x(t)$	$X_\theta(t_a)$
1	$\delta(t-\chi)$	$\sqrt{\frac{1-i\cot\alpha}{2\pi}}e^{\frac{j}{2}(t_a^2\cot\alpha-2t\chi\csc\alpha+\chi^2\cot\alpha)}$, if $a \notin 2\mathbb{Z}$
2	1	$\sqrt{\frac{1+j\tan\alpha}{2\pi}}e^{-j\frac{t_a^2}{2}\tan\alpha}$, if $a \notin 2\mathbb{Z}+1$
3	$e^{\frac{j}{2}(\chi t^2+2\xi t)}$	$\sqrt{\frac{1+i\tan\alpha}{1+\chi\tan\alpha}}e^{j\frac{t_a^2(\chi-\tan\alpha)+2t_a\xi\sec\alpha-\xi^2\tan\alpha}{2(1+\chi\tan\alpha)}}$, if $a-\frac{2}{\pi}\arctan\chi \notin 2\mathbb{Z}+1$
4	$e^{-\frac{j}{2}(\chi t^2+2\xi t)}$	$\sqrt{\frac{1-i\cot\alpha}{\chi-i\cot\alpha}}e^{\frac{j}{2}\cot\alpha\frac{t_a^2(\chi^2-1)+2t_a\chi\xi\sec\alpha+\xi^2}{\chi^2+\cot^2\alpha}}e^{-\frac{1}{2}\csc^2\alpha\frac{t_a^2\chi+2t_a\xi\cos\alpha-\chi\xi^2\sin^2\alpha}{\chi^2+\cot^2\alpha}}$, $\chi>0$
5	$\upsilon_k(t)$	$e^{-jk\alpha}\upsilon_k(t_a)$
6	$e^{-\frac{t^2}{2}}$	$e^{-\frac{t_a^2}{2}}$

where $\chi,\xi \in \Re$, and $\upsilon_k(t)$ are the Hermite-Gauss functions.

G.EMD denoising algorithm for different signals shape and different SNRs

The simulations comprise two simulated signals, the first one is a chirp signal with 1 sec chirp duration chirp bandwidth 500 Hz signals, and the second is block signal with random amplitude and random durations, both signals are sampled at 10 MHz and are shown in Figure G.1-A and Figure G.1-B, respectively.

EMD-DT simulation

Figure G.2-A shows the previous chirp signal with the same chirp parameters with additive white Gaussian noise for SNR= 0 dB is used to show the improvement due to EMD-DT denoising technique. The chirp noisy signal is denoised as seen in Figure G.2-C by performing the thresholding and denoising EMD-DT algorithm and the SNR is improved to 6.7 dB (this value is average of 50 times different simulation of the additive noise). Figure G.2-B shows the IMFs energies $W[i]$ and also threshold level energies. The IMFs energies cross the threshold level at IMF 5.2 (as seen in the zoomed area) so the IMF from 1 up to are 5 considered as noise and all the rest of IMFs is the denoised signal $\tilde{x}(n)$

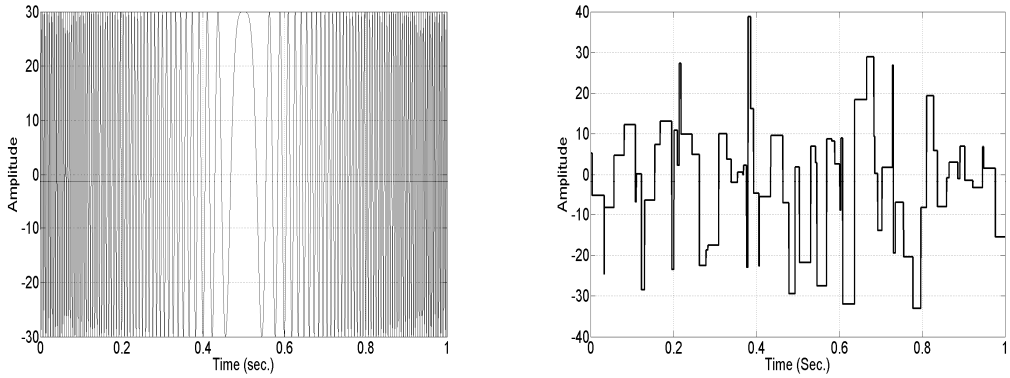

(A) Chirp signal (B) Block signal

Figure G.1 Signal used for EMD-DT validation

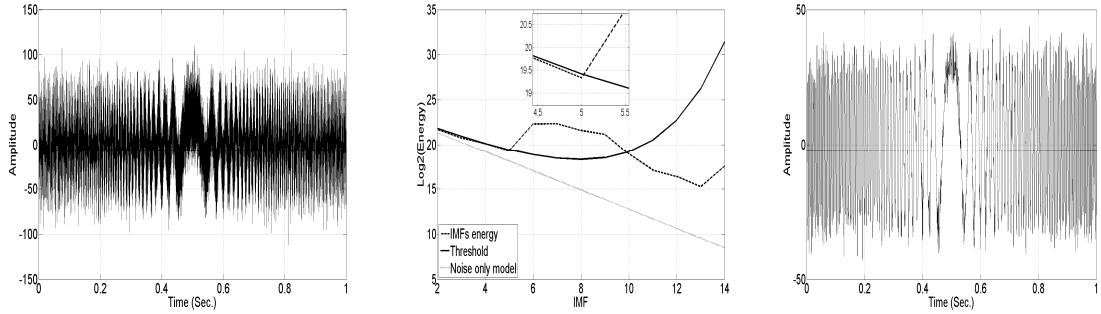

(A) noisy chirp (B) IMF thresholding (C) denoised chirp

Figure G.2 Denoising using EMD-DT algorithm

Using EMD denoising algorithm for Different input SNR

The EMD denoising algorithm works for different input SNR (-5 up to 10 dB) for chirp and block signals. The improvement in output SNR after applying EMD filtering is given in Table G.1. The results comprise an average over 50 independent noise generations.

Table G.1 Signals output SNR for different input SNR (dB)

Input SNR / Signal type	-5	0	10
Chirp signal	8.2	13.2	20.6
Block signal	7.6	12.5	16.7

Author Publications

The following lists the author's publications in reverse chronological order.

Journal Publications

[J5] S. A. Elgamel and J. Soraghan, "Fractional Fourier Transform Filtering to Mitigate High Power Interference in Monopulse Tracking Radars," *Signal Processing Transactions, IEEE.* (submitted)

[J4] S. A. Elgamel, ,and J. Soraghan, "Fractional Fourier Transform Based Matched Filtering for Target Detection in Chirp Radars," *ELSEVIER Signal Processing.* (submitted)

[J3] S. A. Elgamel and J. Soraghan, "Using EMD-FrFT Filtering to Mitigate High Power Interference in Chirp Tracking Radars," *Signal Processing Letter, IEEE.* vol. 18, pp. 263-266, 2011.

[J2] S. A. Elgamel and J. Soraghan, "EMD Based Monopulse Processor for Enhanced radar Tracking in the presence of high power interference," *Radar, Sonar & Navigation, IET.* (In press 2011)

[J1] S. A. Elgamel and J. Soraghan, "Enhanced monopulse tracking radar using optimum fractional Fourier transform," *Radar, Sonar & Navigation, IET,* vol. 5, pp. 74-82, 2010.

Conference Publications

[C9] S. A. Elgamel and J. J. Soraghan, "Mitigate High Power Interference Noise in Chirp Radar Systems Using EMD-FrFT Filtering," in *17th International Conference on Digital Signal Processing, 2011. DSP 2011.*

[C8] S. A. Elgamel, C. Clemente, and J. J. Soraghan, “Radar matched filtering using the Fractional Fourier Transform," in *Sensor Signal Processing for Defence Conference, 2010. SSPD 2010.*

[C7] S. A. Elgamel and J. J. Soraghan, “Fractional Fourier Transform based monopulse radar for combating jamming interference," in *Sensor Signal Processing for Defence Conference, 2010. SSPD 2010.*

[C6] S. A. Elgamel and J. J. Soraghan, “Enhanced monopulse radar tracking using Empirical Mode Decomposition," in *Radar Conference, 2010. EuRAD 2010. European*, 2010.

[C5] S. A. Elgamel and J. J. Soraghan, "Enhanced monopulse radar tracking using fractional Fourier filtering in the Presence of interference," in *Radar Symposium (IRS), 2010 11th International*, pp. 1-4.

[C4] S. A. Elgamel and J. J. Soraghan, "Optimum Fractional Fourier Filtering for monopulse processors distortion," in *Radio Science Conference, 2010. NRSC 2010. National*, 2010, pp. 1-8.

[C3] S. A. Elgamel and J. J. Soraghan, "Enhanced monopulse radar tracking using filtering in fractional Fourier domain," in *Radar Conference, 2010 IEEE*, pp. 247-250.

[C2] S. A. Elgamel and J. Soraghan, "A new Fractional Fourier Transform based monopulse tracking radar processor," in *Acoustics Speech and Signal Processing (ICASSP), 2010 IEEE International Conference on*, pp. 2774-2777.

[C1] S. A. Elgamel and J. Soraghan, "Target tracking enhancement using a Kalman filter in the presence of interference," in *Geoscience and Remote Sensing Symposium,2009 IEEE International, IGARSS 2009*, 2009, pp. III-681-III-684.

References

[1] M. I. Skolnik, *Radar Handbook-Third edition*: McGraw-Hill, Inc., 2008.

[2] R. Klemm and U. Nickel, "Adaptive monopluse with STAP," in *Radar, 2006. CIE '06. International Conference on*, 2006, pp. 1-4.

[3] M. I. Skolnik, *Radar Handbook- Second edition*: McGraw-Hill, Inc., 1990.

[4] D. K. Barton, "History of Monopulse Radar in the US," *Aerospace and Electronic Systems Magazine, IEEE,* vol. 25, pp. c1-c16, 2010.

[5] A. I. Leonov, "History of monopulse radar in the USSR," *Aerospace and Electronic Systems Magazine, IEEE,* vol. 13, pp. 7-13, 1998.

[6] G. M. Kirkpatrick, "Development of A Monopulse Radar System," *Aerospace and Electronic Systems, IEEE Transactions on,* vol. 45, pp. 807-818, 2009.

[7] Z. Xin*, et al.*, "Detection and Localization of Multiple Unresolved Extended Targets via Monopulse Radar Signal Processing," *Aerospace and Electronic Systems, IEEE Transactions on,* vol. 45, pp. 455-472, 2009.

[8] A. D. Seifer, "Monopulse-radar angle tracking in noise or noise jamming," *Aerospace and Electronic Systems, IEEE Transactions on,* vol. 28, pp. 622-638, 1992.

[9] H. Meikle, *Modern Radar Systems* Artech House, Inc., 2008.

[10] Y. Seliktar*, et al.*, "An adaptive monopulse processor for angle estimation in a mainbeam jamming and coherent interference scenario," in *Acoustics, Speech and Signal Processing, 1998. Proceedings of the 1998 IEEE International Conference on*, 1998, pp. 2037-2040 vol.4.

[11] S. A. Elgamel and J. J. Soraghan, "Radar matched filtering using the Fractional Fourier Transform," in *Sensor Signal Processing for Defence Conference, 2010 SSPD*

[12] S. A. Elgamel and J. J. Soraghan, "Optimum Fractional Fourier Filtering for monopulse processors distortion," in Radio Science Conference, 2010 NRSC 2010.

[13] S. A. Elgamel and J. J. Soraghan, "Enhanced monopulse radar tracking using filtering in fractional Fourier domain," in *Radar Conference, 2010 IEEE*, pp. 247-250.

[14] S. A. Elgamel and J. Soraghan, "A new Fractional Fourier Transform based monopulse tracking radar processor," in *Acoustics Speech and Signal Processing (ICASSP), 2010 IEEE International Conference on*, pp. 2774-2777.

[15] S. A. Elgamel and J. J. Soraghan, "Fractional Fourier Transform based monopulse radar for combating jamming interference," in Sensor Signal Processing for Defence Conference, 2010 SSPD

[16] S. A. Elgamel and J. J. Soraghan, "Enhanced monopulse radar tracking using fractional Fourier filtering in the Presence of interference," in *Radar Symposium (IRS), 2010 11th International*, pp. 1-4.
[17] S. A. Elgamel and J. Soraghan, "EMD Based Monopulse Processor for Enhanced radar Tracking in the presence of high power interference," *Radar, Sonar and Navigation, IET*
[18] S. A. Elgamel and J. J. Soraghan, "Enhanced monopulse radar tracking using empirical mode decomposition," in *Radar Conference (EuRAD), 2010 European*, pp. 57-60.
[19] S. A. Elgamel and J. J. Soraghan, "Using EMD-FrFT Filtering to Mitigate Very High Power Interference in Chirp Tracking Radars," *Signal Processing Letters, IEEE,* vol. 18, pp. 263-266.
[20] S. A. Elgamel and J. J. Soraghan, "Mitigate High Power Interference Noise in Chirp Radar Systems Using EMD-FrFT Filtering," in *17th International Conference on Digital Signal Processing, 2011 DSP*.
[21] S. K. a. S. Quegan, *Understanding radar systems* SciTech Publishing, 1999.
[22] D. M. Vavriv*, et al.*, "Development of Surveillance and Tracking Radar," in *Ultrawideband and Ultrashort Impulse Signals, The Third International Conference*, 2006, pp. 26-31.
[23] A. Z. E. Bassem R. Mahafza, *MATLAB simulations for radar systems design*: Boca Raton, FL: CRC Press/Chapman & Hal, 2004.
[24] F. Gini and M. Rangaswamy, *Knowledge Based Radar Detection, Tracking and Classification* John Wiley & Sons, Inc, 2008.
[25] B. R. Mahafza, *Radar system analysis and design using Matlab*: Boca Raton, FL: CRC Press/Chapman & Hall, 2005.
[26] M. I. Skolnik, *Introduction to Radar Systems* vol. Third Edition McGraw-Hill International Editions, 2001.
[27] K. W. Lo, "Theoretical analysis of the sequential lobing technique," *Aerospace and Electronic Systems, IEEE Transactions on,* vol. 35, pp. 282-293, 1999.
[28] A. Guesalaga and S. Tepper, "Synthesis of automatic gain controllers for conical scan tracking radar," *Aerospace and Electronic Systems, IEEE Transactions on,* vol. 36, pp. 302-309, 2000.
[29] R. G. Wiley, *ELINT: The Interception and Analysis of Radar Signals* The Artech House Radar Library, 2006.
[30] A. I. Leonov and K. I. Fomichev, *Monopulse Radar*: Artech House Inc., Norwood, MA, 1986.
[31] D. R. Rhodes, *Introduction to Monopulse*: Artech House Inc., Dedham, MA, 1980.
[32] S. M. Sherman, *Monopulse Principles and Techniques*: Artech House Inc., Norwood, MA, 1984.
[33] "IEEE Standard Radar Definitions," *IEEE Std 686-1997,* p. i, 1998.
[34] D. H. J. a. D. E. Dudgeon, *Array Signal Processing*: Prentice Hall, Englewood Cliffs, NJ, 1993.

[35] G. Liu, *et al.*, "Moving target feature extraction with polarisation diversity in the presence of arbitrary range migration and phase errors," *Radar, Sonar and Navigation, IEE Proceedings -,* vol. 147, pp. 208-216, 2000.
[36] Y. Seliktar, *et al.*, "A space/fast-time adaptive monopulse technique," ed: Hindawi Publishing Corp., 2006, pp. 218-228.
[37] Y. Seliktar, "Space- Time Adaptive Monopulse Processing," PhD, Georgia Institute of Technology, 1998.
[38] D. H. Johnson and D. E. Dudgeon, *Array Signal Processing: Concepts and Techniques*: Prentice-Hall PTR: Englewood Cliffs, NJ, 1993.
[39] P. S. Naidu, *Sensor Array Signal Processing*: CRC Press LLC, 2001.
[40] Y. Seliktar, *et al.*, "Adaptive monopulse processing of monostatic clutter and coherent interference in the presence of mainbeam jamming," in *Signals, Systems & Computers, 1998. Conference Record of the Thirty-Second Asilomar Conference on*, 1998, pp. 1517-1521 vol.2.
[41] I. S. Reed, *et al.*, "Rapid Convergence Rate in Adaptive Arrays," *Aerospace and Electronic Systems, IEEE Transactions on,* vol. AES-10, pp. 853-863, 1974.
[42] R. C. Davis, *et al.*, "Angle Estimation with Adaptive Arrays in External Noise Fields," *Aerospace and Electronic Systems, IEEE Transactions on,* vol. AES-12, pp. 179-186, 1976.
[43] U. Nickel, "Overview of generalized monopulse estimation," *Aerospace and Electronic Systems Magazine, IEEE,* vol. 21, pp. 27-56, 2006.
[44] A. Papoulis, *Probability, Random Variables, and Stochastic Processes*, third edition ed.: McGraw-Hill Inc., NY, NY, 1991.
[45] D. H. Johnson and D. E. Dudgeon, *Array Signal Processing*: Prentice Hall, Englewood Cliffs, NJ, 1993.
[46] S. M. Kogon, *et al.*, "Beamspace techniques for hot clutter cancellation," in *Acoustics, Speech, and Signal Processing, 1996. ICASSP-96. Conference Proceedings., 1996 IEEE International Conference on*, 1996, pp. 1177-1180 vol. 2.
[47] M. K. Stephen, "adaptive Array Processing Techniques for Terrain Scattered Interference Mitigation," PhD, Georgia Institute of Technology, 1996.
[48] Y. Seliktar, *et al.*, "Beam-augmented space-time adaptive processing," in *Acoustics, Speech, and Signal Processing, 1999. ICASSP '99. Proceedings., 1999 IEEE International Conference on*, 1999, pp. 2849-2852 vol.5.
[49] G. W. Titi and D. F. Marshall, "The ARPA/NAVY Mountaintop Program: adaptive signal processing for airborne early warning radar," in *Acoustics, Speech, and Signal Processing, 1996. ICASSP-96. Conference Proceedings., 1996 IEEE International Conference on*, 1996, pp. 1165-1168 vol. 2.
[50] *Mountain Top Radar*. Available: http://spib.rice.edu/spib/mtn_top.html#overview
[51] D. L. Adamy, *EW 102: a second course in electronic warfare*: Horizon House Publications, Inc., 2004.
[52] P. Chevillat, *et al.*, "Rapid Training of a Voiceband Data-Modem Receiver Employing an Equalizer with Fractional-T Spaced Coefficients," *Communications, IEEE Transactions on,* vol. 35, pp. 869-876, 1987.

[53] S. Denno and Y. Saito, "Orthogonal-transformed variable-gain least mean squares (OVLMS) algorithm for fractional tap-spaced adaptive MLSE equalizers," *Communications, IEEE Transactions on,* vol. 47, pp. 1151-1160, 1999.

[54] P. Houlis and V. Sreeram, "An Interconnection between Combined Classical Block Diagrams and Linear Fractional Transformation Block Diagrams," in *Control, Automation, Robotics and Vision, 2006. ICARCV '06. 9th International Conference on*, 2006, pp. 1-5.

[55] S. Venkatesh, "Identification of uncertain systems described by linear fractional transformations," in *Decision and Control, 2003. Proceedings. 42nd IEEE Conference on*, 2003, pp. 5532-5537 Vol.5.

[56] R. Saxena and K. Singh, "Fractional Fourier transform: A novel tool for signal processing," *Journal of Indian Institute of Science,* vol. 58, pp. 11-26 February 2005 2005.

[57] V. NAMIAS, "The Fractional Order Fourier Transform and its Application to Quantum Mechanics," *IMA Journal of Applied Mathematics,* vol. 25, pp. 241-265, March 1, 1980 1980.

[58] L. B. Almeida, "The fractional Fourier transform and time-frequency representations," *Signal Processing, IEEE Transactions on,* vol. 42, pp. 3084-3091, 1994.

[59] H. M. Ozaktas and D. Mendlovic, "Fourier transforms of fractional order and their optical interpretation," *Optics Communications,* vol. 101, pp. 163-169, 1993.

[60] D. Mendlovic and H. M. Ozaktas, "Fractional Fourier transforms and their optical implementation: I," *J. Opt. Soc. Am. A,* vol. 10, pp. 1875-1881, 1993.

[61] D. Mendlovic, *et al.*, "Signal spatial-filtering using the localized fractional Fourier transform," *Optics Communications,* vol. 126, pp. 14-18, 1996.

[62] H. M. Ozaktas, *et al.*, *The Fractional Fourier Transform: with Applications in Optics and Signal Processing*: John wiley & Sons Ltd, January 2001.

[63] A. Bultheel and H. Martìnez Sulbaran, "A shattered survey of the fractional Fourier transform, http://www.cs.kuleuven.be/_nalag/papers/ade/frft/index.html," 2003.

[64] A. Bultheel and H. E. Sulbaran, "Computation of the Fractional Fourier Transform," *Applied and Computational Harmonic Analysis,* vol. 16, pp. 182-202, February 2004.

[65] D. S. Yeung, *et al.*, "Complete way to fractionalize Fourier transform," *Optics Communications,* vol. 230, pp. 55-57, 2004.

[66] E. Leith, "Review of 'Systems and Transforms With Applications to Optics' " *Information Theory, IEEE Transactions on,* vol. 18, pp. 451-452, 1972.

[67] T. Ran, *et al.*, "Image Encryption With Multiorders of Fractional Fourier Transforms," *Information Forensics and Security, IEEE Transactions on,* vol. 5, pp. 734-738, 2010.

[68] Z. Nanrun and D. Taiji, "Optical Image Encryption Scheme Based on Multiple-parameter Random Fractional Fourier Transform," in *Electronic Commerce and Security, 2009. ISECS '09. Second International Symposium on*, 2009, pp. 48-51.

[69] C. Clemente and J. J. Soraghan, "Range Doppler SAR processing using the Fractional Fourier Transform," in *Radar Symposium (IRS), 2010 11th International*, 2010, pp. 1-4.
[70] C. Clemente and J. J. Soraghan, "Fractional Range Doppler Algorithm for SAR imaging," in *Radar Conference (EuRAD), 2010 European*, 2010, pp. 248-251.
[71] A. S. Amein and J. J. Soraghan, "High Resolution- High Focused Squint-Mode Radar Imaging Using the Fractional Chirp Scaling Algorithm," in *Acoustics, Speech and Signal Processing, 2006. ICASSP 2006 Proceedings. 2006 IEEE International Conference on*, 2006, pp. III-III.
[72] A. S. Amein and J. J. Soraghan, "Fractional Chirp Scaling Algorithm: Mathematical Model," *Signal Processing, IEEE Transactions on,* vol. 55, pp. 4162-4172, 2007.
[73] S. Shankar and N. Srivastav, "Power Play: On the Notion of Fractional Quantum Fourier Transform," *Potentials, IEEE,* vol. 30, pp. 29-32, 2011.
[74] B. Santhanam and M. Hayat, "On a pseudo-subspace framework for discrete Fractional Fourier transform based chirp parameter estimation," in *Digital Signal Processing Workshop and IEEE Signal Processing Education Workshop (DSP/SPE), 2011 IEEE*, 2011, pp. 360-363.
[75] R. Shi*, et al.*, "A Novel SAR Signal Reconstruction Method from Non-uniform Sampling Associated with Fractional Fourier Transform," in *Measuring Technology and Mechatronics Automation (ICMTMA), 2011 Third International Conference on*, 2011, pp. 210-213.
[76] G. Jianjun and S. Fulin, "A new cross-range scaling algorithm based on FrFT," in *Signal Processing (ICSP), 2010 IEEE 10th International Conference on*, 2010, pp. 2043-2046.
[77] C. Xiaolong and G. Jian, "A fast FRFT based detection algorithm of multiple moving targets in sea clutter," in *Radar Conference, 2010 IEEE*, 2010, pp. 402-406.
[78] N. E. Huang*, et al.*, "The empirical mode decomposition and the Hilbert spectrum for nonlinear and non-stationary time series analysis," *Proc. R. Soc. London,* vol. Ser. A, 454, pp. 903-995, 1998.
[79] *NASA Inventions and Contributions Board* Available: http://www.nasa.gov/offices/oce/icb/winners/ioy/2002_ioy.html
[80] N. E. Huang*, et al.*, "A confidence limit for the empirical mode decomposition and Hilbert spectral analysis," *Procedures of the Royal Society of London,* vol. 459, pp. 2317–2345, 2003.
[81] B. Narsimha*, et al.*, "Denoising and QRS detection of ECG signals using Empirical Mode Decomposition," in *Communications and Signal Processing (ICCSP), 2011 International Conference on*, 2011, pp. 439-442.
[82] H. Ji*, et al.*, "Flow Pattern Identification Based on EMD and LS-SVM for Gas-Two-Phase Flow in a Minichannel," *Instrumentation and Measurement, IEEE Transactions on,* vol. 60, pp. 1917-1924, 2011.
[83] N. ur Rehman and D. P. Mandic, "Filter Bank Property of Multivariate Empirical Mode Decomposition," *Signal Processing, IEEE Transactions on,* vol. 59, pp. 2421-2426, 2011.

[84] A. Roy and J. F. Doherty, "Overlay Communications Using Empirical Mode Decomposition," *Systems Journal, IEEE,* vol. 5, pp. 121-128, 2011.
[85] M. A. Kutay*, et al.*, "Optimal filtering in fractional Fourier domains," *Signal Processing, IEEE Transactions on,* vol. 45, pp. 1129-1143, 1997.
[86] M. A. Kutay*, et al.*, "Optimal filtering in fractional Fourier domains," in *Acoustics, Speech, and Signal Processing, 1995. ICASSP-95., 1995 International Conference on*, 1995, pp. 937-940 vol.2.
[87] C. Candan*, et al.*, "The discrete fractional Fourier transform," *Signal Processing, IEEE Transactions on,* vol. 48, pp. 1329-1337, 2000.
[88] H. M. Ozaktas*, et al.*, "Digital computation of the fractional Fourier transform," *Signal Processing, IEEE Transactions on,* vol. 44, pp. 2141-2150, 1996.
[89] B. Santhanam and J. H. McClellan, "The DRFT-a rotation in time-frequency space," in *Acoustics, Speech, and Signal Processing, 1995. ICASSP-95., 1995 International Conference on*, 1995, pp. 921-924 vol.2.
[90] J. McClellan and T. Parks, "Eigenvalue and eigenvector decomposition of the discrete Fourier transform," *Audio and Electroacoustics, IEEE Transactions on,* vol. 20, pp. 66-74, 1972.
[91] J. McClellan, "Comments on "Eigenvector and eigenvalue decomposition of the discrete Fourier transform"," *Audio and Electroacoustics, IEEE Transactions on,* vol. 21, pp. 65-65, 1973.
[92] C. Capus and K. Brown, "Short-Time fractional fourier methods for the time-frequency representation of chirp signals," *The Journal of the Acoustical Society of America,* vol. 113(6), pp. 3253-63, 2003.
[93] R. Jacob*, et al.*, "Applications of Fractional Fourier Transform in Sonar Signal Processing," *Journal of Research, IETE* vol. 55, pp. 16-27, 2009.
[94] P. Soo-Chang*, et al.*, "Discrete fractional Fourier transform based on orthogonal projections," *Signal Processing, IEEE Transactions on,* vol. 47, pp. 1335-1348, 1999.
[95] P. Flandrin*, et al.* Empirical Mode Decomposition [Online]. Available: http://perso.ens-lyon.fr/patrick.flandrin/emd.html
[96] P. Flandrin*, et al.*, "Detrending and denoising with Empirical Mode Decompositions," in The 2004 European Signal Processing Conference (EUSIPCO-2004), 2004
[97] Y. Kopsinis and S. McLaughlin, "Empirical mode decomposition based soft-thresholding," in Proc. 16th Eur. Signal Processing Conference (EUSIPCO), Lausanne, Switzerland, 2008.
[98] Y. Kopsinis and S. McLaughlin, "Development of EMD-Based Denoising Methods Inspired by Wavelet Thresholding," *Signal Processing, IEEE Transactions on,* vol. 57, pp. 1351-1362, 2009.
[99] G. Rilling and P. Flandrin, "One or Two Frequencies? The Empirical Mode Decomposition Answers," *Signal Processing, IEEE Transactions on,* vol. 56, pp. 85-95, 2008.
[100] Y. Kopsinis and S. McLaughlin, "Investigation and Performance Enhancement of the Empirical Mode Decomposition Method Based on a Heuristic Search

Optimization Approach," *Signal Processing, IEEE Transactions on,* vol. 56, pp. 1-13, 2008.
[101] T. Tanaka and D. P. Mandic, "Complex Empirical Mode Decomposition," *Signal Processing Letters, IEEE,* vol. 14, pp. 101-104, 2007.
[102] G. Rilling*, et al.*, "Bivariate Empirical Mode Decomposition," *Signal Processing Letters, IEEE,* vol. 14, pp. 936-939, 2007.
[103] P. Flandrin*, et al.*, "EMD Equivalent Filter Banks, from Interpretation to Applications," in *Hilbert-Huang Transform and Its Applications* ed: World Scientific, 2005, pp. pp. 57 -74.
[104] E. Leith, "Review of 'Systems and Transforms With Applications to Optics' (Papoulis, A.; 1968)," *Information Theory, IEEE Transactions on,* vol. 18, pp. 451-452, 1972.
[105] A. Koc*, et al.*, "Digital Computation of Linear Canonical Transforms," *Signal Processing, IEEE Transactions on,* vol. 56, pp. 2383-2394, 2008.
[106] A. Farina*, et al.*, "Maximum likelihood estimator approach to determine the target angular co-ordinates in presence of main beam interference: application to live data acquired with a microwave phased array radar," in *Radar Conference, 2005 IEEE International*, 2005, pp. 61-66.
[107] J. Zongsheng and S. Xicai, "Analysis on the tracking performance of active radar seeker under the condition of coherent interference," in *Intelligent Computing and Intelligent Systems, 2009. ICIS 2009. IEEE International Conference on*, 2009, pp. 418-422.